2014

Surface chemistry and growth of oxide supported metal nanoparticles

Ziyu Zhang
Louisiana State University and Agricultural and Mechanical College, zzhang3@lsu.edu

SURFACE CHEMISTRY AND GROWTH OF OXIDE SUPPORTED METAL NANOPARTICLES

A Dissertation

Submitted to the Graduate Faculty of the
Louisiana State University and
Agriculture and Mechanical College
in partial fulfillment of the
requirements for the degree of
Doctor of Philosophy

in

The Department of Physics and Astronomy

by
Ziyu Zhang
B.S., University of Science and Technology of China, 2004
May 2014

To my whole family

Acknowledgements

First of all, I would like to thank my advisor Dr. Richard L. Kurtz and Philip T. Sprunger and it had been an honor to be their Ph.D. student. I am very grateful to them for their guidance, encouragement and inspiration throughout my whole PhD study. They are always positive, patient, and enthusiastic about my research work. Thanks to the helpful discussions with them, I have learned a lot in every research aspect, especially how to present my work, and how to troubleshoot and fix problems. They have made a great example how to be a successful physicist and professor. I also want to express my thanks to Dr. John C. Flake, Dr. E. Ward Plummer and Dr. Milen Yakimov for their valuable time to serve on my committee and suggestions to future work.

I would like to acknowledge Minh Le, Maoming Ren and Fei Wang for the inspiring discussions and sharing their knowledge of science with me. It is my pleasure to work with them on various experiments from physics to chemical engineering for a couple of years. I am also thankful to Frank Womack for his endless help on showing me how to use all kinds of tools and instruments, and how to fix the chamber stuffs, and especially his kind helps in TAMU. I am also thankful to Matthew Patterson for his help in STM experiments. I am also thankful to Fangyang Liu for the ISS measurements, and he made significant contributions to the experiments, and shared some of his experimental experience with me. I am also thankful to Chen Chen for his help in software and making programs. I would also like to acknowledge CAMD facility in LSU, where I have made all the spectra measurements.

My life at LSU was made wonderful and enjoyable largely due to the many friends that became a part of my life. I am grateful for time spent with my roommates and friends

for our memorable trips and for many other people and memories. Thanks to all of them for being in my life or having been in it.

At the end, I would like to thank my beloved family, my parents, my uncle and aunt, my cousins for their love, support and encouragement. My parents raised me with their love and supported me in all my pursuits. I am very thankful to my aunt, who is always willing to listen to me and offer me many helpful suggestions. I feel very lucky to have them in my life and share my enthusiasm for academic pursuits with them.

---Ziyu Zhang

Table of Contents

Abstract

A model heterogeneous catalyst inspired by a real catalyst is synthesized for the purpose of understanding how it works. To make such model catalysts, we choose to evaporate metal atoms on metal oxide single crystals and measure them under UHV conditions. The study of model catalysts could advance the understandings of fundamental catalytic properties of real catalysts and helps to optimize or redesign industrial catalysts. In our experiments, many ultra-high vacuum (UHV) techniques have been employed to investigate the atomic and electronic structure of the surface as well as the interface of the prepared samples. In particular, the surface-sensitive tools such as electron energy loss spectra (EELS) and low energy ion scattering (LEIS) spectra provide us detailed information of the surface modification. In this dissertation, we confine our attention to three popular catalysts: Cu on ZnO, Au on ZnO and Cu on TiO_2, which play primary roles on modern methanol industry. For instance, Au on ZnO and Cu on ZnO are important catalysts for methanol synthesis, water-shift reaction and methanol-steam reforming, while Cu on TiO_2 possesses a high photocatalytic activity for photoreduction of CO_2 into methanol. It becomes important for us to develop an understanding of which factors determine the functions of the prepared samples. Different metal growth models are observed for the above samples, due to the varied metal-oxide interactions. At the high substrate temperature, full encapsulation of metal nanoparticles takes place to all of the above samples, which dramatically changes the adsorption behavior and catalytic performance. It provides a strong indication that these thin encapsulation layers are very different from their bulk materials in both geometric and electronic sides. The charge transfer in the interface may be responsible for the modification of geometric and

electronic structure of surface, and results in high-thermal stability of these ultra-thin films. The above reconstruction leads to an exceptional catalytic activity of CO oxidation through a different reaction kinetics and mechanism. The CO oxidation experiments show a direct relation between encapsulation rate and reaction rate, which indicates the active sites should be localized at these thin oxide films rather than the metal nanoparticles.

Chapter 1: General Introduction

1.1 Overview

In modern industry, chemical manufacturing is known to be based or relies heavily on catalytic processes, and catalysis industry contributes to approximately 1/3 of gross domestic product (GDP) in the world. In the late 20th century, heterogeneous catalysis of industrial importance had developed into broad research area from nano-crystalline powders to surface science studies supported by single crystals, in order to improve the catalytic performance of industrial catalysts. [1] As the development of catalysis industry, the new demand of catalyst design becomes urgent to promote a desired conversion but also to avoid any undesirable side reactions. In the last decade, numerous research groups have developed nanosize industrial catalysts which contribute to their functions, for instance catalytic activity and selectivity for certain reactions. [2] Among these industrial catalysts, typical heterogeneous catalysts are composed of dispersed metal nanoparticles supported by highly porous, high-surface-area oxides. The oxide-metal interface of a heterogeneous catalyst is proposed to play a significant role on multipath reactions by modifying its atomic and electronic structure. [3] A great step into understanding the nature of heterogeneous catalysis is the development of surface science. The advents of high resolution in-situ spectroscopies, atomically resolved surface science techniques and precise calculation methods enable scientists to probe the geometric and electronic properties of surfaces and adsorbates. The above efforts and achievements help scientists to learn how the catalytic reactions proceed at atomic level and what the decisive factors are to determine catalytic reactivity and stability, which is fundamental to the mechanism of certain catalytic reactions.

As mentioned above, most of industrial catalysts are based on metal nanoparticles. However, support effects, and quantum size effects could not be investigated on metal single crystals. Therefore a model heterogeneous catalyst is synthesized for the purpose of overcoming the above barriers, in order to approach ideal molecular catalyst with identical active sites. To achieve this goal, a typical model catalyst comprising dispersed metal clusters supported on oxide single crystal is designed with a known structure, containing identifiable and countable active sites. The simple surface structure of model catalyst offers a pathway for scientists to investigate the above size effect, and even the complex metal-oxide interaction. For instance, strong metal support interaction is found to be associated with encapsulation behavior by the support. Although it is a great advantage to use model catalysts to understand real catalysts, material gap is another barrier that may be encountered with the application of model catalyst. [4, 5] For instance, industrial catalysts always have very large surface area, due to their highly porous structure.

Besides the identical structure, most of the model surface studies focus on the simple chemical reactions, such as carbon monoxide oxidation into carbon dioxide. Such simple type of reaction is a basic approach to understand the nature of active sites, which plays a decisive role in understanding multi-path reactions in industrial reactions.

Reactivity is another essential factor in developing certain reactions that contain the desired product with high reaction rate. Figure 1.1 illustrates how the formation of two products competes with each other in the corresponding potential-energy plot. [7] The small energy difference ($\Delta G1$-$\Delta G2$) completely changes the product distribution, and it has several possible causes such as the coadsorbates, structural changes, or even various

charge transfer. Besides the above factors, the types of reactions including both the reactants and the desired products are also primary factors determining the overall reaction rates.

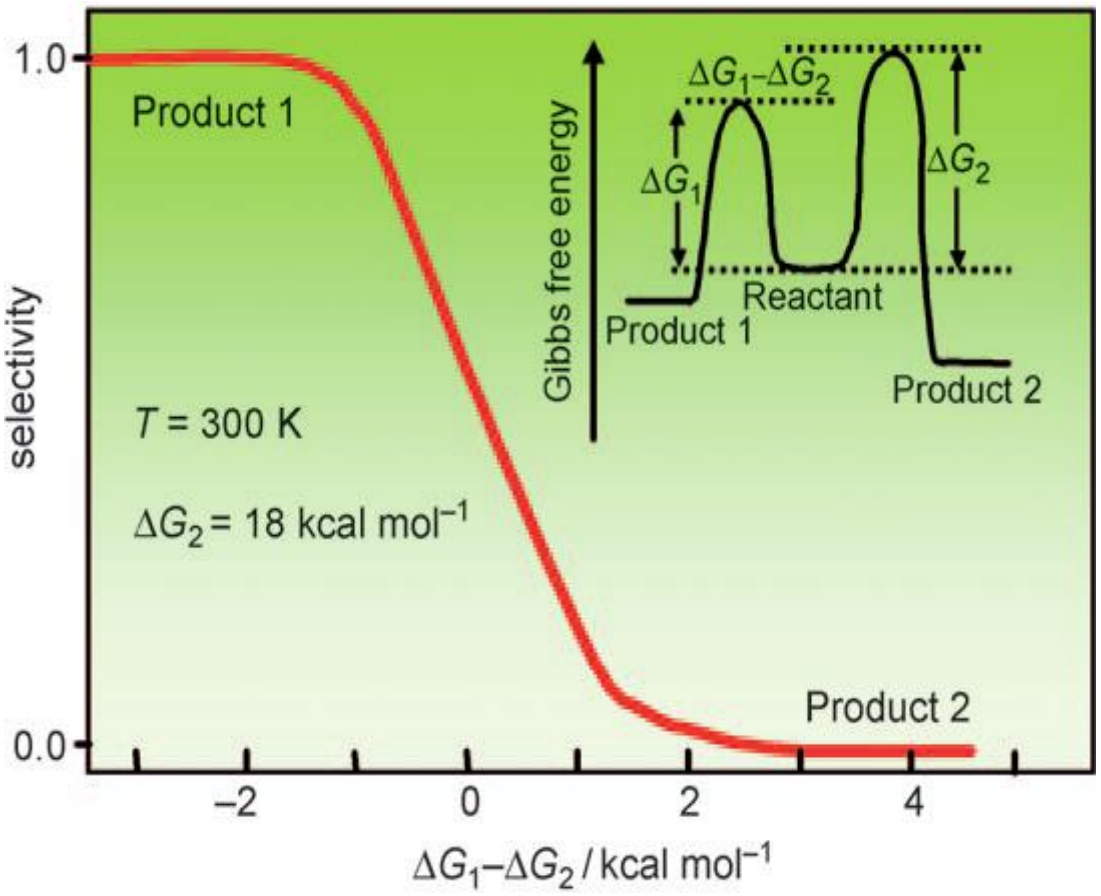

Figure 1.1 Potential-energy plot illustrating selectivity in heterogeneous catalysis. The relative heights of the activation barriers for different reactions determine the selectivity of catalytic processes. [6] "Reprinted (adapted) with permission from J. Phys. Chem. B 106 (2002) 4043. Copyright (2002) American Chemical Society."

1.2 Heterogeneous Catalysts

1.2.1 Metal Nanoparticles On Oxide Surface

As mentioned above, the size and shape of heterogeneous catalysts could be of decisive importance to decide their performance, which is influenced by interactions with the oxide support. [8, 9] And a lot of other important factors are also summarized in Figure

1.2. Among these factors, the metal-support interaction is the primary one that influences the particle geometry and the particular electron-transfer processes are exploited to alter the growth model of metals. The previous studies have revealed the 1D growth of Au chains on alumina, while 2D growth of Au islands are observed on MgO and CaO films. [10, 11, 12]

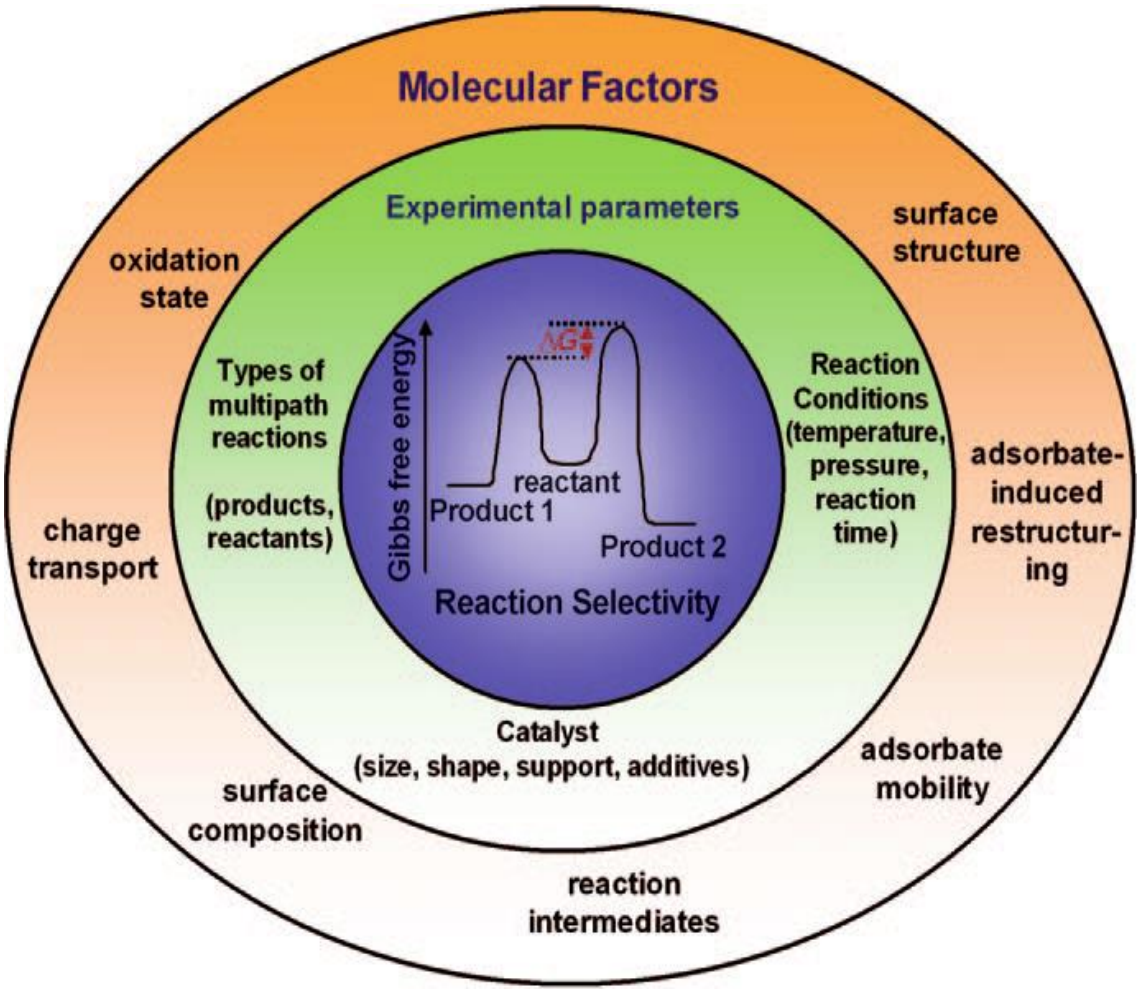

Figure 1.2 Seven molecular factors influencing the reactivity of a catalytic reaction (temperature, pressure, reaction time, and nature of the support) could influence the pathways. As shown in Figure 1.2, Gabor A. Somorjai has identified seven molecular level factors that affect reactivity: (1) surface structure, (2) adsorbate-induced restructuring, (3) adsorbate mobility, (4) reaction intermediates, (5) surface composition, (6) charge transfer during catalysis, (7) oxidation state of the catalyst. [7]

In an actual chemical reaction, the catalyst's performance is known to highly depend on how the adsorbed species are bond to the surface and how stable is the intermediate products. With the development of nanocatalytic reactions, an important question needs to be answered: why does the size of the oxide supported metal nanoparticle play a significant role in changing the bond strength between the adsorbed molecule and metal particle? In order to address this question, it is important to measure gas molecule adsorption on model heterogeneous catalysts.

A pronounced trend is shown in Figure 1.3: the initial heat of CO adsorption is decreased with a smaller particle size. [13, 14] Two possible microscopic effects may be responsible for the above phenomenon: (1) weakening of the chemical adsorption interaction; (2) reduction of the Van der Waals attraction. The first one stands to the reason that smaller clusters contain higher number density of lower coordination sites in higher surface-volume ratio. And the cause for the second one is that the bulk electrons of the metal nanoparticles fluctuates the charge density in the adsorbed molecule. [14, 15]

Another essential effect "strong metal support interaction (SMSI)" was first introduced in 1978 to describe unusual decreased chemisorption capacity for CO and H_2 on reducible oxides supported metal particles after heat treatment, especially on TiO_2 supported Pt. [16, 17] Much effort has been directed at understanding these phenomena, and one possible explanation is the encapsulation of supported metal particles by the oxide support. It was expected that the suppression of gas molecule adsorption on metal surface would inhibit the desired reactions, however, the catalytic reactions had shown the decoration of metal particles' surface by thin oxide films leads to enhanced catalytic

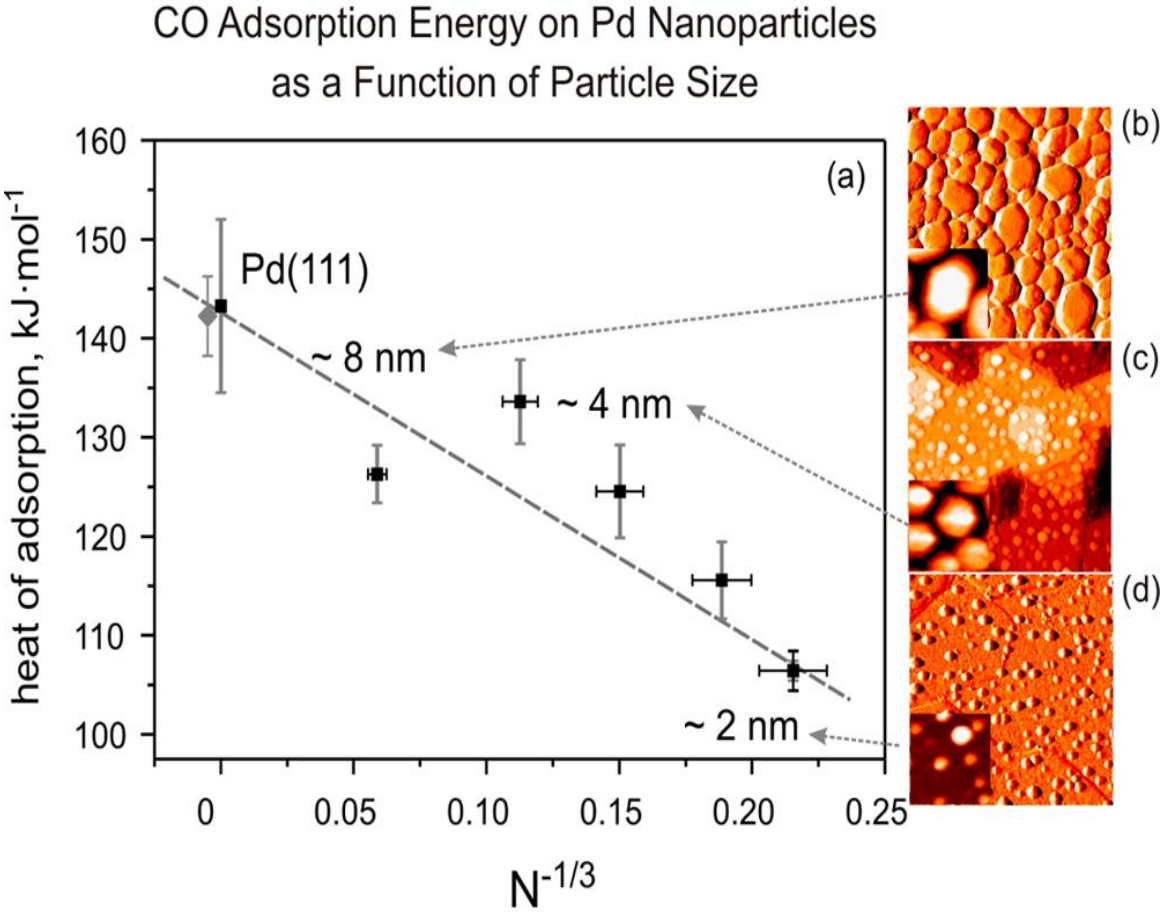

Figure 1.3 (a) initial heat of adsorption of CO as a function of Pd particles. The gray symbol corresponds to the literature value on Pd (111). (b-d) STM image of the $Pd/Fe_3O_4/Pt(111)$ model catalyst for nominal Pd coverage of (b) 0.03 nm, (c) 0.4nm, (d) 0.7nm.[13] Copyright (2010) by The American Physical Society, [14] "Reprinted (adapted) with permission from Acc. Chem. Res. 2012. Copyright (2012) American Chemical Society."

activity. [18] Unfortunately, the atomic structure and function of these important encapsulation layers become always unknown and debate. [19, 20] what are the active sites? Are they still those directly covered by the encapsulation layer? Or new active sites on the encapsulation layer? In attempt to answer this question, H. J. Freaund's group has examined the model system Pt nanoparticles supported on Fe_3O_4 (111) and thin iron oxide films on Pt (111).

Therefore, the most debated questions about Figure 1.4a shows Pt nanoparticles deposited at 300K and 850K, and top facets of these Pt nanoparticles are exposed in the (111) orientation. [21] The inset of Figure 1.4a shows FeO (111) film on top of Pt (111), consisting of close-packed layers of iron and oxygen atoms. [22] The FeO encapsulation is induced by the high adhesion energy between Pt and iron oxide, in order to minimize the surface energy. The further CO oxidation experiments have yielded the similar results that a higher reactivity is found for the encapsulated Pt particles exhibit rather than clean Pt particles. On the other side, FeO (111) films on Pt (111) show considerable reactivity of CO oxidation at relatively low temperatures and realistic pressures, whereas FeO (111) single crystal is essentially inert in UHV based experiments. This interesting example demonstrates that the loaded metal particles may result in modifying the atomic and electronic structure of the above ultra-thin oxide films, and therefore results in promoted reactivity of CO oxidation. In other words, the nano-structured oxide may show different physical and chemical properties from the bulk oxide.

1.2.2 Ultra-thin Oxide Films On Metal Single Crystal

To obtain adequate conductivity, the growth of oxide thin films supported on a conducting metal single crystal is another important way to make model oxide surfaces. These unique oxide thin films with adequate conductivity enable us to use the PES, AES, EELS and LEIS to investigate their surface structure and electronic structure. [24] According to previous studies, the various combinations of metal and oxide and suitable supported oxide film thickness could bring dramatic changes to the characteristics of ultra-thin oxide films, since the intrinsic properties of the bulk oxide material could be tuned by the interfacial interaction between metal and oxide. Here it is important to note

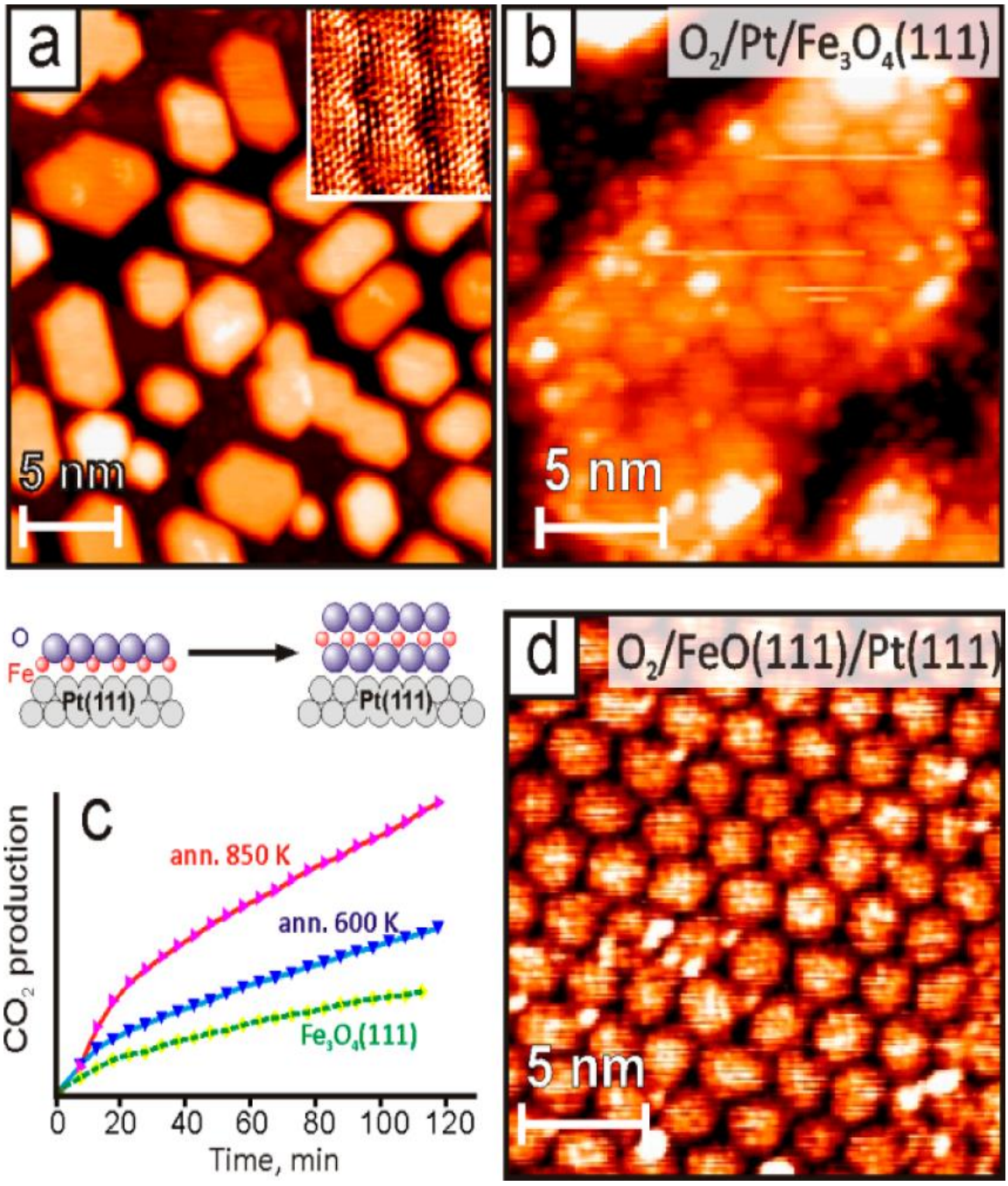

Figure 1.4 (a) STM image of Pt deposited onto a Fe_3O_4 (111) film and subsequently annealed in UHV at 850K. (b) STM image of the encapsulated Pt particle exhibiting the same surface reconstruction as a FeO(111)/Pt(111) film (d). (c) CO_2 production over a clean Fe_3O_4 (111) film and two $Pt/Fe_3O_4(111)$ model catalysts, annealed in UHV to 600 and 850 K prior to the reaction, respectively. [21, 22, 23, 14] Copyright (1998) by The American Physical Society

that the chemical composition and even the defect concentration of oxide films could be modified under different experimental conditions, for instance the more reducing condition brings more O vacancies to the oxide film. That is why a new series of oxide based catalysts with tunable properties becomes possible to be fabricated by the preparation of metal supported thin oxide films. [24, 25]

The adhesion between the surface of metal single crystal and the oxide overlayers is pivotal to geometric properties of the oxide thin films and results in a higher thermal stability. [26] If the metal support is very active, the contribution from the interface might be more than that from the intrinsic characteristics of the oxide, and therefore the structure of these thin films becomes entirely controlled by the of the crystallographic structure of the metal support, especially its symmetry and lattice parameters. [27, 28, 29] For example, the direction of oxide layer growth is found to be partially dependent on the symmetry of its substrate, since oxide phases can be stabilized in a thermodynamically unfavorable structure. Moreover, metals with high oxidation enthalpies have a higher tendency to react with oxygen ions in the oxide thin films to form interfacial bonds, which is ascribed to oxygen spillover effect.

The oxide thin films have different adsorption behavior from the corresponding bulk oxide materials when the film thickness is less than 1nm and the metal support starts to dominate the binding energy of adsorbates to the oxide surface. Figure 1.5 presents various effects of metal support on the adsorption behavior of the oxide thin films, on which the binding strength of adsorbates could be enhanced with respect to the bulk materials. [29] Metals are known to have free electrons and a strong dielectric response to the oxide films, which brings a larger dispersive of adsorbates on thin oxide films and

enhances the binding strength. [30] Therefore, electrons could transfer from the metal support into electronegative adsorbates or from electropositive adsorbates into the metal support. In the ionic oxide materials, the adsorbate binds either to surface anions or

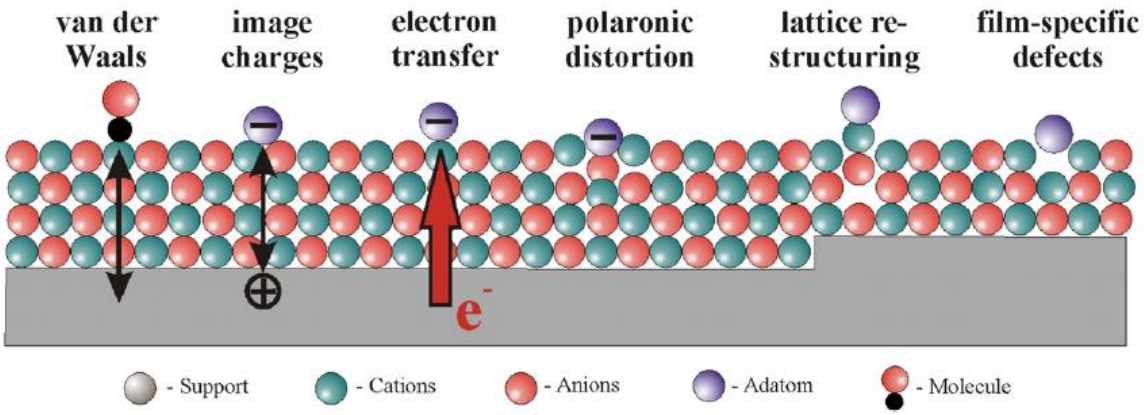

Figure 1.5 Examples for binding mechanism which are specific to thin-film systems. [29]

cations through coulomb interactions with the Madelung potential of the oxide, determined by its charge state. Thus the neighboring ions of oxide to the adsorption sites needs to be displaced to adapt to the extra charge, because of the polaronic distortion induced in the underlying lattice. [31] This phenomenon plays a significant role on adsorption processes and in stabilizing the excitons of the oxide materials. Besides the polaronic distortion, the formation of an image charge in the metal support below could increase the interaction strength compared to the neutral charged species. [32, 33] For instance, the binding energy between neutral Au adatoms and bulk MgO is 0.9 eV, while the negatively charged Au adatom has 2.3 eV binding energy with 3 ML thick MgO film supported on Mo (001) single crystal. [34]

Besides the electron exchange, thin oxide films are more flexible, which enables the thin films to form new chemical bonds with the adsorbed molecules through rearranging the configuration of their internal atoms and chemical bonds. That is why a much higher

energy barrier is required for bulk oxides to break and rearrange the formed surface chemical bonds, where the barrier could be lowered for thin oxide films, due to the above various effects from the metal support.

In addition, the above bond arrangement could release new valences and result in the stabilization of the adsorbed molecules even on the oxide surface, which is originally inert to the adsorbates. In the case of Au on alumina/NiAl (110) thin films, the deposited Au atoms induce the cleavage of Al-O bonds in the thin film, resulting in new chemical bonds between the unsaturated Al ions and the adatoms. [10] As a consequence of bond reorganization, the adsorption energy of Au adatom to alumina films is greatly enhanced to 2.1 eV, compared to 0.8 eV to the bulk alumina. [36]

The charge transfer from the metal support is also found to alter the geometric and chemical properties of the Au clusters on the oxide thin films. [37, 38] Figure 1.6 shows how the growth model of Au atoms is influenced by the thickness of oxide thin films. On 2 ML MgO/Ag (001) films, the Au growth is found to be in 2D, and single-layer islands are formed after deposition of Au. Furthermore, a nearly complete wetting layer is developed with more Au deposition. On 8 ML MgO/Al (001) films, 3D growth regime is observed, suggesting the absence of charge transfer in the interface. This spatial arrangement also implies the reduction of charge transfer on the higher thickness, which results in the above 3D growth of Au. Compared to 3D growth on the higher thickness, the 2D growth could largely increase the contact area between Au and the supporting MgO film, due to the electron transfer into Au affinity levels. The above cases establish a direct relationship between the oxide film thickness and its adsorption activity, which

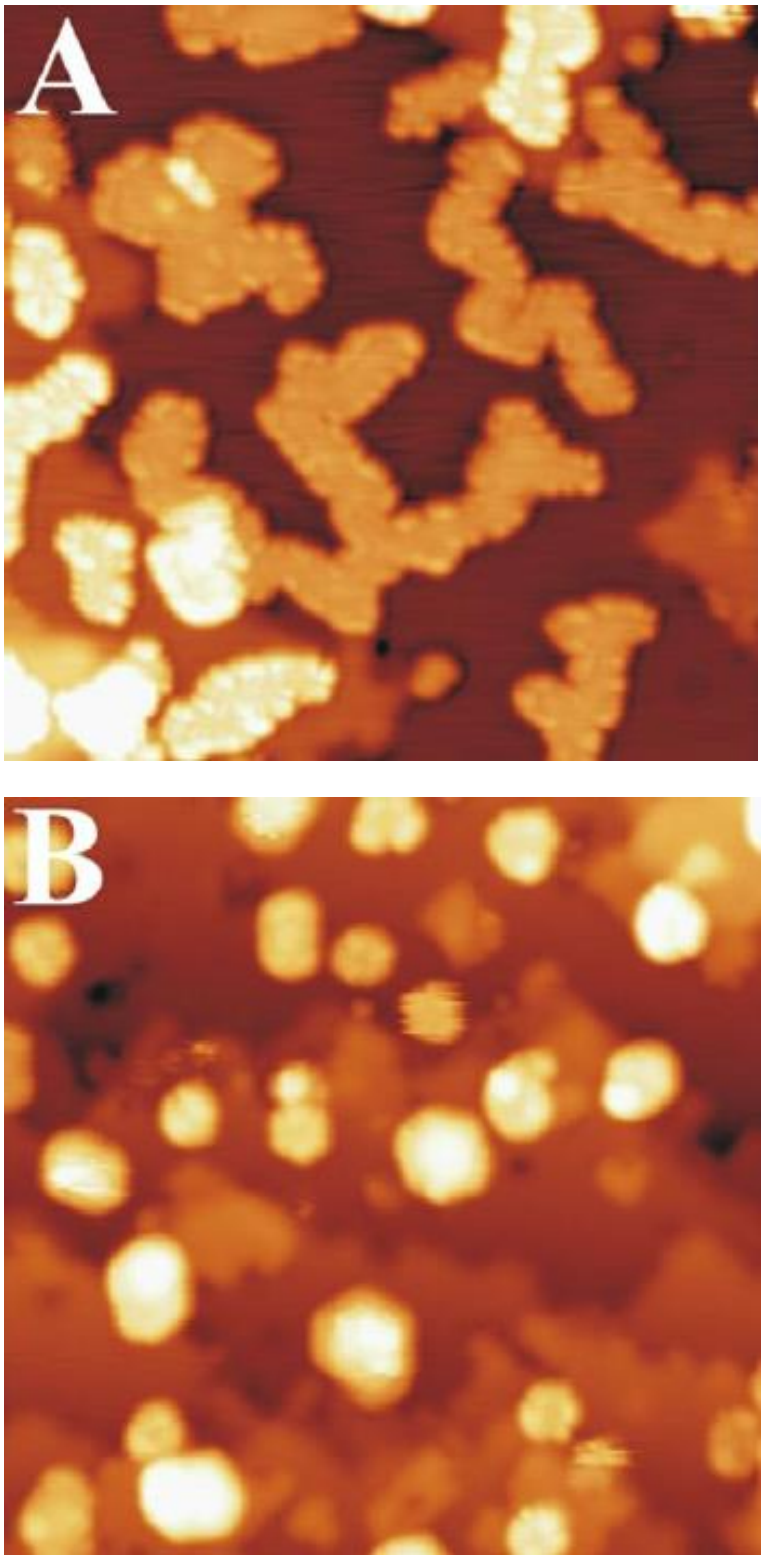

Figure 1.6 STM images of Au deposits on (a) 3ML and (b) 8ML MgO/Ag (001). [11] Copyright (2007) by The American Physical Society

enables the reactivity and selectivity of these oxide thin film based catalysts to be controlled by simply changing the thickness of oxide thin films.

1.3 Industrial Methanol Synthesis

In 1924, methanol was first produced through the destructive distillation of wood wastes. As the development of methanol catalysis, the large-scale synthesis of methanol became possible and was first carried out by B.A.S.F.. A large number of catalysts have been proposed and investigated for methanol synthesis, but only those containing ZnO or CuO proved to be practical in industry. It is interesting to note that the catalytic activity of pure ZnO or CuO is fairly low, whereas the mixture of both oxides shows much higher reactivity and stability.

Zinc oxide is definitely the most selective among all the individual catalysts for methanol synthesis, since certain forms of ZnO could produce methanol without any side products at temperatures lower than 380 ℃. The great activity of special ZnO forms is ascribed to its small crystalline size, and the deactivation is found to be related to the increased size of individual crystals. That is why the most durable catalysts always show relatively low variations in crystal size with reaction time. [40, 41]

Due to this high selectivity, many research groups have paid attention to ZnO based mixed catalysts. Up to the present, Cu/ZnO and Cu/ZnO/Al_2O_3 catalysts have shown to possess the highest selectivity and activity. Have been mainly used in methanol industry for decades, the mechanism for methanol synthesis, the nature of the active sites and the role of the support substrate on these catalysts are still debatable, since it is always hard and complex to study the chemical reactions on active sites underlining heterogeneous catalysts and most of the surface analytic techniques such as X-ray photoelectron

spectroscopy (XPS), thermal desorption spectroscopy (TPD) usually require ultrahigh vacuum (UHV) conditions. [42, 43] On Cu/ZnO and Cu/ZnO/Al_2O_3 catalysts, many different active sites have been proposed in previous studies, such as the Cu/ZnO interface, strained Cu particles, or metallic Cu. Unfortunately, the role of Cu in all the above proposed active sites is always overlooked, which could not explain why ZnO support is essential to the reactivity of methanol synthesis.

In methanol synthesis, Au/ZnO was found to have similar high selectivity and reactivity to the industrial Cu/ZnO catalyst. Besides methanol synthesis, Au /ZnO was also reported to possess similar reactivity and selectivity in water shift reactions. The above interesting findings reflect some unknown internal connections between these two ZnO supported catalyst system. That is why our research work focuses on the ZnO supported system, in order to find the atomic structure of active sites and the multiple processes for methanol synthesis from CO hydrogenation.

1.4 Overviews

In the following chapters, we will present the experimental results of important model catalysts Cu on ZnO, Au on ZnO, and Cu on TiO_2. Not surprisingly, two ZnO supported systems really possess many similarities, especially in surface structure and catalytic reactivity. These interesting results in agreement with previous studies are very helpful to reveal the unique properties of ZnO, especially its diffusion and catalytic properties. On the other hand, ZnO and TiO_2 are very important catalyst substrates in industry, and both of them have a bandgap of 3.2 eV. The big difference between Cu on ZnO and Cu on TiO_2 demonstrates the important role of ZnO support, which plays a decisive role in the CO oxidation reactions.

In these three systems, the surface structure of the prepared samples is highly sensitive to the experimental conditions. The high temperature pretreatment could induce the encapsulation of metal nanoparticles by the oxide supports, which provides a strong indication of the SMSI effects in the interface. As introduced above, the modification of atomic and electronic structure would result in different chemical and physical properties, leading to different reactivity and selectivity of the prepared samples. Unfortunately, it is always hard to study the encapsulation layers in atomic scale, which is highly related to the complex interfacial interaction.

Among these samples, the Cu on TiO_2 could be taken as a classical SMSI case and favors the reduction treatment to form the SMSI in the interface. Based on our experimental evidence, the encapsulation of Cu clusters by reduced TiO_x ultra-thin films are found to enhance the CO oxidation rate. The Cu clusters preferred to be oxidized by the O atoms from TiO_2 bulk rather than the O atoms from gas phase during the oxidative pretreatment. That is because TiO_2 is reducible oxide and could donate the oxygen ions to form new chemical bonds with Cu. In contrast, a higher activation barrier is required for the dissociation of oxygen molecule from gas phase. Similar to other TiO_2 supported metal nanoparticles systems, the interfacial charge redistribution induced by charge transfer should be considered to be the main cause for encapsulation and the improved catalytic reactivity.

The ZnO supported systems are differing from Cu on TiO_2 samples, and that is because ZnO is non-reducible oxide. As a consequence, the diffusion of ZnO favors the oxidative conditions, instead of the reductive conditions. That is why the introduction of oxygen at high temperature could greatly improve the ZnO diffusion and thus largely

decrease the encapsulation temperature. The fully encapsulated Cu on ZnO and Au on ZnO are found to possess the highest CO oxidation rates, although the size of metal clusters is much larger in these samples. In comparison with other samples, the encapsulated ones have a relatively simple surface structure, in which the metal clusters are fully buried by ultra-thin ZnO films. In other words, the outer layer of the whole surface is only composed with ZnO. On the other side, the theory of size effect of metal nanoparticles is in contrast to our experimental results, and the reactants (CO, O_2) could not be bond to the buried metal clusters. In addition to the above differences, the two encapsulated ones show very similar CO oxidation rates, which lead to a new hypothesis that the ultra-thin ZnO films should be responsible for the exceptional catalytic reactivity. Compared to TiO_2, no papers have been published about the encapsulation behavior of ZnO on a model catalyst. It is very difficult to explain why the ultra-thin ZnO films possess these unique properties, which largely differ from those of ZnO bulk materials. It is important to notice that the ultra-thin ZnO films have an irregular shape and relatively strong interaction in interface. In this dissertation, we are trying to construct the bridge over this gap and demonstrate a probable 'size effect' of metal oxide. Together with previous reports, our experimental results do show that the unique properties of ultra-thin ZnO films result from the interfacial charge transfer and their special size.

In a brief summary, we will show how the diffusion of ZnO creates the active sites on the above ZnO supported samples and how the different pretreatments modify the atomic and electronic structure of surface, resulting in different catalytic performance. At the end, we will summarize the unique properties of these ultrathin ZnO films and provides possible reasons for the exceptional chemical performance. Surely, our experimental

findings would open new chapter for mechanism of methanol synthesis, since the migration of ZnO creates the active sites, deviating from previous theories.

Chapter 2: Experimental Principles and Instrumentation

2.1 Introduction

In this chapter, several experimental techniques and methods are involved and the details would be discussed in theoretical principles, experimental setup and methodology. In addition to the widely used ultra-high vacuum (UHV) techniques and important sample preparation methods, Electron Energy Loss Spectroscopy (EELS), Scanning Tunneling Microscopy (STM), Photoemission Spectroscopy (PES) and Low energy Ion Scattering Spectroscopy (LEIS) are also employed to characterize the samples in our experiments, which offer new pathways to understand the nature of the exact surface of prepared samples.

2.2 UHV Chamber

The modern surface science is based on the UHV conditions, which are required for most of the surface analytic techniques. In order to inhibit the adsorption of molecules in the air, the base pressure of a UHV chamber needs to be as low as 10^{-10} Torr. At a pressure of 10^{-6} Torr, one layer of gas could be adsorbed on the surface in 1 second. That is also the definition of Langmuir, $1L=10^{-6}$ Torr s. So it is clear that UHV pressure is a factor 1000 lower, which means hours are needed before the sample is significantly degraded. Therefore, this length of time is possible to suffice the surface experiments.

A lot of special procedures of pumping are needed to achieve UHV, because of the importance of UHV. First, a rotary pump is used to pump down the chamber to 10^{-3} Torr and then a turbo pump could pump it down to 10^{-7} Torr. After such a low pressure is achieved, an ion pump starts to work at 7kV. At this stage, the whole chamber is enclosed for bakeout. This period will last for a day or more at least 100 ℃, which could remove

gas atoms sticking to the chamber walls, especially water. After cooling down to the room temperature, the chamber could achieve a UHV pressure.

2.3 Surface Cleaning

The samples used in this work are ZnO (10-10) and TiO_2 (110) single crystals with a size 10mm x 10mm x 0.5mm, purchased from MTI Corporation. The sample surface is cleaned with cycles of sputtering (1-2 kV Ne^+, I~10-20 μA, 30 min) and annealing (650 ℃, 30 min). All the temperatures are monitored with a k type thermocouple. The sample is heated by a W filament, and a high voltage of hundreds of volts is applied to accelerate the electrons from the filament to hit the sample. And then LEED is employed to check the surface order and cleanliness. The cycles of cleaning will be not completed until the good LEED pattern is observed.

2.4 Low Energy Electron Diffraction (LEED)

LEED is a surface-sensitive technique for detecting the surface structure of crystalline materials. With a collimated beam of low energy electrons, the diffracted electrons are observed as spots on fluorescent screen. For more than half century, LEED is always the principal method to study the morphology of 2D plane surfaces. In our experiments, an ErLEED 150 reverse view LEED optics and ErLEED 1000A power supply are installed in this LEED system. The range of the whole optics could be up to 100mm in the chamber, while the energy of electron beams could be increased to 1000 eV. The typical LEED apparatus is shown in Figure 2.1. For LEED, single scattering is the main kinematic theory. The wavelength of electrons could be presented as de Broglie relation: $\lambda = h/p$ and $p = \sqrt{2mE}$, where p is electron momentum, m is electron mass, E is kinetic energy of electron. So it could be concluded that $\lambda = \frac{p}{\sqrt{2mE}} = \sqrt{\frac{150.4}{E}}$, after

plugging in the constant *h* and *m*. In our case, the LEED pattern directly shows the symmetry and periodicity of the ZnO surface. As shown in Figure 2.2, the image is the clean ZnO (10-10) with (1x2) pattern. After dosing atomic hydrogen, the surface is (1x1)

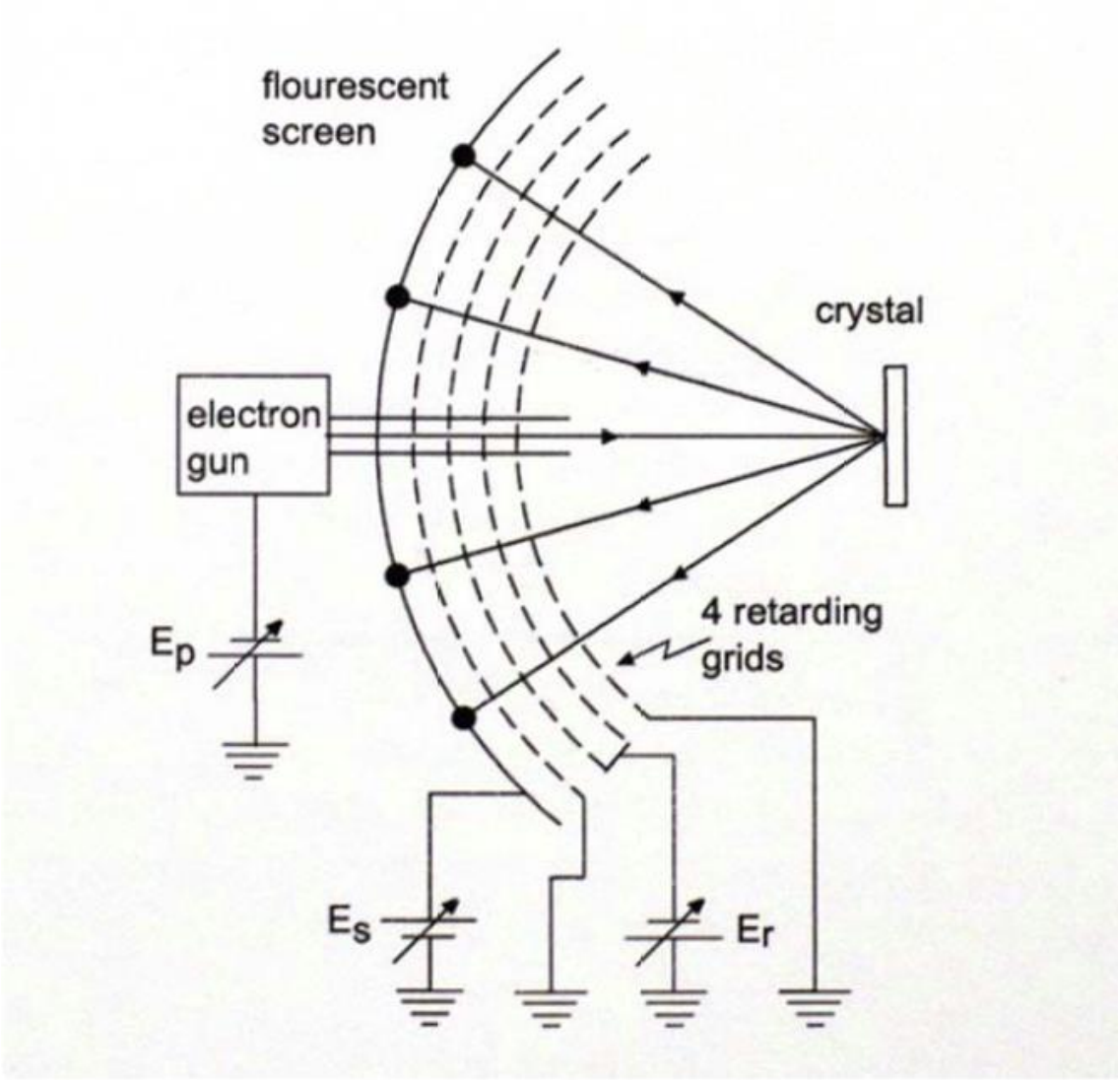

Figure 2.1 a typical LEED apparatus [44]

pattern in Figure 2.3. The above change shows the reconstruction is induced by the new formation of OH bond on ZnO surface.

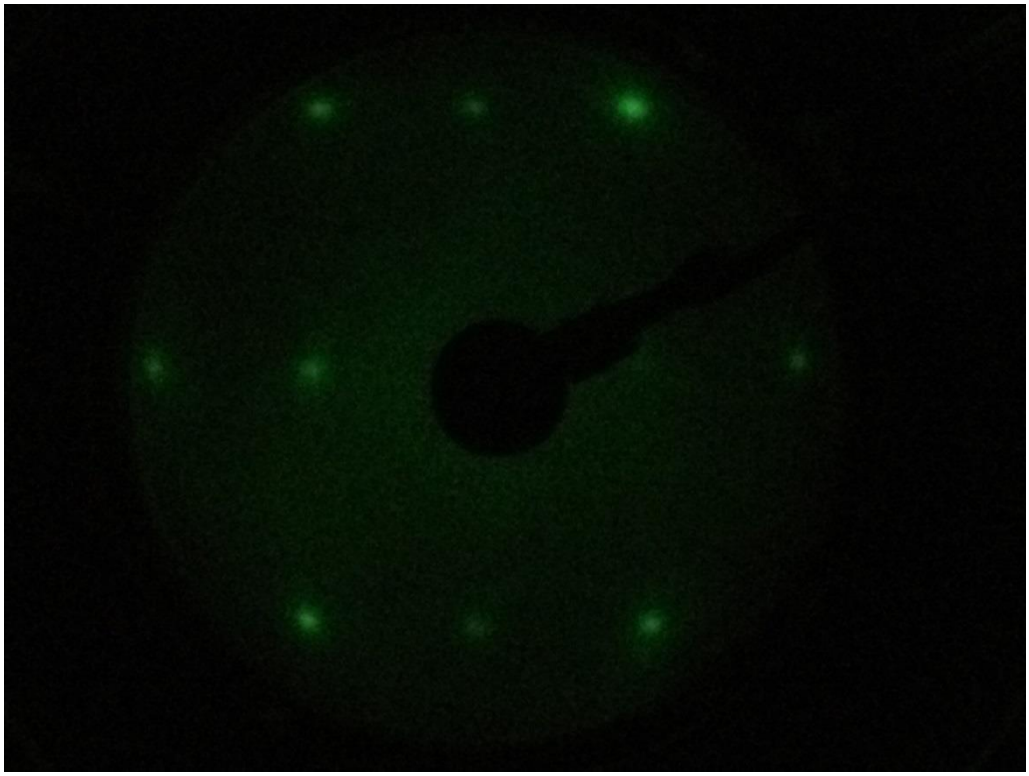

Figure 2.2 LEED pattern of ZnO (10-10)

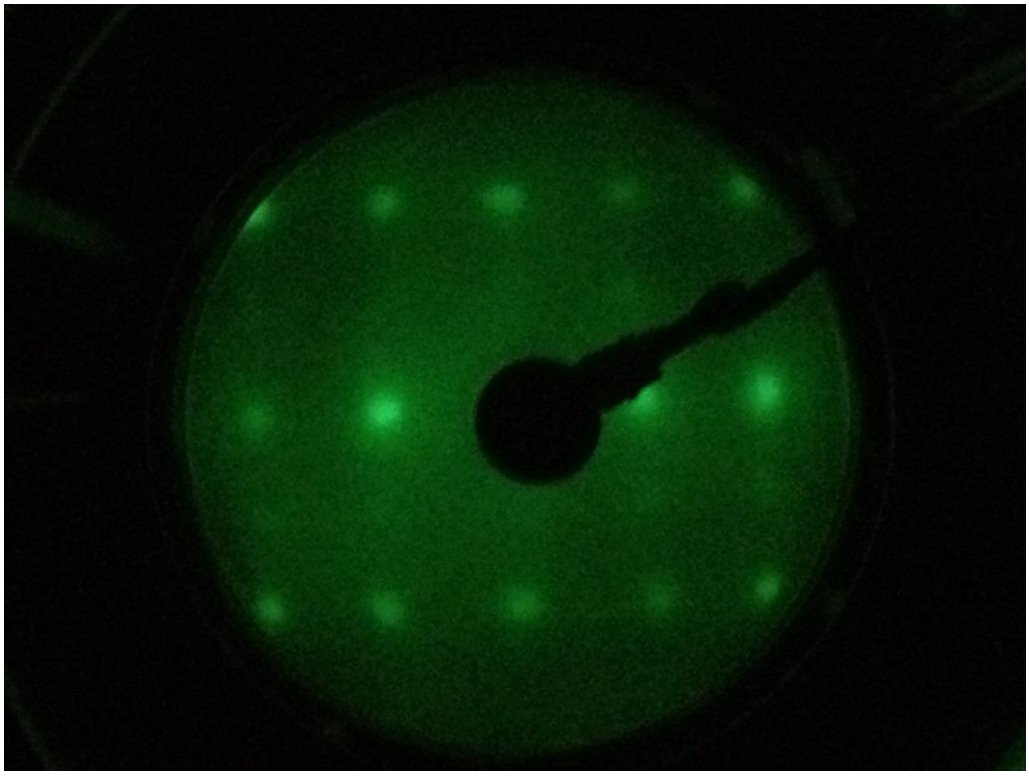

Figure 2.3 LEED pattern of ZnO (10-10) after dosing H atoms on the clean surface

2.5 High Resolution Electron Energy Loss Spectroscopy (HREELS)

2.5.1 Introduction

EELS was first developed in the middle 1940s and became widely used in the 1990s after the development of ultra-high vacuum technology. As a powerful surface technology, it plays a decisive role in studying the surface or the adsorbates to the surface, based on inelastic scattering of low-energy electrons.

When an incident electron beam with energy E_0 is scattered on the surface, it can cause the excitation and suffer an energy loss ΔE. Then the electron beam with energy E_0-ΔE will be back scattered into the chamber. The energy loss ΔE could offer the information about the ionic vibrations of the materials or the vibrational frequencies of the adsorbates to the surface. The surface sensitivity is highly relevant to the angle of the incident electron beam and the low energy of the incident electrons. Normally, the interaction between the incident electrons and the excitations are mediated through two types of scattering mechanisms: dipole scattering and impact scattering. In Figure 2.4, it shows how the absolute intensities are influenced by the off-specular angle for dipole scattering and impact scattering.

2.5.2 Dipole Scattering

In dipole scattering, the incident electron, kind of an electromagnetic wave, interacts with oscillating dipoles at long range induced by the vibration of the surface species. According to previous studies, Dipole scattering is known to follow the harmonic-oscillator infrared selection rules: (i) it allows just the fundamental transitions; (ii) vibrations could be only induced by a change in dipole moment. [45]

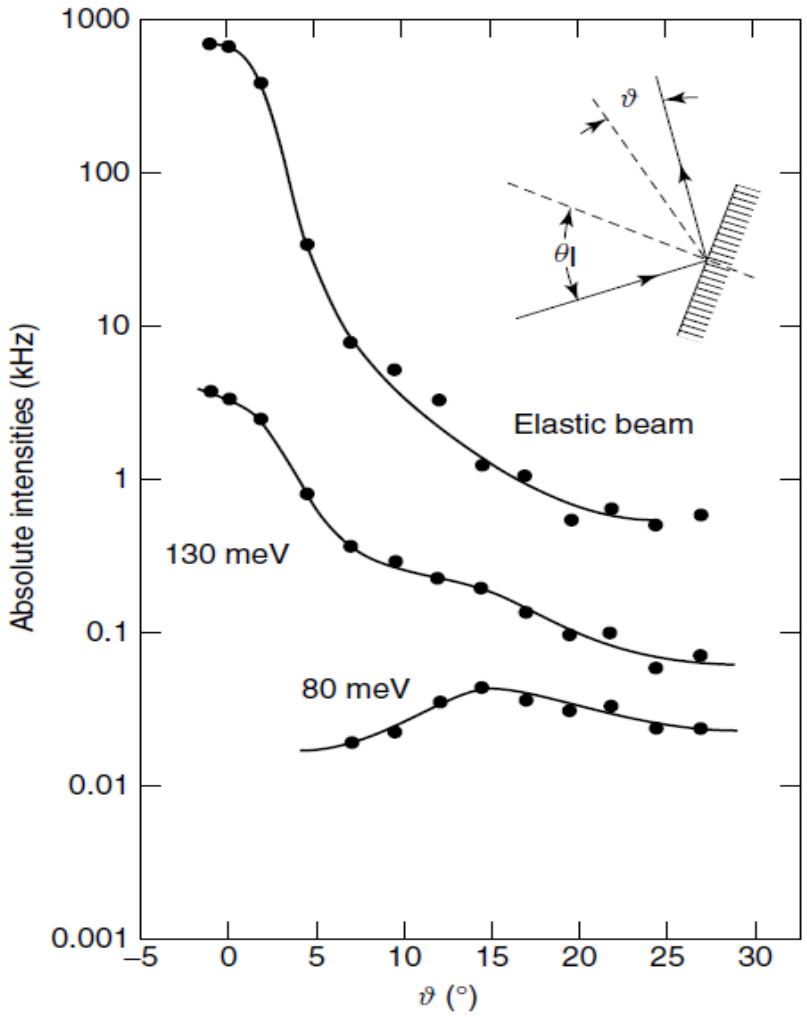

Figure 2.4 The influence of off-specular angle (ψ) on the absolute peak intensities in dipole scattering (130 meV) and in impact scattering (80 meV). [45]

In metal materials, electromagnetic waves are generated normal to the surface. In surface-parallel orientation, the dipole moment could be cancelled due to its image dipole. In the vertical direction, however the dipoles from the surface and image are working together to reinforce the electric dipole moments as shown in Figure 2.5. As a consequence, only the induced dipole moments normal to the surface could be excited and observed.

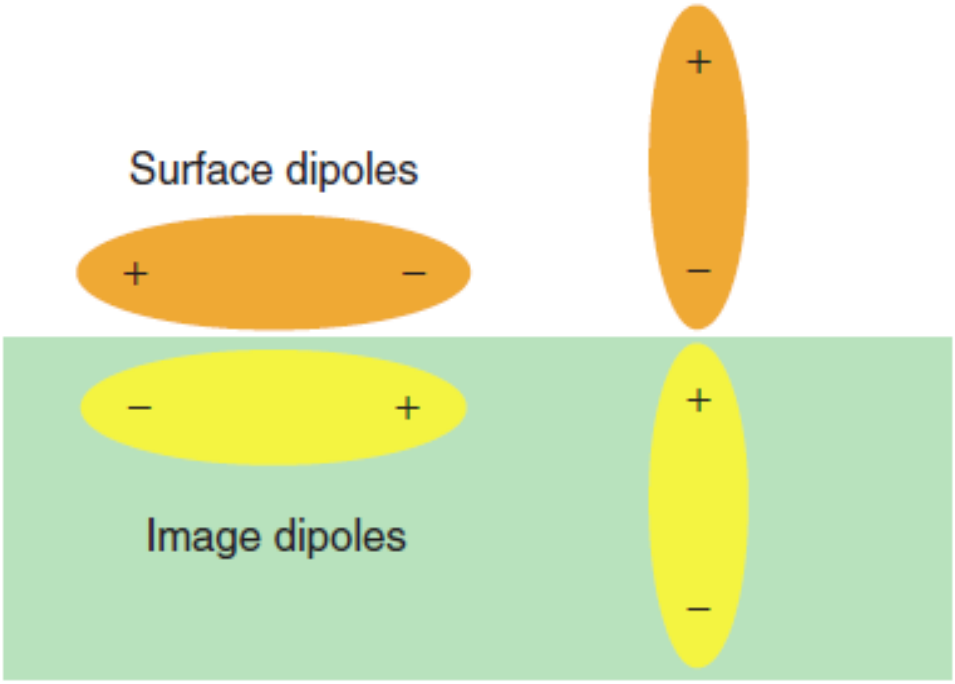

Figure 2.5 The dynamic electric moment of the dipole oriented parallel to the metal surface is cancelled by that of its image dipole. In the vertical orientation, the dynamic electric moments of the surface and image dipoles reinforce each other. [45]

2.5.3 Impacting Scattering

Different from the long-range dipole scattering, impact scattering are normally complex and the above selection rules cannot be simply applied to impact scattering. The incident electrons in impact scattering are scattered in inelastic way from the core of a surface atom or an adsorbed molecule to the surface. It is usually short range interactions and the incident electrons are possible penetrate into the adsorbed molecule. The quantum formalism has applied to impact scattering, in order to satisfy the theoretical requirements. Moreover, the impact scattering is governed by the "propensity rules": (i) impact scattering is dominant in HREELS; (ii) impact scattering is cancelled in the specular direction; (iii) in contrast to the dipole scatterers, strong impact scatterers are always weak dipole scatterers. [45]

2.5.4 Experiment Setup

The instrument in our lab is the HREELS LK 2000 DAC by LK technologies. Its maximum resolution could be 3 meV (FWHM) and its beam energy could range from 0 to 240 eV. The sample bias is ±15V and all the data acquisition could be down by the associated software. The instrument is shown in Figure 2.6.

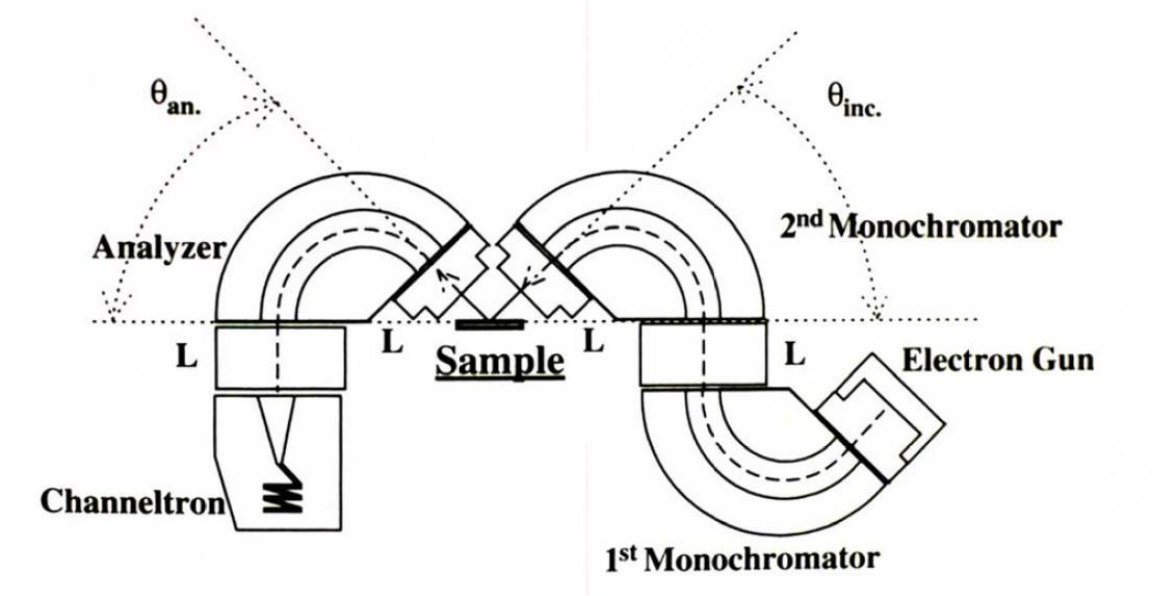

Figure 2.6 Schematic cross section of the LK 2000 HREELS [35]

2.6 Photoelectron Spectroscopy (PES)

PES is a useful tool to study the electronic structure of the materials, which provides the information of their internal electronic properties. PES techniques are developed based on the photoelectric effect, first discovered by Henrich Hertz in 1887. [46] Angle resolved photoemission spectroscopy (ARPES) is powerful in mapping the electronic structures of the material in k space. A schematic of geometry of ARPES experiment is shown in Figure 2.7, and it applies to ultraviolet (UV) light with photon energies less than 100 eV. Figure 2.8 shows the "Universal" curve reflecting the electron escape depth

for different materials. It is obvious that the electron escape depth is varying with the type of materials and electron energy. For photon energies between 20 and 200 eV, the electron escape depth is less than 1 nm, only a few atomic layers on the top surface.

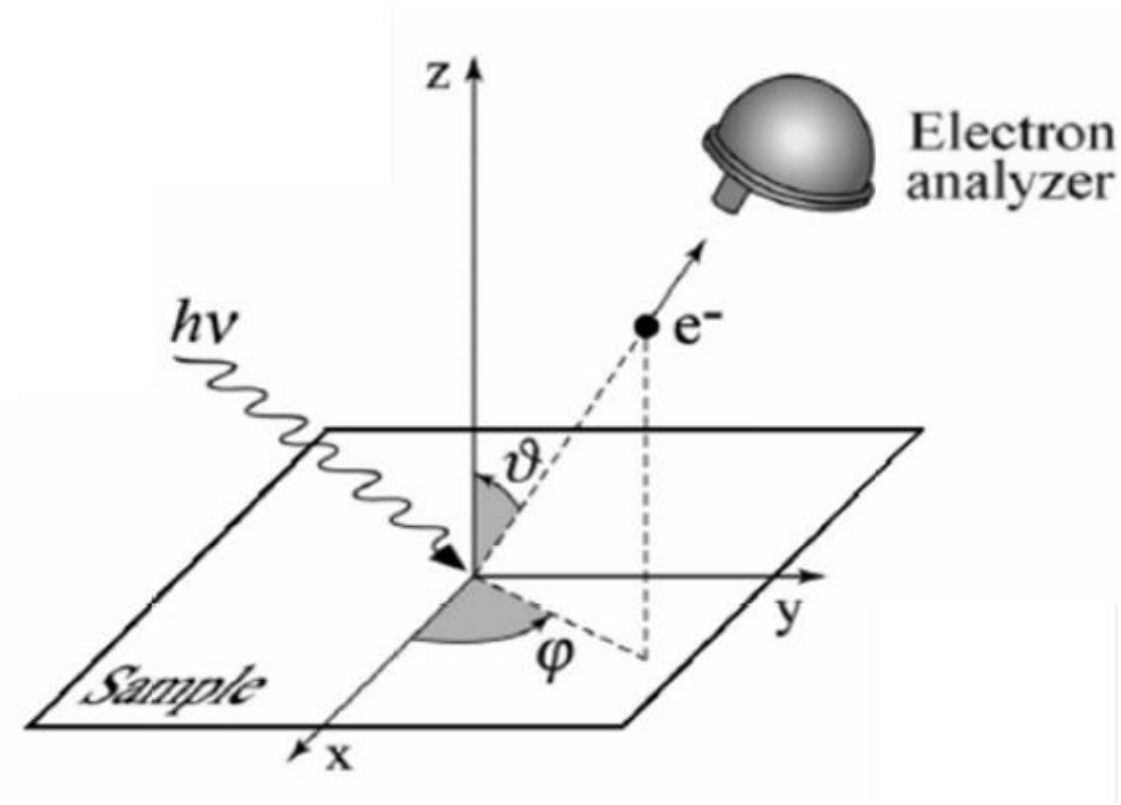

Figure 2.7 Schematic of geometry of ARPES experiment [47]

2.7 Low Energy Ion Scattering (LEIS)

LEIS, also called ion scattering spectroscopy (ISS), is a useful tool to offer insight into the chemical composition of the outer atomic layer. The outer surface always dominates the adhesion as well as catalysis processes, and that is why the chemical industry challenges are always relate to surfaces. It has been applied to study all types of materials, metals, semiconductors, and even ceramics. The only restriction, similar to other surface analysis techniques, is vacuum and the low materials vapor pressure to sustain vacuum.

Thanks to the penetration property of the ions, it becomes possible to detect the surface information in-depth, normally few layers below the surface.

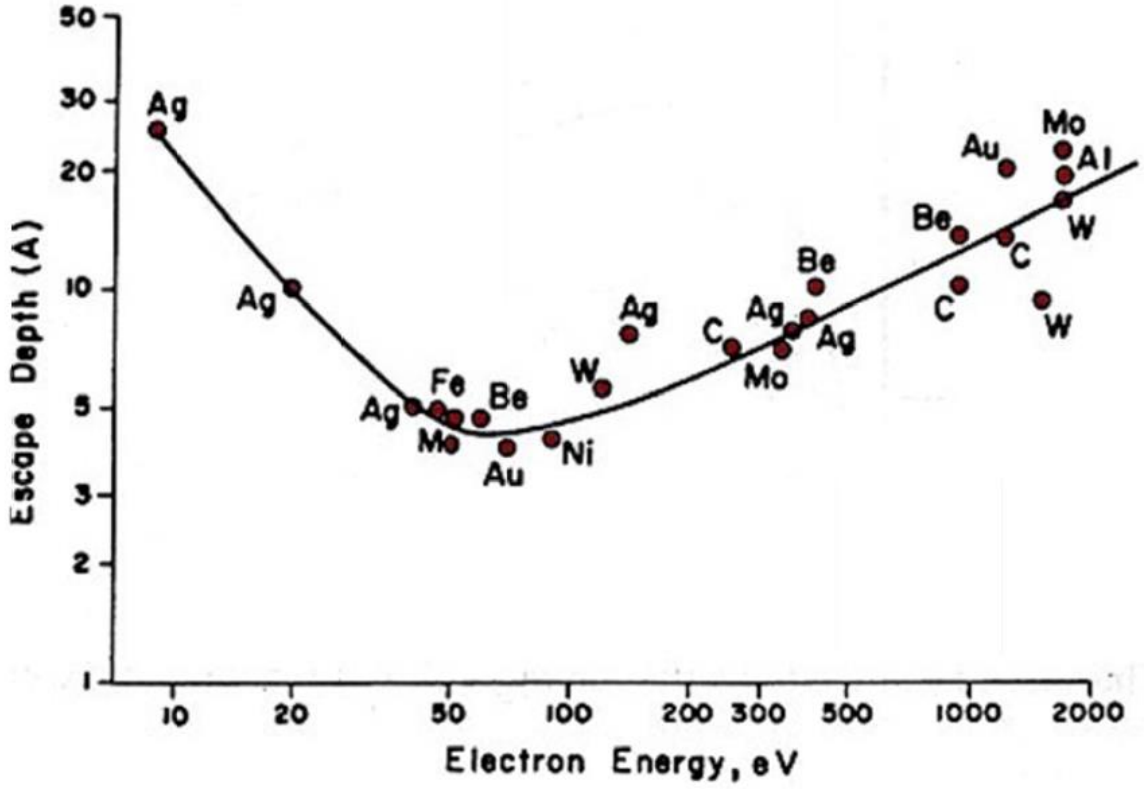

Figure 2.8 Universal curve of electron escape depth as a function of kinetic energy [48, 49]

2.7.1 Binary collision peak

In an elastic binary collision, consider a particle with mass m_1 as well as primary energy E_0, and another particle with mass m_2 at rest. The energy transfer between two particles is just dependent on the scattering angle θ. The kinematic factor k, which is defined as the ratio E_f/E_0, could be calculated from energy and momentum conservation.

$$E_f = k * E_0 = \left(\frac{cos\theta \pm \sqrt{\left(\frac{m2}{m1}\right)^2 - sin^2\theta}}{1+\frac{m2}{m1}} \right)^2 * E_0$$

So it is easy to conclude that heavier atoms always have higher energy scattering peaks while lighter atoms is corresponding to lower energy peaks.

As shown in Figure 2.9, 3 keV He^+ ions are scattered by a pure Al target. [50] The highest peak is due to binary collision and the signal at higher energies is ascribed to plural scattering, which is caused by double and multiple scattering. The broad peak at lower energies results from deeper layers' backscattering.

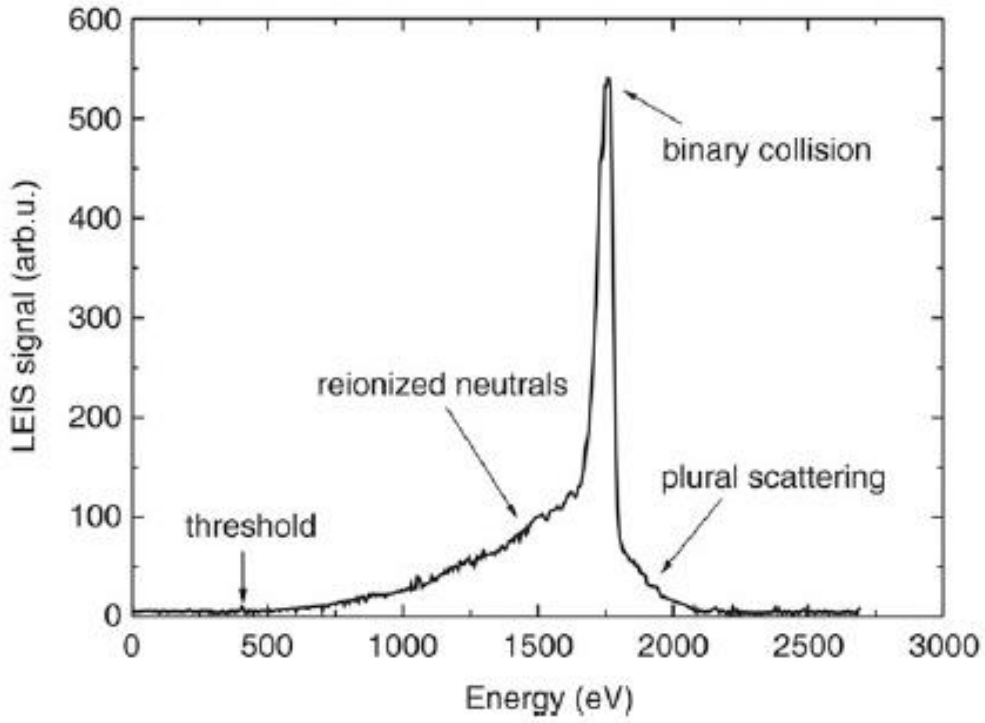

Figure 2.9 LEIS spectrum of 3keV He^+ scattered over 142 °by polycrystalline aluminum. [50]

2.7.2 Analysis Of Chemical Components Of Atomic Surface Layer

Normally, the atomic surface concentration N_i is defined as

$$S_i = \frac{I_p}{e} \cdot t \cdot \varepsilon \cdot R \cdot N_i \cdot n_i,$$

S_i: the yield of ions; I_p: the primary ion beam current; t: the acquisition time; ε: an instrumental factor determined by detector and analyzer; R: a factor, which depends on surface roughness and the shielding effects by neighboring atoms; n_i: the elemental sensitivity factor. The quantitative analysis is always difficult, since the surface sensitivity of LEIS is dependent on a few elements: incident ions, ion energies and scattering angles. [51, 52] In principle, the area of peak could be the proper physical parameter to analyze the surface composition.

2.8 Scanning Tunneling Microscopy (STM)

As a unique and powerful tool in surface science, STM is applied to explore a wide variety of surfaces at the atomic level. In a simple STM, a sharp metallic tip is brought very close (around 5 Å) to the conducting sample surface and then the wave functions of tip starts to overlap the sample. When the bias voltage is positive, electrons start to tunnel from the tip to the sample. The induced tunnel current strongly depends on the distance between the sample and the tip. If the current remains constant, a feedback loop adjusts the distance and the height modulations are recorded. By these height modulations, it becomes possible to make a tgeographic image of the surface.

As discussed above, the image of STM is highly dependent on the tunnel current. Thus it becomes necessary to know the factors, which determines the tunnel current. In first-order perturbation theory, the tunnel current could be expressed as

$$I = \frac{(2\pi)^2 e}{h} \sum_{\mu\upsilon} f(E_\mu)[1 - f(E_\upsilon + eV)] \times \left|M_{\mu\upsilon}\right|^2 \delta(E_\mu - E_\upsilon) \qquad (2.1)$$

Where $f(E)$ is the Fermi function, $M_{\mu\upsilon}$ is the tunneling matrix element between the tip states φ_μ with energy E_μ and the sample states φ_υ with energy E_υ, V is the bias voltage

between the sample and the tip. The tunneling occurs from filled tip states f (E_μ) into empty sample states 1- f (E_υ + eV). After introducing the Bardeen theory and the model of a tip by Tersoff-Hamann, the above function could be simplified as:

$$I \propto V \sum_v |\varphi_v(\overrightarrow{r_0})|^2 \, \delta(E_\mu - E_v) = V\rho(E_F, \overrightarrow{r_0}) \qquad (2.3)$$

Here ρ(E) is the LDOS (local density of states) at or very near the surface and a constant density of states for the tip is assumed. Within this approximation, the STM images could be made in the constant current mode, in agreement with the LDOS of the surface. In Figure 2.10, a typical setup of STM is shown based on the constant current mode. In our experiments, the Omicron VT STM is employed to investigate the surface structure. Here,

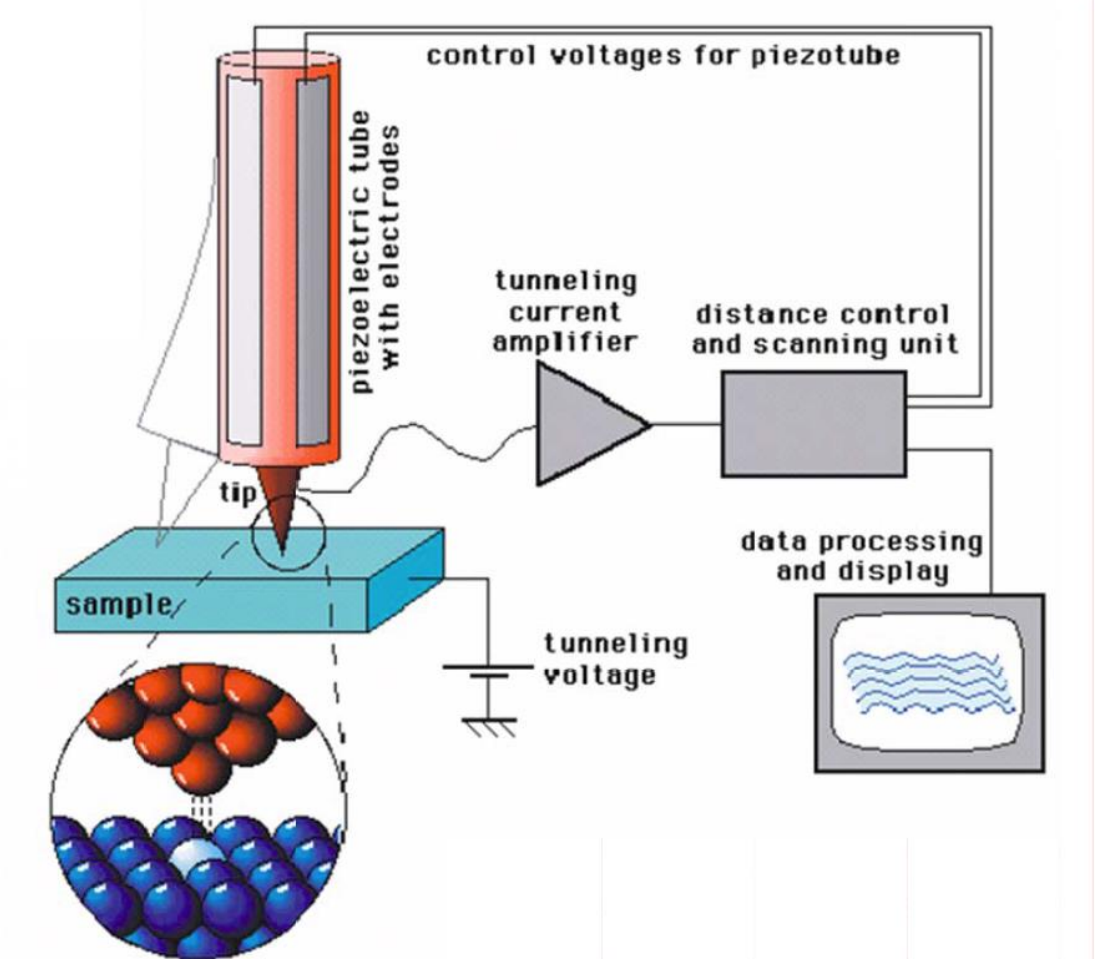

Figure 2.10 Schematic of a typical STM set up. [53]

the Omicron VT STM is an UHV scanned probes microscope equipped with a Q-plus sensor for AFM, operating in a variable temperature range from 50K to 650K. The Omicron UHV chamber is connected to our preparation chamber, in order to protect the prepared samples. In the following chapters, we will show the surfaces of different prepared samples, which offer the internal information of the growth model of metal adatoms under different pretreatments.

2.9 Batch Reactor

The ideal batch reactor is usually used to maintain the mixture of reactants for the desired reaction and keep the reactants in intimate contact with the designed catalysts at the given experimental conditions, such as temperature and pressure. The batch reactor is composed of simple equipment and especially suitable for small production of chemical reactions. In surface science, a typical bath reactor consists of a tank with heating system and is generally used for simple chemical reactions such as CO oxidation. In our system, a fixed chamber with a volume of 2.3 Liter is set up for batch reactor and a Ta wire insider is used to heat the prepared sample. The reactants ($CO+O_2$) would be pre-mixed at a constant ratio (2:1) and stored in a glass bottle. After the reaction chamber is pumped into UHV, the reactants are filled into the reactor by measuring the pressure of the gases. Next, the prepared sample is heated to the proposed temperature and the pressure of the chamber is recorded by the computer program. In a simple CO oxidation experiment: $2CO + O_2 = 2CO_2$, the change of the chamber pressure is used to calculate the yield of CO_2. It is important to notice that the reaction time is relatively short and the change of pressure induced by the gas heating could be ignored.

Chapter 3: Cu on ZnO

3.1 Introduction

In the last decades, ZnO has attracted a lot attention, and its wide range of potential applications becomes more and more practicable. ZnO has a wide band gap (3.37 eV) and a very large exciton binding energy of 60 meV. The above specific properties enable ZnO to be an alternative material for light-emitting devices (LED) and laser in ultraviolet (UV) region. In 1986, Drapak had made hybrid heterostructure LEDs with p type layer Cu_2O on n type ZnO. [54] In 1997, the scientists in Hong Kong and Japan had observed the optically pumped excitonic UV laser emission from the prepared ZnO thin films. [75, 76] Based on this interesting UV emission, Peidong Yang *et al.* had prepared ZnO nanowires in 2001 on sapphire substrates and used the prepared samples to make room-temperature UV nano-laser. The lasing action was observed at 385 nm, with an emission linewidth of less than 0.3 nm. [55]

Owing to the above developments, more and more groups start to focus on novel nanostructures of ZnO, because of its various highly ordered nanowire arrays, nanorods, tower-like structures, nanobelts, nanobows, nanorings, and nanosprings. [56, 57, 58] Some of these groups have developed new applications of these nanostructures, especially in gas sensors and bio-sensors, such as NO_2, NH_3, CO, H_2O, and C_2H_5OH. [59, 60, 61, 62] Recently, Zhonglin Wang has found another important application of these nanostructures, which is used to make nanodevices with piezoelectric ZnO nanowires to transfer mechanical energy into electrical energy, which offers promising new insight of renewable energy sources. [64] Addition to the above applications, the most popular potential application of these nanostructured ZnO is working as photocatalysts, especially

in dye sensitized solar cell (DSSC). The electron injection is ultrafast in nanoporous ZnO films from the dye into the conduction band of ZnO, which supposes to have better catalytic performance than TiO_2 based DSSC. In addition, ZnO with high surface area possesses higher charge carrier mobility, leading to higher dye-sensitization and light harvesting. Due to the above advantages, ZnO is widely considered to be a potential electrode material in DSSC. [65, 66, 67]

3.2 Electronic Structure

The band structure of a certain semiconductor plays a decisive role on its electronic structure and subsequently its potential applications. Consequently, it becomes critical to understand the band structure through accurate measurements, especially under UHV conditions. The polar (0001)-Zn, $(000\bar{1})$-O and nonpolar $(10\bar{1}0)$ ZnO surfaces have always been the most important topics in recent experimental and theoretical works. The nonpolar ZnO $(10\bar{1}0)$ surface has a particular advantage over the other two surfaces at surface chemistry, since its surface is terminated with both O and Zn atoms. The relaxation of the surface could be characterized by downward shifts of both O and Zn atoms on the surface and the shift of Zn atoms are found to be greater than that of O atoms. Therefore, it results in a Zn-O bond rotation by $6.2°$ or $11.5°$ and the O 2p dangling-bond state is stabilized through this ZnO relaxation. [68, 69] As shown in Figure 3.1, the detailed ARPES studies were performed on ZnO $(10\bar{1}0)$ surface and revealed that two dimensional band structures of O 2*p* dangling-bond state were localized along the symmetry axes of the surface Brillouin zone (BZ). [70] In this paper, Ozawa also measured the surface localized O 2*p* dangling-bond states, which existed at 3.7 eV below the Fermi level at the Γ point and shifted to higher binding energy by 0.8 and 0.5

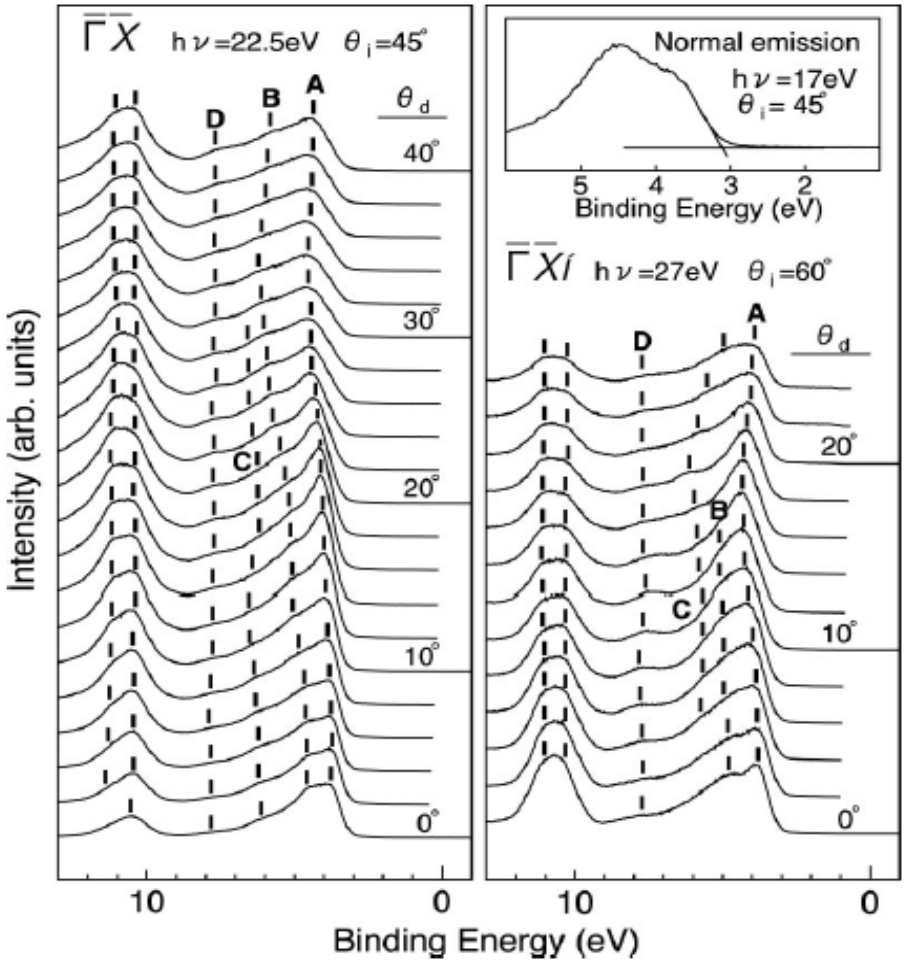

Figure 3.1 Off-normal emission spectra of the clean surface recorded at *hv*=22.5eV and θ_i=45 ° along the [12-10] direction (left) and at *hv*=27ev and θ_i=60 ° along the [0001] direction. (right) [70]

eV along ΓX and ΓX' axes, respectively. (Figure 3.2) The above studies offer us probable pathways to learn the electronic structure of ZnO ($10\bar{1}0$), which determines its potential applications.

3.3 Nature Defects

(1) Zinc interstitials

As shallow donors, the Zn interstitials have a characteristic "effective mass" (EM) *g*-factor of 1.96. [71] In n-type ZnO, higher formation energies are found for Zn interstitials,

which are fast diffusers has migration barriers of 0.57 eV. [72] As shown in the proposed experiments, they are not stable at room temperature and could not diffuse into the ZnO

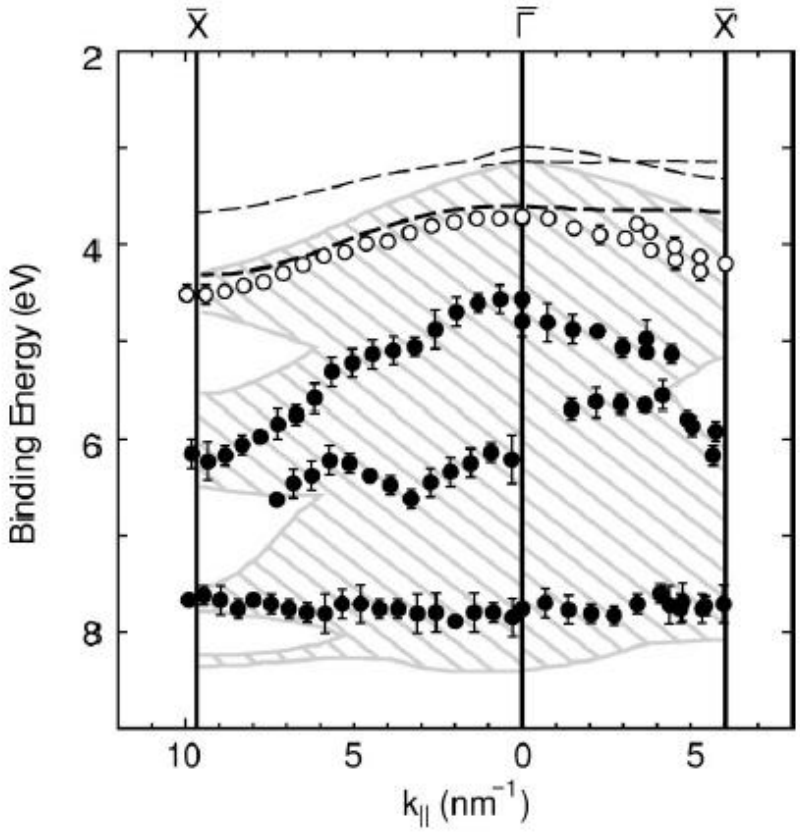

Figure 3.2 Measured dispersion of the O *2p* dangling-bond state (open circle) and the bulk related states. [70]

crystal. [73, 74] Based on the above consensus, the Zn vapor was supposed to react with O to form new ZnO species on the surface, which brings an increase of O vacancy density to the bulk. [75]

(2) Oxygen vacancies

Oxygen vacancy is always a popular topic in metal oxide materials, and it plays a significant role in modifying the electronic structure, and subsequently its catalytic performance. Oxygen vacancies have been suggested to be the active sites on ZnO based heterogeneous catalysts, because they are supposed to be the energetically favored

adsorption sites for oxygen molecules and could dissociate oxygen molecule into atomic oxygen. Through the accurate theoretical calculations, the O vacancy of ZnO is a deep, negative donor and remains stable up to 400 ℃, where +1 charge state is thermodynamically unstable. The stable +2 state of O vacancy were supposed to locate at 0.5 to 0.8 eV above the maximum of valence band, while the neutral O vacancy ground state lies at 2.1 eV below the minimum of conduction band. [76, 77, 78, 79, 80] Photoluminescence (PL) experiments have presented the famous green luminescence band around 2.4 eV (510 nm) caused by O vacancies with an excited-to-ground state transition. [81] Another vacuum experiment also produces PL lines at 2.53 eV by annealing ZnO in Zn vapor, which experimentally supports the above hypothesis. [82] Moreover, the above theoretical calculation also shows that the migration barrier for the neutrally charged O vacancy is 2 eV. [83]

(3) Zn vacancies

Zn vacancies are double acceptors and their negative charge states allow them to be effective trapping centers for positrons. That is why a lot of experiments have focused on positron annihilation spectroscopy (PAS) to investigate the formation of Zn vacancies. Selim *et al.* have found that the Zn vacancies could be simply formed by polishing the crystal. [75] Furthermore, pioneering work by T. Moe Borseth has shown that the Zn vacancies become clustering in the Li-implanted ZnO and He-implanted ZnO, and the vacancy clusters are of larger size than the Zn vacancies. [85] Through the deposition of metal thin films on ZnO crystal, Brillson's studies demonstrate that the metal thin films induce deep level emissions at characteristic energies of O and Zn vacancies related point

defects and the formation of metal-Zn eutectic results in characteristic emissions of Zn vacancies, complexes and/or clusters. [86]

In n type doped ZnO, it is well established that the decisive role of Zn vacancy is responsible for the diffusion behavior of the dopants, especially the group III elements such as B, Al, Ga and In. [91] Through an ab initio calculation, Huang *et al.* have proposed a Zn vacancy-assisted mechanism for dopant diffusion. [101] From their studies, it becomes possible to hypothesize that the dopants diffuse by exchanges between the Zn vacancy and the doped atoms. At the first step, the doped atom migrates to the neighbor Zn vacancy and forms a dopant-Zn vacancy pair as intermediate state. Subsequently, the Zn vacancy dissociates from this neighbor dopant and diffuses to another neighbor dopant. In the following table of Figure 3.3, all the possible binding energies and dissociation barriers are listed. It is not surprising that the migration barrier of Zn vacancy becomes larger, as the size of doped atoms becomes larger. The migration barrier is relevant to the diffusion length of Zn vacancy and therefore determines the formation of Zn vacancy clusters. The above finding explains why a much higher density of Zn vacancy clusters is found in the Li-doped ZnO crystal.

(4) Defect chemistry

How to control defects and charge carriers of the semiconductor materials is the key to apply them to the electronic devices and chemical industry. However, in spite of numerous papers on ZnO, how to connect the properties of defects to their defect chemistry is still under debate. That is because ZnO has a rich defect chemistry system in a very simple chemical formula. Based on the above discussions, it enables us to learn the

TABLE I. Calculated energy barriers and dissociation energy barriers and binding energy in eV for vacancy-mediated migration of B, Al, Ga, and In in wurtzite ZnO.

	Charge state	
Migration path	0	−1
Zn vacancy diffusion with B, Al, Ga, and In dopings		
Zn-V_{Zn}(B): in plane	0.57	0.69
Zn-V_{Zn}(Al): in plane	1.05	1.17
Zn-V_{Zn}(Ga): in plane	1.16	1.27
Zn-V_{Zn}(In): in plane	1.43	1.57
Zn-V_{Zn}(B): out of plane	1.06	0.97
Zn-V_{Zn}(Al): out of plane	1.13	1.01
Zn-V_{Zn}(Ga): out of plane	1.15	1.04
Zn-V_{Zn}(In): out of plane	1.17	1.05
Exchange between Zn vacancy and B, Al, Ga, and In		
B-V_{Zn}: in plane	2.12	2.25
Al-V_{Zn}: in plane	1.80	1.76
Ga-V_{Zn}: in plane	1.51	1.45
In-V_{Zn}: in plane	0.74	0.65
B-V_{Zn}: out of plane	1.21	1.12
Al-V_{Zn}: out of plane	2.33	2.19
Ga-V_{Zn}: out of plane	1.96	1.80
In-V_{Zn}: out of plane	0.99	0.80
Dissociation barrier		
B-V_{Zn}: in plane	1.00	0.94
Al-V_{Zn}: in plane	1.00	0.95
Ga-V_{Zn}: in plane	1.00	0.96
In-V_{Zn}: in plane	1.12	1.09
Binding energy		
B-V_{Zn}	−0.57	−0.66
Al-V_{Zn}	−0.42	−0.52
Ga-V_{Zn}	−0.37	−0.48
In-V_{Zn}	−0.33	−0.43

Figure 3.3 Reproduced with permission from *Appl. Phys. Lett.* **88**, 032106 (2006). Copyright 2006 American Institute of Physics

native states of different defects and the electronic energy levels of various defects of ZnO are exhibited in Figure 3.4. [87] In an actual catalytic reaction, the active sites of most catalysts are always related to the defects, which play a decisive role on the catalytic performance and the reaction pathways. Consequently, the improvements of stability and activity of defects become a popular topic in the demand for new designs of the modern catalysts. In ZnO related cases, many groups have revealed that the defect states are highly dependent on the experimental conditions. For instance, O vacancies become the main defects after heating ZnO in Zn vapor. Therefore, it could help to enable the precise control of the defect states by simply modifying the experimental conditions, because of their significant importance in surface chemistry.

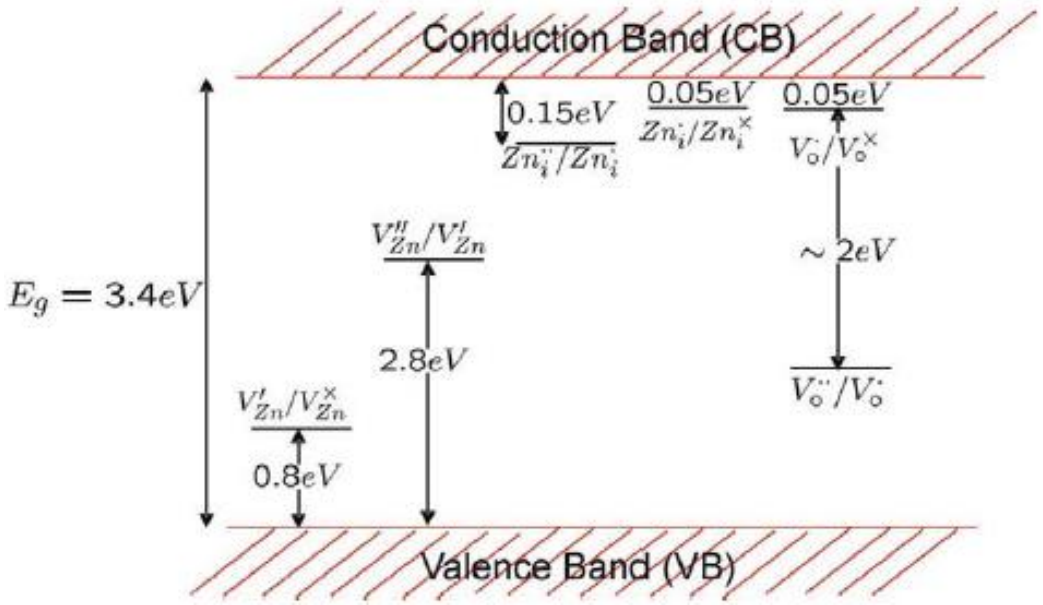

Figure 3.4 Energy levels of native defects in ZnO. [87]

In the following Figure 3.5, possible defect reactions in ZnO are described. [87] It has revealed that the change of defect states may alter the energy barrier of reaction steps, and subsequently lead to different direction of reaction pathways, resulting in unexpected

side products. Therefore, the experimental conditions are of significant importance to the selectivity and stability of ZnO supported catalyst, because of the controllable defect states from the above discussion.

Defect chemistry in ZnO

Zn interstitials come from the Frenkel reaction:

$$Zn_{Zn} \Leftrightarrow Zn_i^X + V_{Zn}^X$$

Further ionization reactions and equilibrium constants are[66]:

$$Zn_i^X \Leftrightarrow Zn_i^\bullet + e' \qquad K = 2N_c \exp(-0.05/kT)$$
$$Zn_i^\bullet \Leftrightarrow Zn_i^{\bullet\bullet} + e' \qquad K = 1/2N_c \exp(-0.15/kT)$$

The oxygen vacancies arise from the Schottky reaction:

$$0 \Leftrightarrow V_{Zn}^\times + V_O^\times$$

Further ionization reactions and equilibrium constants are:

$$V_O^X \Leftrightarrow V_O^\bullet + e' \qquad K = 2N_C \exp(-0.05/kT)$$
$$V_O^\bullet \Leftrightarrow V_O^{\bullet\bullet} + e' \qquad K = 1/2N_C \exp(-2.0/kT)$$

$$V_{Zn}^\times \Leftrightarrow V_{Zn}' + h^\bullet \qquad K = 2N_V \exp(-0.8/kT)$$
$$V_{Zn}' \Leftrightarrow V_{Zn}'' + h^\bullet \qquad K = 1/2N_V \exp(-2.8/kT)$$

Figure 3.5 the defect chemistry of ZnO. [87]

3.4 ZnO Diffusion

From T.A. Merz's work, the nano-mounds are observed on ZnO polar surface, indicative of the diffusion of ZnO atoms or defects. [88] As presented in Figure 3.6, a hexagonal pit is surrounded by nanomounds. The spectra with a peak excitation depth of 20 nm below the surface exhibit optical emissions in a 1.7 to 2 eV DRCLS energy range near these nanostructures. The increased intensity of the black peak is ascribed to higher nano-mound density. Their previous PAS studies of Zn vacancies in ZnO have identified

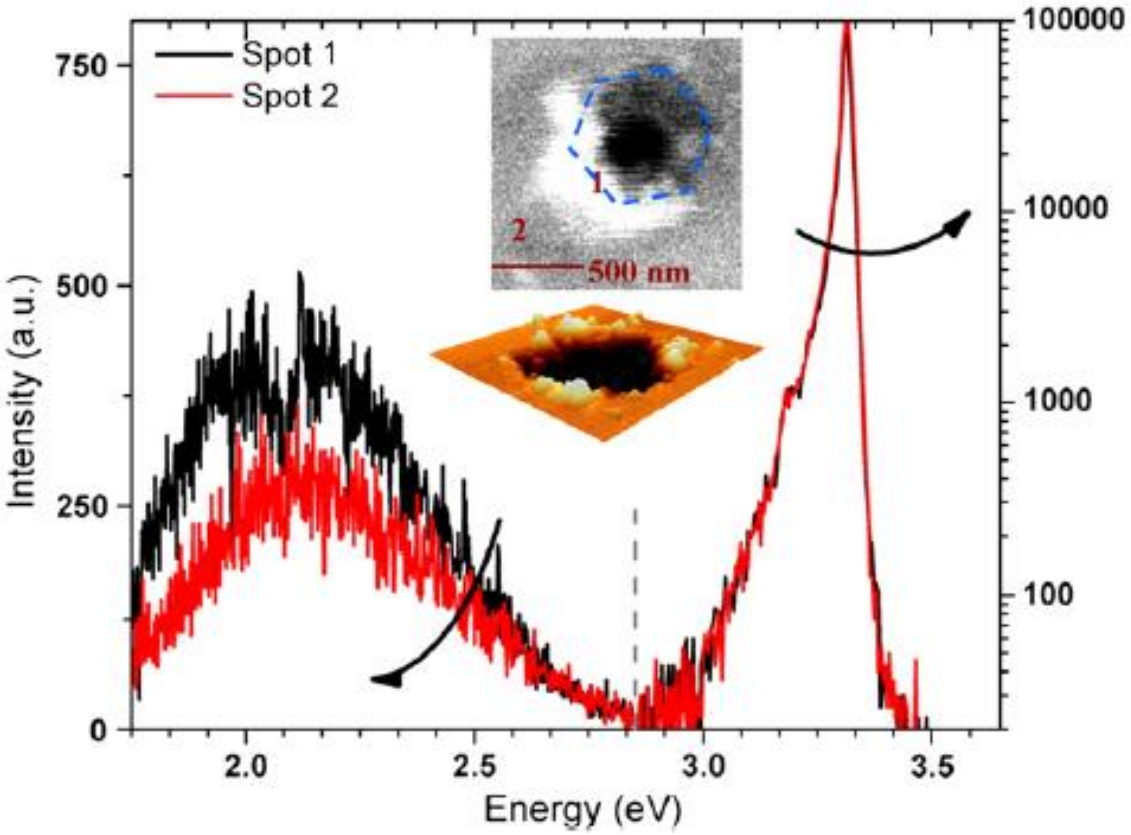

Figure 3.6 Near-surface DRCLS spectra (T=12 K) normalized to the NBE for E_B=3.3eV on a ZnO (0001) surface with nanomounds bordering a hexagonal pit. Zn vacancy emission at 2-2.1 eV increases dramatically at the outer edge of the nanomounds. [88]

a 1.7 eV optical transition with isolated Zn vacancy defects and a related 2.1 eV optical transition with Zn vacancy clusters. [89]

In our experiments, similar nano-pits and nano-mounds are observed after annealing pretreatment at sufficiently high temperature. The atomic structure is relevant to the electronic structure and subsequently catalytic behavior. As a result, the above appearance of new nanostructures would result in formation of new energy level on the surface. In order to understand the role of ZnO nanopits, it is of significant importance to learn the nature of ZnO diffusion. To approach a promising mechanism, it is necessary to calculate the defect formation energy of various ZnO species, which determines how

difficult it is for these species to diffuse. In a simple chemical formula, ZnO has only three types of defects: Zn vacancy, O vacancy, Zn-O dimer vacancy. Among these three possible defects, a lot of experimental and theoretical evidence has been found for Zn and O vacancy. Despite the huge amount of ZnO papers, very few of them are found to be related to the Zn-O dimer vacancy. Roman Kovacik *et al.* have employed the DFT calculation to exhibit that the Zn-O dimer vacancies could be the most favored atomic defects on the ZnO $(10\bar{1}0)$ surface, in both UHV experiments and catalytic reactions. [90] According to their calculations, a table with the formation energies of O, Zn and Zn-O dimer vacancies and how these formation energies change with the oxygen chemical potential is illustrated in Figure 3.7. The formation energy of Zn-O dimers amounts to only 1 eV, whereas 3.6 eV is required to form a separated Zn and O vacancy pair. That is because the Zn-O dimers are neutrally charged, leading to a much lower formation energy. The above theoretical work has predicted that Zn-O dimer vacancies should be the most abundant atomic defects and the most preferred diffusion species during surface reconstruction. In our following experimental work, the occurrence of Zn-O dimer diffusion is favored under high temperature pretreatments, especially in the oxidizing conditions. The diffusion of Zn-O dimers should be responsible for the formation of nanopits on the big terraces on the ZnO surface.

3.5 Experiments And Results

All the experiments are performed in an UHV chamber, including Cu deposition, scanning tunneling microscope (STM), EELS, low energy ion scattering spectroscopy (LEIS), and low-temperature ultraviolet photoelectron spectroscopy (UPS). The substrates are non-polar surface of ZnO $(10\bar{1}0)$ (MTI Corporation) and have been

Table 1: Formation energies [in eV] of O, Zn, and ZnO-dimer vacancies on the nonpolar ZnO(10$\bar{1}$0) surface.[a]

Unit cell	N_L	N_{at}	$E_v^O - \Delta\mu_O$	$E_v^{Zn} + \Delta\mu_O$	E_v^{ZnO}
(3×2)	4	48	2.87	0.62	1.49
	6	72	2.90	0.40	1.06
	8	96	2.91	0.45	0.97
	10	120	2.91	0.41	0.95
(4×2)	6	96	3.05	0.50	1.07
	8	128	3.05	0.53	0.97
	10	160	3.05	0.47	0.95
(5×3)	8	240	3.17	0.51	1.03

[a] As a function of the surface unit cell size ($n \times m$) and the slab thickness N_L, yielding N_{at} atoms in the supercell calculation.

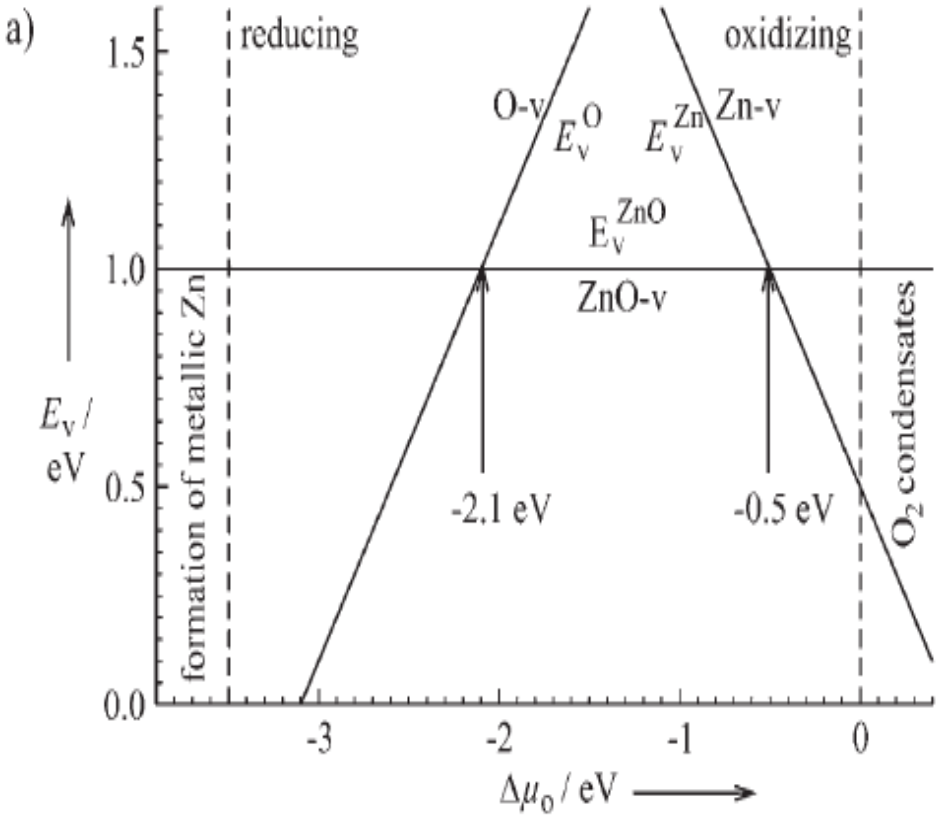

Figure 3.7 Formation energy of different atomic defects on the ZnO (10$\bar{1}$0) surface as a function of the oxygen chemical potential of a surrounding gas phase. [90]

prepared by repeating cycles of Neon-ion sputtering (1.5 kV, 30 min, 15 mA) and annealed to increasingly higher temperature, up to 650°C. Before all the proceeding experiments, surface order and cleanliness were monitored by low-energy electron diffraction (LEED), and Auger electron spectroscopy (AES) respectively.

Cu clusters are deposited with an E-beam evaporator at room temperature (RT). The coverage of Cu clusters is calibrated by counting the cluster size and density from STM images, which were acquired using an Omicron variable temperature UHV STM. The annealing temperature is around 450°C and lasts 15 minutes. The oxidation was prepared by annealing Cu on ZnO in O_2 for 15 minutes. The pressure of O_2 is around $1x10^{-7}$ Torr, and the annealing temperature is 450°C.

The UPS measurements were performed at the Center for Advanced Microstructures and Devices (CAMD) at Louisiana State University. The photon energy in all the experiments is 25 eV. The CO_2 adsorption of different samples has also been achieved by exposing it to a constant pressure of $1x10^{-7}$ Torr at low temperature (~90K) and the exposure of CO_2 is up to 6 Langmuir (L).

LEIS experiments were performed in He source with a fixed scattering angle of 110°. The He^+ ion current injected to the sample is up to 500 nA at 1500 eV, with spectral acquisition of 3 mins. HREELS was performed in an electron spectrometer manufactured by LK Technology. Primary electron beam energies in all the experiments are fixed at 30 eV and spectra were taken with energy resolution of 13 meV.

3.5.1 STM

As a low-index face, ZnO $(10\bar{1}0)$ is non-polar surface with the lowest cleavage energy, which could be an ideal model system for the surface chemistry experiments. [102] As

shown in Figure 3.8, a well-defined terrace structure is clearly evident on the smooth ZnO $(10\bar{1}0)$ surface, and very few defects are found on the surface.

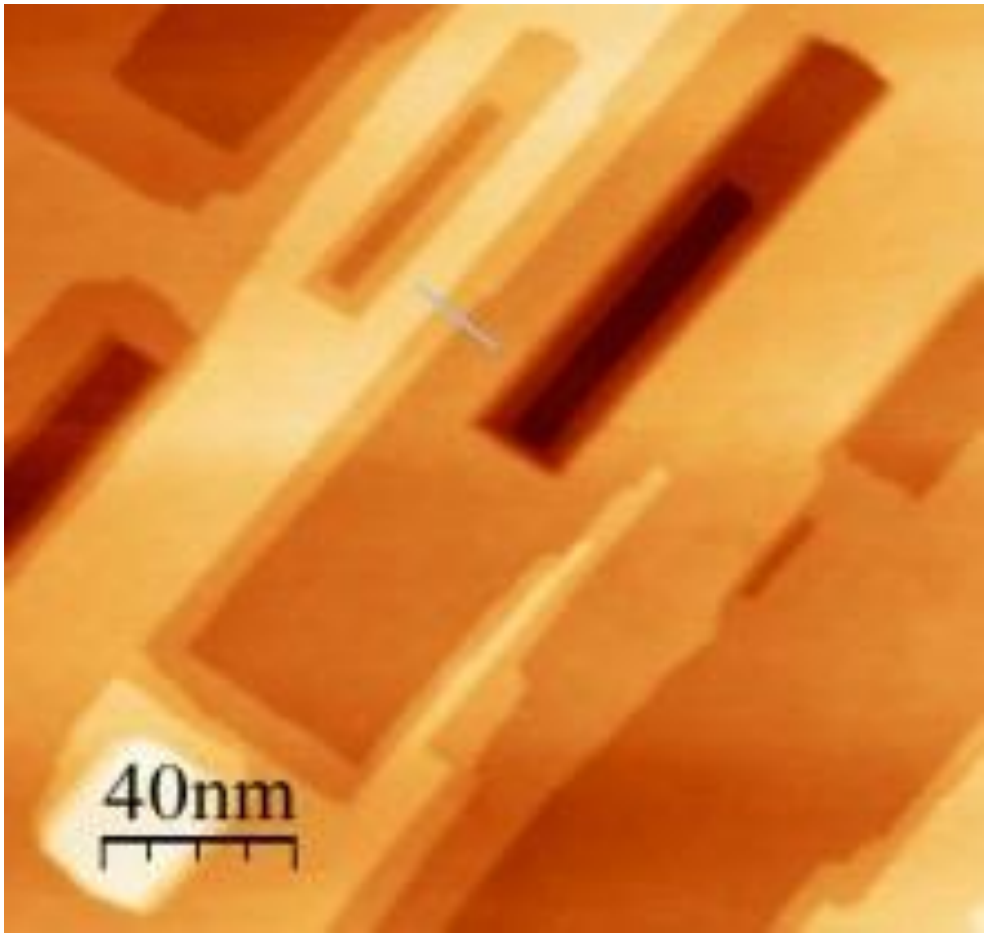

Figure 3.8 STM image of clean ZnO$(10\bar{1}0)$. (Thanks Fei Wang for taking STM data) [39]

As shown in Figure 3.9 A, after depositing 0.2 ML Cu in room temperature (RT), STM still reveals a well-defined terrace structure on the smooth ZnO $(10\bar{1}0)$ surface. The Cu clusters energetically favors nucleation at step edges and the mean size of these clusters is 5nm across and 0.5 to 1 nm high. Following the Volmer-Weber (VW) model, the 3D growth of Cu on ZnO surface shows a high tendency towards ripening even at low densities. It reflects a high (anisotropic) diffusion and a stronger Cu-Cu interaction compared to Cu-ZnO energetics. [92] After increasing the Cu coverage to 2ML, both the

steps and terraces are covered by Cu clusters with approximately the same size, but slightly higher, suggesting that higher Cu coverage primarily leads to higher cluster density. (Figure 3.9 B) Diffusion to the initial step sites has been suppressed and the nucleation of new Cu clusters occurs on the terraces, without appreciable Ostwald ripening. [93] In studies of Cu cluster distribution on polar ZnO(0001) surfaces, the spatial arrangement of Cu clusters on the terraces also reveals the absence of charging of the clusters.

The thermal energy is known to act as an additional destabilizing factor at sufficiently high temperature and control the surface reconstruction by the coalescence and ripening process. [94] It needs to notice that the visible differences are not noted until 350 °C. A 2 ML Cu/ZnO sample, deposited at RT and annealed to 450 °C, is shown in Figure 3.9 C. The clusters appear larger (around 10nm) and higher (1 to 1.5 nm), which is mainly caused by the coalescence of small clusters. An analysis of this image results in a ~23% nanocluster areal coverage. The slight oxidation of Cu clusters may also contribute to the larger cluster size, which we cannot exclude here. In addition to larger Cu clusters, STM also reveals the emergence of new "nano-pits" that are randomly distributed around Cu clusters. All the nano-pits are 0.3 nm deep, corresponding to the height of a "Zn-O" bilayer, which points to the partial removal of the ZnO layer. After exposing this surface to O_2 at the same elevated temperature ($1x10^{-7}$ torr O_2 for 15 mins at 450°C), the cluster number density has very slight change while the mean cluster size becomes even larger (around 12 nm) and higher (2.5 nm). (Figure 3.9 D) An analysis of this image results in a ~26% nanocluster areal coverage. This indicates that the cluster size has increased after

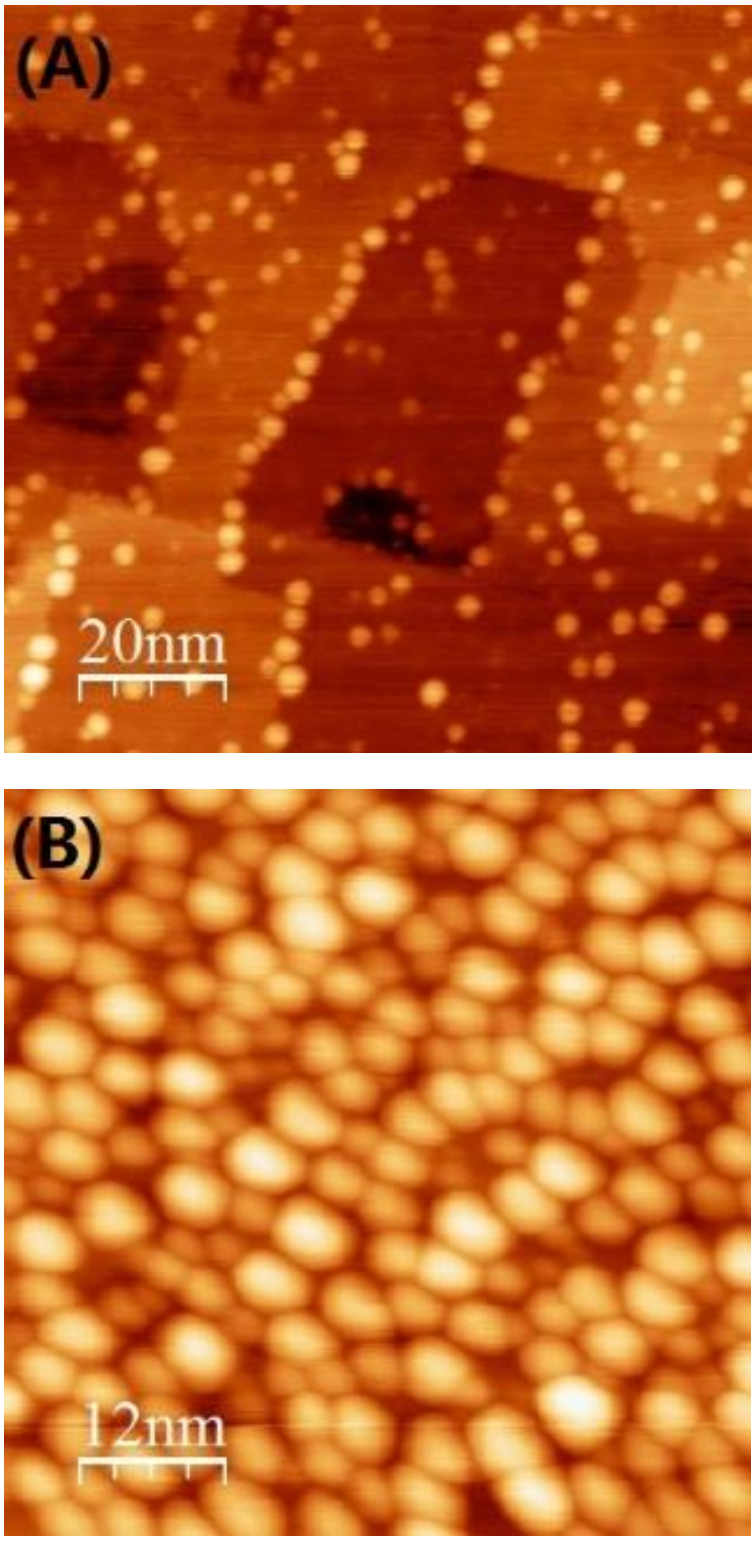

Figure 3.9 (A) Deposition of 0.2 ML Cu on ZnO ($10\bar{1}0$) in RT; (B) Deposition of 2 ML Cu on ZnO in RT; (C) 2ML Cu annealed at 450 ℃ for 15 min; (D) the 2ML Cu oxidized in $1x10^{-7}$ Torr O_2 at 450 ℃ for 15 min. (Thanks Fei Wang for taking STM data) [39]

(Figure 3.9 continued)

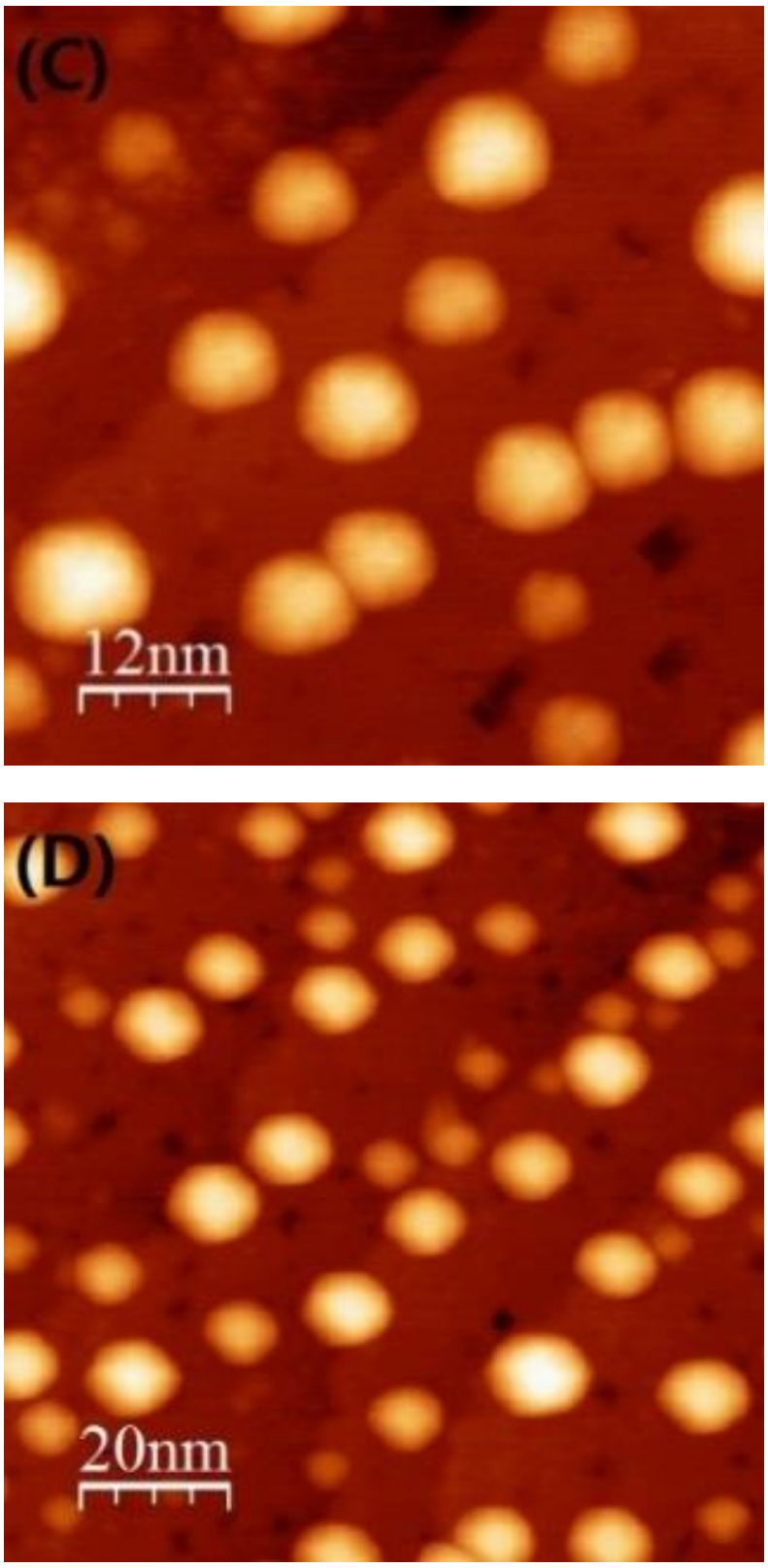

heating in oxygen. STM reveals that following this treatment, there is little change in the overall shape with a slight change in aspect ratios.

One might conclude that this may be due to simply a partial oxidation of the Cu but the LEIS and EELS data, below suggest that a more complex process is in place. These data indicate that the surface can no longer be characterized as merely Cu (or Cu_xO) clusters supported on the unperturbed ZnO($10\bar{1}0$) "support".

3.5.2 EELS

In general, the performance of catalyst is very sensitive to the chemical and physical structure of the surface. As a powerful surface-sensitive probe, EELS can play a key role in elucidating the vibrational and electronic structure of the surface. For electron losses in the 10 s to100 s of meV, one can observe vibrational excitations of the substrate as well as those of adsorbed species. Here we present data in the several eV energy-loss range which provides information on electronic excitations and interband transitions.

As shown in Figure 3.10, EELS reveals that the clean ZnO surface has wide band gap of 3.3 eV resulting from the interband transition from O 2p to the bottom of the conduction band. The Fuchs-Kliewer modes, due to the optical phonon losses of the ZnO, can just be seen at energies below 0.3 eV. Upon deposition of 2 ML of Cu at RT, a new loss peak at around 2.2 eV emerges within the ZnO band gap due to the 3*d*-interband transitions of metallic nanoclusters of Cu on the surface. This is consistent with the STM results presented above. Surprisingly though, after the Cu clusters are oxidized by annealing in O_2, the interband peak due to metallic Cu peak is totally attenuated and only the loss corresponding to ZnO remains at the surface. Furthermore, if one assumes that the Cu clusters are partially/totally oxidized, a loss feature due to the corresponding oxide

would be observed in EELS within the band gap. CuO shows an interband transition onset at 1.4 eV while Cu_2O exhibits this onset at 2.3 eV. What we observe in Figure 3.8 following oxidation is an interband transition onset consistent with the bandgap of ZnO.

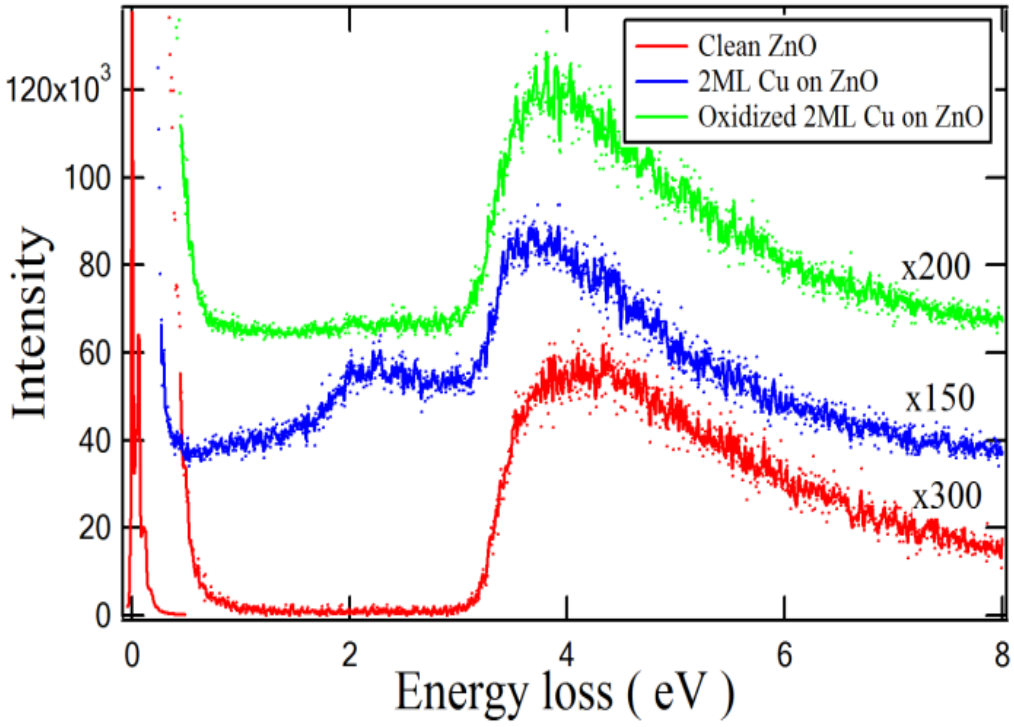

Figure 3.10 EELS: Optical spectra of clean ZnO, 2ML Cu on ZnO at RT, oxidized 2ML Cu on ZnO in O_2 $1x10^{-7}$ Torr at 450 ℃

EELS is a highly surface sensitive probe, and these data indicate the elimination of all the Cu related electronic losses upon annealing in oxygen. In the specular scattering geometry of this 30 eV electron beam, scattering is in the q=0 limit, and dipole scattering results in a sensitivity to only the top 1-2 ML of the surface. With the lack of Cu or Cu_xO-related losses a new model for the cluster structure is needed. The STM data, taken alone, indicates that the oxidative pretreatment merely increases the mean size of Cu clusters. With the lack of Cu spectral features on the surface, one potential hypothesis is that the

Cu clusters are encapsulated by ZnO, rather than Cu atoms simply diffusing into the selvage region of ZnO.

3.5.3 LEIS

In addition to EELS, low energy ion scattering spectroscopy (LEIS), a unique tool which yields atomic composition of the outer atomic layer, has been used to study the cluster surfaces. In the experimental arrangement chosen here, the scattering ratio of Zn to that of both Cu and Zn has been employed to extract information of the surface composition as function of annealing temperature. Because the mass of Cu and Zn are similar, a fitting procedure has been used to extract the relative composition at the surface for different annealing treatments of 2 ML Cu/ZnO($10\bar{1}0$). The results of fitting the LEIS data for the systems described above are shown in Figure 3.11 and can be directly correlated with the STM results. For example, at temperatures below 200°C, both STM

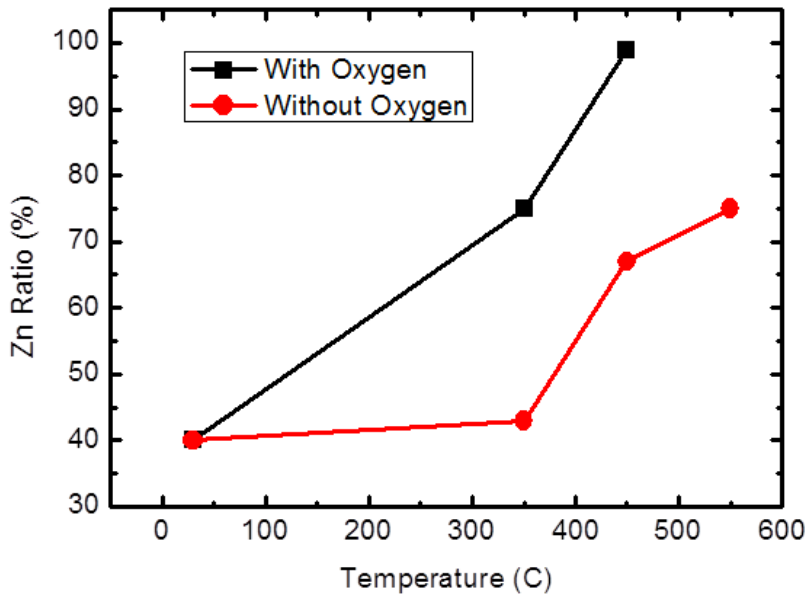

Figure 3.11 LEIS: the Zn ratio (in term of Zn/(Zn+Cu)) of 2ML Cu on ZnO with increasing temperature with/without oxygen flow

and LEIS indicated that the surface is covered with an areal density of approximately 60% Cu nanoclusters with 40% of the ZnO remaining uncovered. However as indicated in Figure 3.9, the Zn ratio increases with the annealing temperature in both vacuum and in oxygen ($1x10^{-7}$ Torr O_2). In the annealing pretreatment without oxygen, the sharp increase at 450 °C is mainly caused by the coalescence of small clusters, as seen in the STM; the Zn ratio at that point is at 67%. The highest ratio in the 2 ML vacuum annealed sample increases to 73% at 550 °C and compares reasonably well with STM areal density of 77% coverage.

In contrast, LEIS results for samples annealed in oxygen are markedly different. Figure 3.9 shows that annealing in oxygen, even at $1x10^{-7}$ Torr, greatly enhances the Zn surface composition ratio at the same temperature. Indeed, the oxidative pretreatment at 450 °C enhances the Zn surface composition ratio to almost 100%, which is in agreement with EELS results described above.

To investigate the effect of interfacial interaction, the annealed sample is directly exposed to oxygen while holding the temperature at 450 °C. The Zn ratio is also found to increase from 67% to 97%, indicating the encapsulation process is enhanced in oxygen despite the initial vacuum annealing treatment.

Based on the above discussion, the surface structure of Cu/ZnO system under various pretreatment is pictured in Figure 3.12. The Cu clusters are partially encapsulated in the annealed sample, while they are fully encapsulated in the oxidized sample. It is important to notice that the high temperature pretreatment also induces the interface interaction in both samples. As known, the outer surface determines many processes such as adhesion, catalysis. For example, the ultra-thin encapsulation layer is always part of the definition

of SMSI. So it is necessary to study the surface chemistry of the above samples, in order to understand why the encapsulation changes the adsorption behavior.

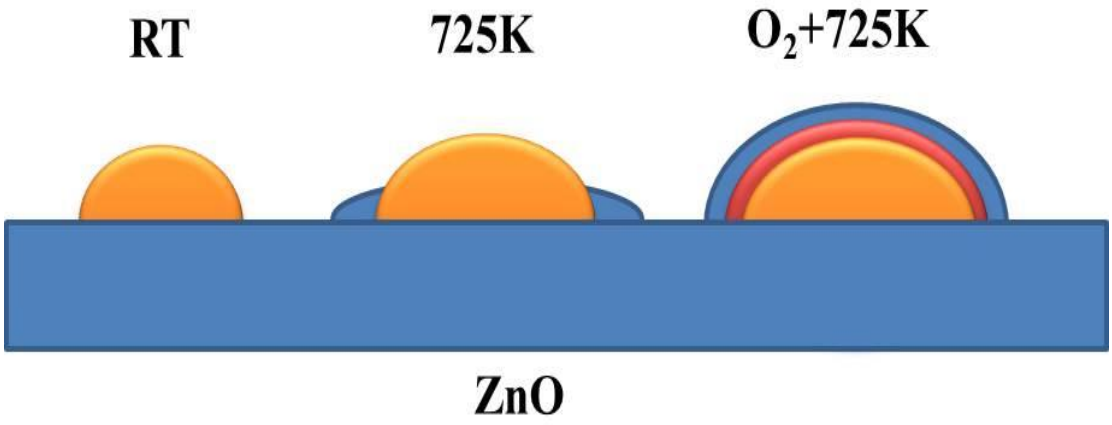

Figure 3.12 Schematic illustration of Cu/ZnO system under various pretreatments, in which the blue represents ZnO, yellow Cu, and the red possible CuO_x. (450 °C is around 725K)

3.5.4 UPS

UPS is an effective technique in studying the valence energy levels and chemical bonding, and it is employed here to gain further insight into the electronic structure of the above samples. Different from the other UPS data (25 eV), photon energy used here is 21 eV. Clean ZnO shows three peaks in Figure 3.13: 3.7 eV, 4.8 eV and 10.3 eV, which are ascribed to O 2p and Zn 3d respectively. After annealing in CO at high temperature, all the peaks have red shifts from CO reacted with ZnO. It is evident that the reduced ZnO species have a binding energy, which could be ascribed to the higher density of O vacancies after the CO reduction.

Different photon energies will bring changes to the position and shape of peaks, and that is why the shape of Zn and O peaks at 25 eV is deviating from that at 21 eV. As seen

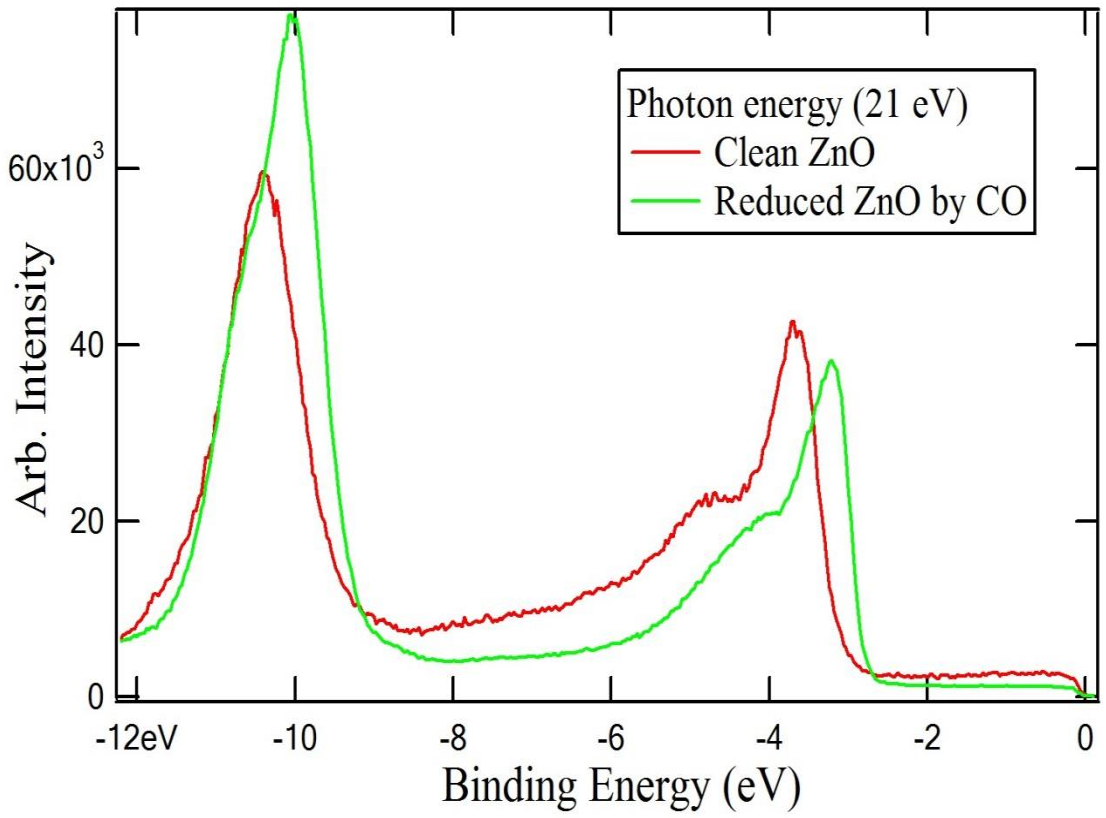

Figure 3.13 Clean ZnO reduced by annealing in CO

in Figure 3.14(a), the spectrum from clean ZnO is dominated by three peaks due to valence electronic states: Zn 3*d* (10.6 eV binding energy (BE)) and a pair of O 2*p* states (3.8 eV, 4.7 eV BE). Despite the fact that stoichiometric ZnO should be an insulator, at the surface we observe a very slight uniform density of states in the bandgap region (0-3 eV). These states exhibit a Fermi edge that allows us to observe potential charging which would cause us to measure an apparent shift in E_F, and allows us to isolate band-bending effects from charging. We find that for all of the treatments and spectra reported here, the Fermi edges align indicating there is no substrate charging for our samples under these

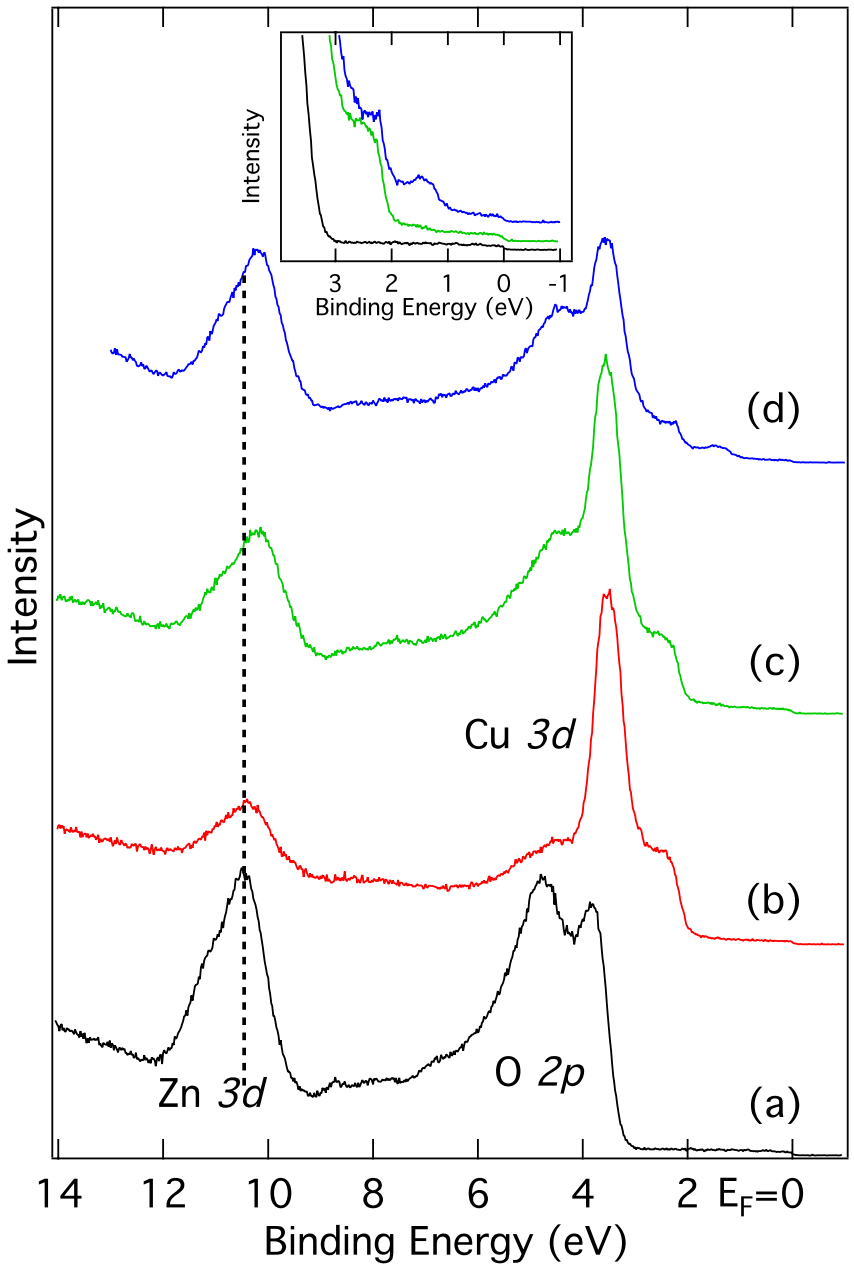

Figure 3.14 Photoemission spectra from (a) clean ZnO($10\bar{1}0$); (b) 3 ML Cu/ZnO($10\bar{1}0$) at RT (c) 3 ML Cu/ZnO($10\bar{1}0$) annealed to 450°C for 15 minutes; (d) 3 ML Cu/ZnO($10\bar{1}0$) oxidized in $1x10^{-7}$ Torr O_2 at 450°C for 15 minutes. The inset compares the bare ZnO (a) with the annealed and oxidized spectra, (c) and (d), in the region near E_F. The 1.4 eV feature, absent in ZnO($10\bar{1}0$)and clear in the oxidized spectrum is already visible as a shoulder in the annealed spectrum. The dashed line is a guide to the eye to highlight band-bending.

treatments. One caveat that needs to be made is that surface inhomogeneities such as patches may occur, where the band-bending and insulating/conducting natures may differ, giving a distribution in their effects.

Upon deposition of 3 ML Cu at RT, Figure 3.14(b), there are no measured shifts to the Zn and O related states, however the spectrum is dominated by the appearance of Cu 3*d* peaks at 2.4 eV and 3.5 eV BE, characteristic of metallic Cu, and consistent with previous XPS results indicate metallic Cu at this coverage range[30]. Because of the absence of peak shifts due to band bending, the UPS data indicates that the interaction between ZnO and Cu clusters is very weak, which is consistent with both previous theoretical calculations[33,30], and the above STM and LEIS results, wherein ~ 5 × 1 nm Cu clusters cover approximately 60% of the surface at 2 ML.

As seen in Figure 3.14(c), annealing 3 ML Cu/ZnO($10\bar{1}0$) to 450°C results in a FWHM of the Zn 3d peak that is 0.3 eV wider than the clean ZnO. Comparison of the lineshapes for these two surfaces suggests that an additional shoulder appears on the high binding energy side of the 3d peak.

As shown in Figure 3.14(d), for oxidized 3ML Cu/ZnO($10\bar{1}0$), a new feature appears at 1.4 eV while the upper edge of the Cu 3d remains unchanged at 2.1 eV and the primary Cu 3d peak is located at 3.6 eV as in the other samples. The peak at 1.4 eV seen as a shoulder in the annealed spectrum and is clear in the oxidized spectrum, suggesting the formation of partly covalent Cu-O bonds. As seen in the inset of Figure 3.12, under the oxidative conditions at higher temperature, the Cu_xO peak becomes distinct and the intensity of the metallic Cu bands at 3.5 eV decrease, partially due to oxidation and partially due to encapsulation. As an aside, it is difficult to clearly identify Cu (I) from Cu

(0) using UPS, however a previous XPS/AES study showed that Cu (I) is the highest component in this oxidized sample. [96] Although a detailed structure of these clusters is still under study, it is important to note that the 3d Cu states are clearly evident by UPS, even after the encapsulation. Although the presence of surface Cu is absent in both EELS and LEIS spectra, the observation of Cu states with UPS, having a probing depth of ~ 1 nm implies that despite encapsulation of the Cu nanoclusters by ZnO, this coating is probably only one or two layers thick.

In Figure 3.15, we show UPS studies of CO_2 adsorption on these surfaces. In CO_2 adsorption, the chemical bonds of CO_2 to the surface are determined by the atomic and electronic structure of the catalyst surfaces. As a powerful tool to study adsorbed species, UPS is also employed to investigate the adsorbed CO_2 to probe the surface chemistry property of Cu on ZnO catalysts. On the clean ZnO surface, Figure 3.15 (a) shows that all the peaks have the same energy shift (0.15 eV), due to the CO_2 induced downward band bending. In order to find the effect of Cu clean ZnO surface, the CO_2 adsorption ceases upon 1L and it shifts ZnO peaks toward deposition, two samples are prepared under room temperature: 0.2 ML and 3 ML Cu on ZnO. On the surface of both samples, no CO_2 adsorption takes place, suggesting that the CO_2 adsorption sites on ZnO should be buried via the deposition of Cu. (Figure 3.15 (b), (c)) The nature of this deviation might arise from the change of the impact energy and adsorption probability of CO_2 after the deposition of Cu. [95]

In annealed sample, the interaction between Cu clusters and ZnO has been attributed to both geometric and electronic effects. By increasing the CO_2 dosage, a new weak CO_2 adsorption occurs, while Zn and O peaks shift higher and are accompanied with a

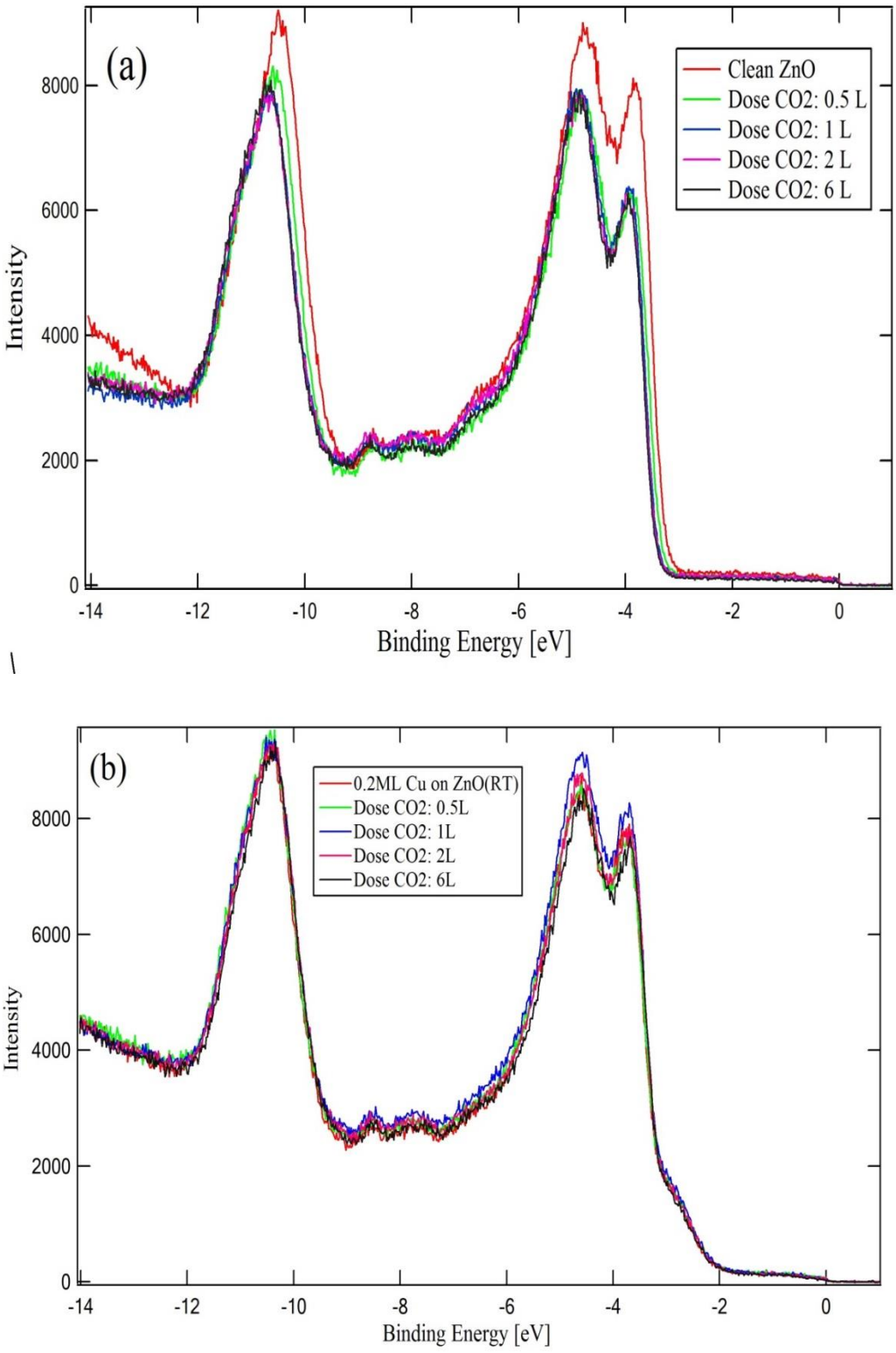

Figure 3.15 UPS: CO_2 adsorption on different samples (a) Clean ZnO; (b) 0.2ML Cu on ZnO; (c) 3ML Cu on ZnO; (d) Annealed 3ML Cu on ZnO at 450 ℃; (e) Oxidized 3ML Cu on ZnO at 450 ℃

(Figure 3.15 continued)

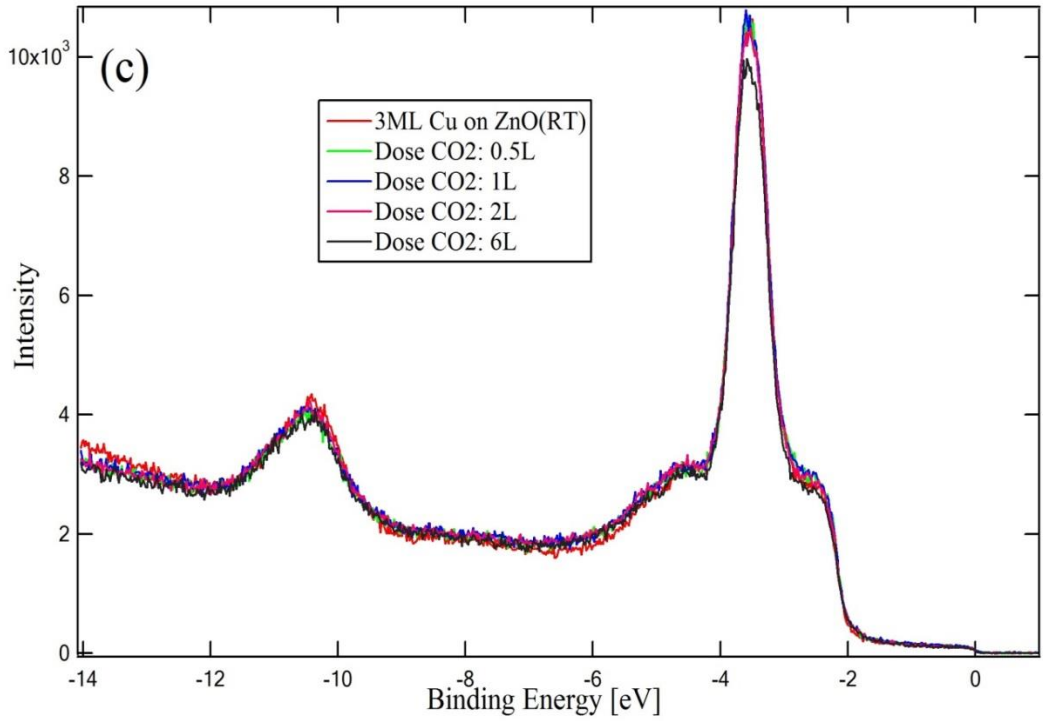

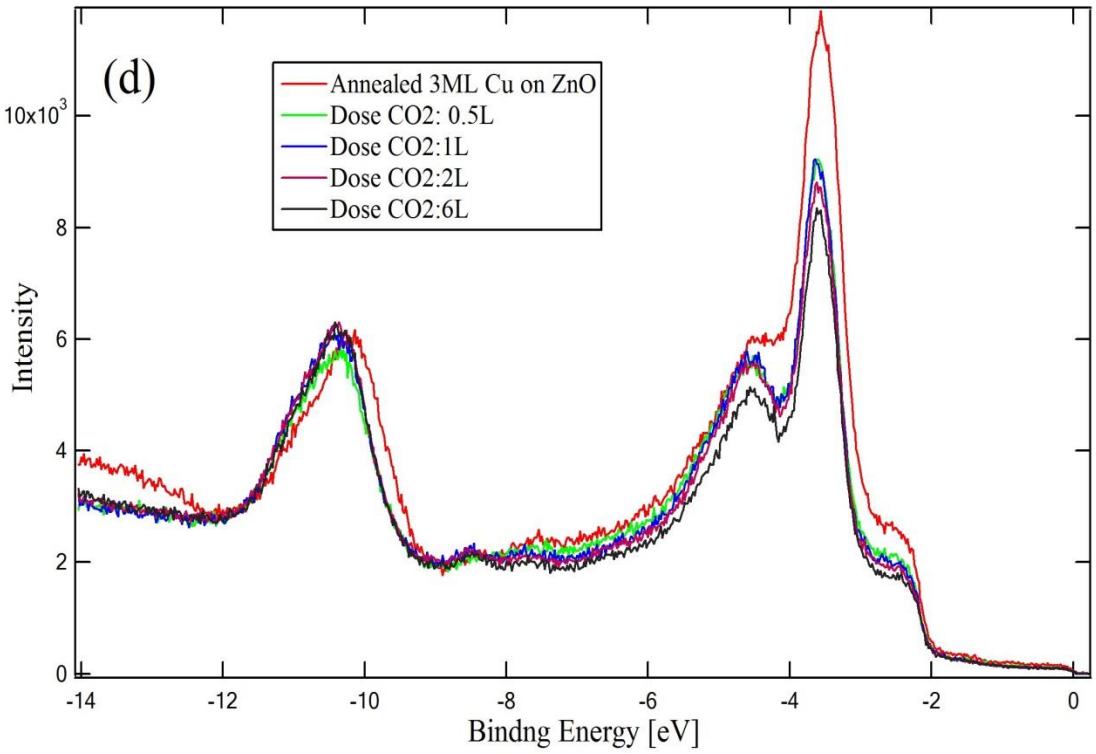

(Figure 3.15 continued)

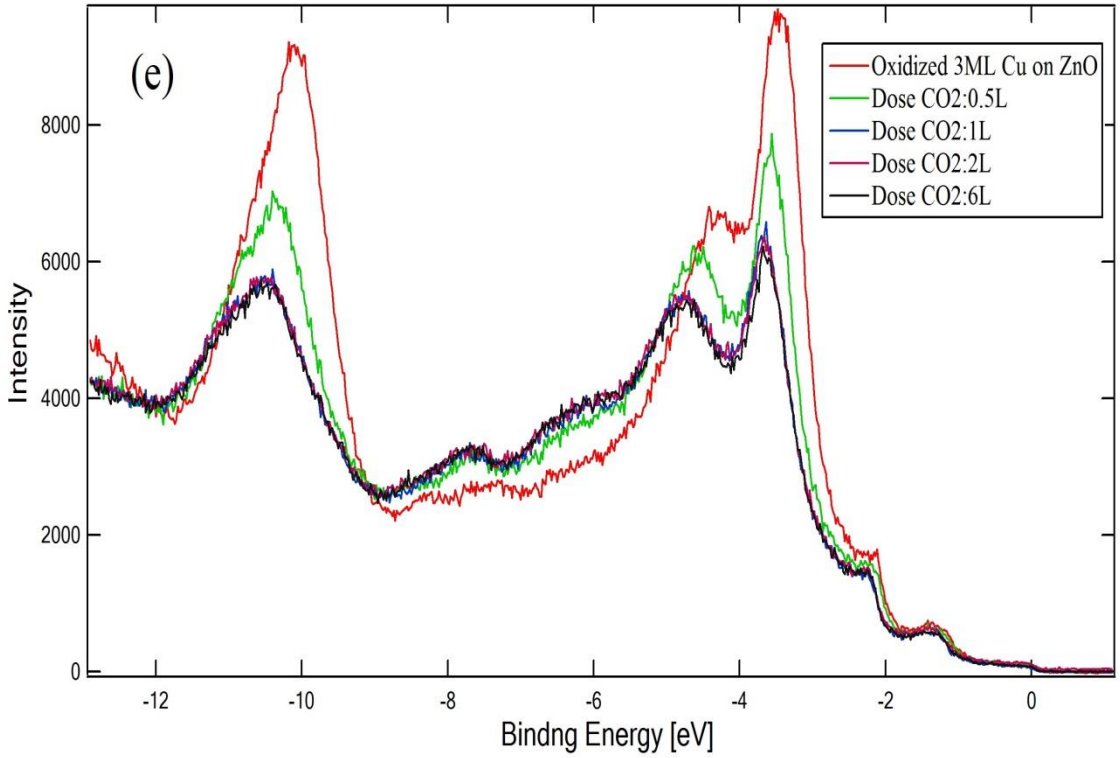

decrease in intensity. (Figure 3.15 (d)) In addition, Zn 3d peak (0.26 eV) shifts more than O 2p peak (0.15 eV), indicating the formation of covalent bond of carbonate on the surface. We also note that the Cu related peaks have no change at all, which means the Cu species are not the favorite adsorption sites for CO_2. The encapsulation of the thin oxide film on metal catalyst as well as the SMSI found in particular catalyst system usually show reduced catalyst activity, since the adsorption of gas molecules are drastically attenuated on the new formed thin oxide films. [100] However, the support role of ZnO has proved to highly improve the selectivity and activity of Cu catalysts in methanol synthesis reactions. [95] As a result, we want to investigate the CO_2 adsorption behavior to understand the important support role of ZnO to Cu catalysts. In Figure 3.15 (e), it displays a strong adsorption of CO_2 on 3ML Cu on ZnO pretreated in oxidative

environment. As more CO_2 is dosed, Zn and O peaks keep shifting higher with a decreasing intensity. The decreased intensity is due to the higher CO_2 coverage caused by the gradual encapsulation of Cu the nano-clusters, while the blue-shift of Zn and O peak indicates the electron transfer from the surface to the adsorbed CO_2. In addition, two new broad peaks are found to range from 5 eV to 9 eV, which is ascribed to carbonate. Similar to the annealed sample, Cu peaks do not show any change, due to the encapsulation. So it can be deduced that abundant new adsorption sites on the ultra-thin ZnO film are created for CO_2 and the stronger chemical bonds between CO_2 and the surface is caused by the oxidative pretreatment.

Difference spectra produced by subtracting the oxidized 3ML Cu/ZnO($10\bar{1}0$) spectrum from that after CO_2 exposure are unreliable and show spurious features due the fact that some features in the spectrum clearly show band-bending effects while others, such as the upper edge of the Cu bands and the 1.4 eV feature do not.

3.5.5 CO Oxidation

After investigating the chemical adsorption of CO_2, CO oxidation was completed in a brash reactor. As shown in Figure 3.16, the reaction rate has a close relation with the CO_2 adsorption of the above prepared samples. The 2ML Cu on ZnO (RT) has no CO_2 adsorption, while the corresponding CO_2 formation rate is very low. The strongest CO_2 adsorption was found on 2 ML Cu on ZnO sample (oxidized), which also has the highest CO_2 formation rate. The reaction rate of the active catalysts drops fast, which should be ascribed to the deactivation or the loss of reactants. To testify the above assumptions, we tried to perform the CO oxidation at different pressures without moving sample out of the chamber, in order to avoid the influence of formed CO_2. These two oxidized samples still

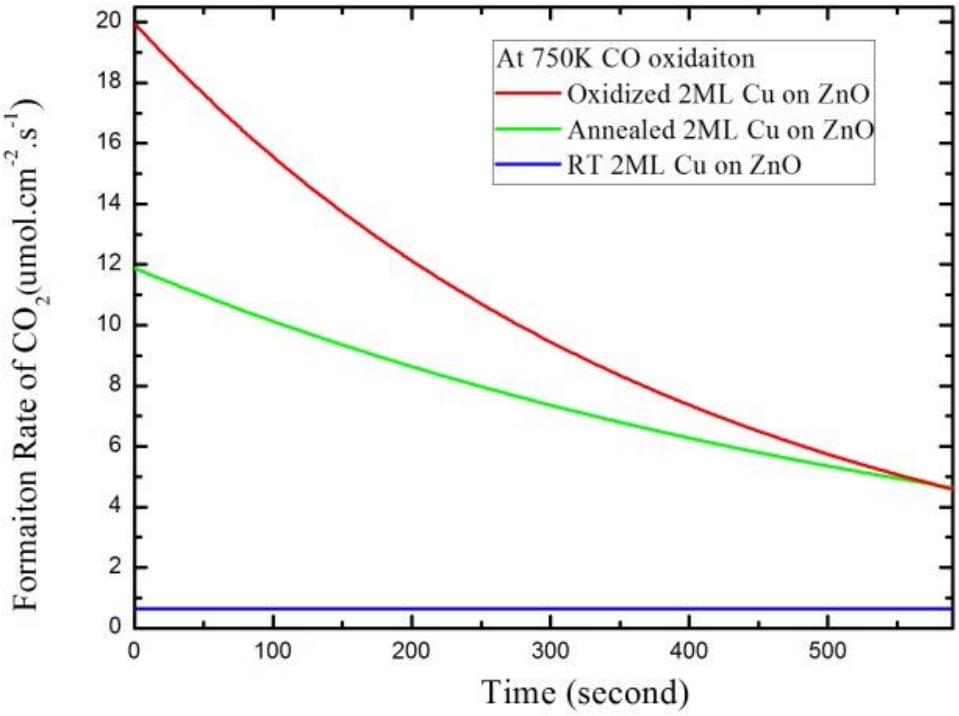

Figure 3.16 CO_2 formation rate on different prepared samples at a mixture of CO and O_2 (CO: O_2=2:1)

show a higher formation rate of CO_2 under high pressures in Figure 3.17, even after running in low pressures first. It is evident that the initial formation rate of both oxidized samples has a linear relation with the pressure, indicative of the high thermal stability of the above samples. Therefore the decreasing reaction rate is likely the consequence of the loss of reactants, instead of deactivation of the above catalysts. In actual gas-phase catalytic reactions, the reaction rate depends on various factors, especially the partial pressure of reactions. That is because the probability of reactants bond to the active sites is ascribed to the partial pressure of reactants. The cause for the linear relation is the ultra-high TOF of the active sites, where the reaction rate is determined by the probability bond to the active sites. The significant importance of the high thermal-stability

demonstrates that the encapsulation morphology of the above samples could be preserved during CO oxidation.

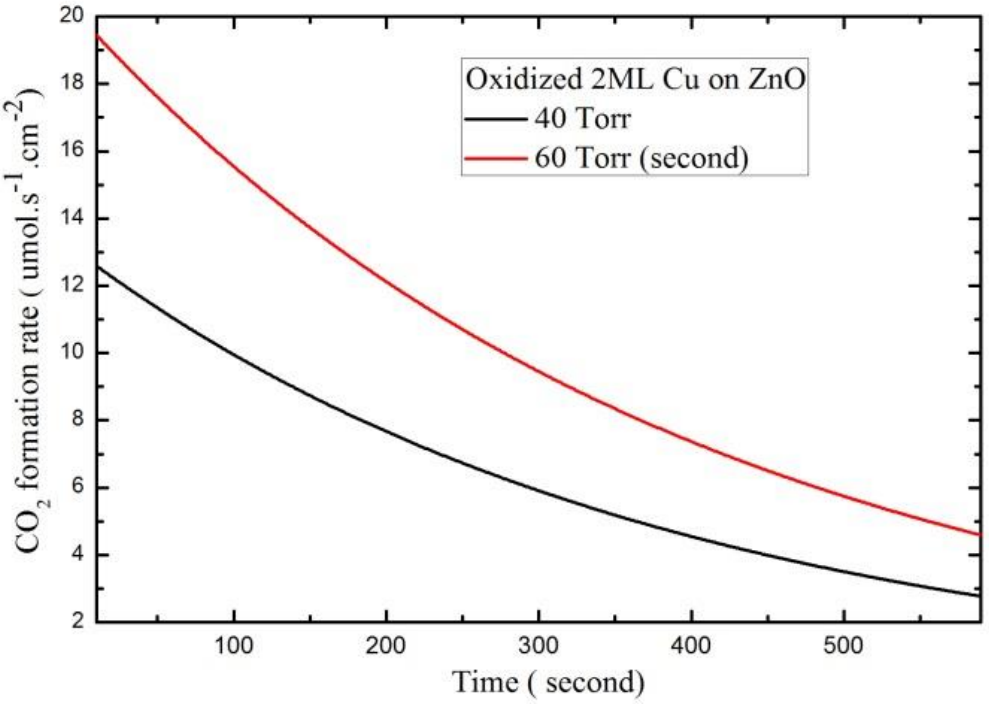

Figure 3.17 CO_2 formation rate at different pressure with a mixture of CO and O_2 (CO: O_2=2:1) on the same prepared sample. (Here the chamber is pumped down to UHV and filled with the mixed gas and then the same sample holds on to CO oxidation)

3.6 Discussion

As shown above, the experimental conditions determine the surface structure, surface composition and oxidation state of the catalysts, which play a decisive role on the surface chemistry of the catalysts. All these factors have led to the change of adsorption behaviors, and subsequently the reactivity of the system. Consequently, we try to figure out the internal connections in the following discussions.

The initial deposition of Cu results in metallic clusters that preferentially nucleate on step edges perpendicular to the $(1\bar{2}10)$ direction but with increasing Cu-coverage

approximately above 0.5 ML they fill the terraces as well, as has been reported previously.

As known, the classical SMSI always have the following characteristics: (a) response to high temperature pretreatment; (b) encapsulation of metal nanoparticles by the support; (c) the change of adsorption capacity and catalytic reactivity; (d) electron transfer in the interface. [97, 16, 99] In our case, the electron transfer in the interface is induced by the high temperature pretreatment, corresponding to the shift of Zn and O peaks in UPS. The annealing pretreatment makes the Fermi level of ZnO lower than Cu clusters, which requires the electron transfer from the Cu clusters to the support, in order to attain a Fermi-level equilibration at the interface. The encapsulation of Cu clusters by ZnO is induced by the oxidative pretreatment, which has resulted in a strong adsorption of CO_2. Here it is apparent that the strong interaction between Cu and ZnO should be denoted as SMSI, which brings different properties to both Cu clusters and ZnO substrate. For instance, this SMSI has affected the oxidation states of Cu by forbidding the further oxidation into Cu (II).

The active sites on ZnO supported Cu catalyst are always debatable and Cu/ZnO interface has been considered to be the active sites. [95] In our experiment, an enhanced adsorption capacity of CO_2 is observed after ZnO encapsulating the Cu nanoclusters and the interfacial SMSI effect is believed to have a great influence on the chemical bonds of CO_2 to the surface. The encapsulation behavior is driven by the charge redistribution and mass transfer. Therefore, it is of great importance to identify the adsorption sites of CO_2, which helps to learn the nature of CO_2 reduction into methanol.

First, no adsorption of CO_2 could be found on Cu on ZnO (deposited at RT). Moreover, the further high temperature pretreatment has reconstructed the surface, on which the new CO_2 adsorption sites are created. In the annealed sample, only the perimeters of Cu clusters are buried by ZnO, whereas Cu clusters are fully encapsulated in the oxidized sample. Compared to the annealed sample, the further oxidative pretreatment has greatly enhanced the CO_2 adsorption capacity, and the CO_2 could only be adsorbed at ZnO sites. Therefore, it is possible to conclude that CO_2 adsorption sites should locate at the ultra-thin ZnO films influenced by the interface, for instance the encapsulation layer and the perimeters of Cu clusters.

Apart from the adsorption sites, the adsorption energy also plays a decisive role on the pathways and reactivity of catalytic reaction. These chemical bonds of CO_2 to the surface on the oxidized sample are much stronger than those to the bulk ZnO or CuO_x (x=0, 0.5, 1), which suggests that the combined system exhibits better adsorption ability than the sum of the individual components. Naturally, it is evident that the structure of ultrathin ZnO films is governed by the Cu clusters underneath, in order to compensate the growth-induced stress. And these ultra-thin films become negatively charged by the interfacial charge redistribution. According to the charge-mediated binding mechanism, these unique ultrathin films would result in stronger chemical bonds with the adsorbed CO_2. Therefore, the substantial charge towards CO_2 not only enhances the chemical bonds between the adsorbates and the ultrathin films, but also modifies the chemical and physical properties of the ZnO ultrathin films.

The above results reveal that the unusual reactivity of the ultra-thin ZnO films is intimately relevant to the formation of ZnO encapsulation layers, especially in oxygen-

rich environment. As an unknown nano-structure with only one to two layers thick, these encapsulation layers could largely maximize degree the surface area of interface between metal clusters and the oxide support in three dimensions. These ultra-thin ZnO films present the strong adsorption of CO_2 favored in low substrate temperature, and the SMSI has strong effects on the chemical bonds of CO_2 to the surface. The enhancement of such chemical bonds is helpful to break the C=O bond of CO_2 and thus increase the probability of CO_2 hydrogenation. As a result, the above improvement is important for enhancing the catalytic activity, even at low CO_2/CO concentrations and subsequently the performance of methanol synthesis. Our CO oxidation experiments under realistic conditions verify the enhancement of catalytic activity and stability, which could be ascribed to the formation of SMSI, including the encapsulation of Cu clusters by ZnO support. In contrast to the previous reports, the oxidized sample possesses the highest reactivity of CO oxidation, mainly caused by the simple oxidation. The CO oxidation result is in a very good agreement with the CO_2 adsorption experiments, suggesting the Cu clusters could not be responsible for the above catalytic performance. The reaction rate of these special ZnO thin films remains stable through the oxidation even at high substrate temperature, which stands for the high-thermal stability of this thin film catalyst. The dissociation of oxygen molecules into O atoms could be dramatically facile at these ZnO thin films, since they are negatively charged. Moreover, the ultra-thin ZnO films as well as the SMSI states in the interface could stabilize the combined nano-structures against sintering through the core-shell configuration. The mechanism of CO oxidation would be discussed in Au on ZnO chapter.

3.7 Summary

The Cu growth on ZnO surface is in a manner of Volmer-Weber (VW) model, and therefore Cu clusters are found to locate at the step edges in low coverage. After depositing more Cu to the ZnO substrate, Cu clusters start to appear at the terraces with a similar size. A large size of these clusters could only be formed by high temperature pretreatments, mainly caused by the ripening and coalescence process. The introduction of O_2 at high temperature results in Cu clusters with larger size, which could be ascribed to Cu oxidation and ZnO encapsulation. In all these high temperature samples, the same charge transfer is found to occur between the Cu clusters and ZnO substrate, which indicates the neutrally charged ZnO dimers should be responsible for the encapsulation. Therefore, the ZnO dimer diffusion to the surface of Cu clusters may be the cause of Cu-ZnO synergy effect on the industrial catalysts. As proposed in other heterogeneous catalysts, SMSI based on the encapsulation and charge transfer plays a significant role in modifying atomic and electronic structure, and therefore results in unusual chemisorption and catalytic behaviors. Here it should be noticed that the substrate temperature plays a decisive role on the strength of SMSI effect, and the addtion of oxygen could enhance this primary effect, however the role of oxygen remains poorly understood.

This oxidation induced SMSI contributes to the strong CO_2 chemisorption and CO oxidation on ZnO thin films. The adsorption behavior here is different from the classical TiO_2 supported SMSI cases, in which the suppression of CO or H_2 adsorption is observed. The SMSI effect is responsible for the enhancement of stability and reactivity of ZnO thin films with hemisphere. The above model catalyst studies play a key role in bridging the existing gap between surface science and real catalysts. The remarkable

improvement of reactivity observed for the semi-core-shell structure points to a direct connection between ZnO thin films and catalytic performance, including the altered chemisorption behavior. Based on the above findings, the traditional Cu based mechanism could not explain the exceptional reactivity found in our experiments. These ZnO thin films have important advantages: (1) low coordinated thin films, which enables the rearrangement of chemical bonds and therefore reduces the activation barrier; (2) negatively charged surface is energetically favored for dissociation of oxygen molecules, which is the most difficult step in CO oxidation experiments. That is why the whole CO oxidation process could be completed on these ZnO thin films without CO diffusion to the interface. Therefore, new routes become available to redesign the adsorption behavior and certainly the related catalytic performance of ZnO supported Cu systems. The internal connection between the interface and the catalytic performance may be helpful to reconstruct the mechanism of methanol synthesis. It definitely opens up new pathways to redesign this important industrial catalyst with the modified atomic and electronic structure by changing the preparation conditions.

Chapter 4: Au on ZnO

4.1 Introduction

Au nanoparticles dispersed on metal oxide surface are found to be active for hydrogentation of CO and CO_2 and scientists have paid enormous attentions to its important role of CO_2 reduction into fuel cell through the photoactivations. [103] In order to optimize the Au based heterogeneous catalyst, it is important to understand which factors determine the overall catalytic performance. In general, the catalytic performance of supported Au particles is determined by three key features: the Au particle size, the type of support, and the interface between Au particles and the support. Among these three factors, the interaction between the Au nanoparticles and the support has a significant influence on the reactivity and selectivity of Au supported heterogeneous catalysts. [106] Among these metal oxide supports, ZnO has caused widespread interest in its potential application in methanol industry. The previous studies have shown that Au on ZnO shows exceptional catalytic performance of methanol synthesis and Water-Gas shift reaction, even similar to that of the classical Cu on ZnO catalyst. [103, 104, 105]

In order to improve the chemical properties of Au based catalyst, it needs to understand the electronic structure and chemical composition of these active sites, which is the first step to construct the mechansim of catalytic reactions. Three mechanism have been proposed for carbon monoxide oxidation on Au on ZnO samples: (1) the reaction occurs on the support, where carbon monoxide molecules and oxygen species would migrate into the active sites; (2) the reaction takes place on metallic gold particles, which could dissociate oxygen molecules into oxygen atoms; (3) the reaction could happen at the edges of gold particles, where the sites on the support and sites on the metal could be

influenced by the metal-oxide interaction. [110, 111, 112] Among these three assumptions, most of research work has suggested that the active sites should located at the interface between the Au nanoparticles and the support, particularly at the perimeter line of the nanoparticles. [105, 107, 109] However, a few new experiments have demonstrated the decisive role of oxygen vacancies on ZnO, which could be the active sites for methanol synthesis. According to Forst's work, the reducibility of the oxide could be increased by increasing the density of oxygen vacancies and the improvement of ZnO reducibility could greatly enhance the catalytic performance of CO oxidation through the O vacancies on ZnO. [117]

In our studies, Au on ZnO catalyst has a similar reactivity of CO oxidation to the Cu on ZnO catalyst, which provides a strong indication that the "support role" of ZnO should be the main cause for the catalytic reactions, such as methanol synthesis, water-gas shift reaction. In this chapter, we will present how the activity and selectivity of Au on ZnO samples is interlinked with the formation of reduced ZnO thin films, which could be tuned by controlling the experimental conditions.

4.2 Experiments And Results

All the experimental work was performed in UHV chambers and the base pressure is less than $2x10^{-10}$ Torr. ZnO single crystals were cleaned by several cycles of Ne^+ sputtering and annealing (650 ℃, 30 min). The surface was investigated by Auger spectra and LEED. This cleaning process was not completed until a clear LEED pattern was observed. After obtaining a clean surface, Au was deposited at room temperature, using a thermal evaporator with 99.999% Au source. The deposition rate was calibrated from the STM images and the coverage of Au changed with the time. All the CO oxidation

experiments are completed in a brash reactor and the mixture of CO and O_2 in a ratio of 2:1is filled into the chamber before raising the reaction temperature.

4.2.1 STM

As a power tool, STM here is applied to investigate the atomic structure of the prepared model catalyst, which enables us to observe the growth of metal nanoparticles on single crystal surface. Figure 4.1 (a) shows the STM image of 0.05 ML Au deposited on ZnO $(10\bar{1}0)$ surface at room temperature. The small Au layers are randomly dispersed on the whole surface, including step edges and big terraces. It is important to note that the step edges are energetically favored adsorption sites for Cu at low coverage. The mean size of these Au layers is found to be 3nm across and 0.3 nm high, which equals to only one layer thickness of Au and provides a strong indication of 2D growth of Au on ZnO $(10\bar{1}0)$ at relatively low coverage. The different growth model for Au on ZnO suggests that the interaction between Au and ZnO is stronger than that between Au atoms. This explains why the diffusion of Au atoms is forbidden, leading to the formation of 2D Au islands on the surface.

As shown in Figure 4.1 (b), a much higher density of Au islands is observed for 0.4 ML Au on ZnO. The average height of Au islands at this coverage is slightly less than 0.7 nm (~2 ML Au thickness), which suggests both 2D layers and 3D clusters exist on the surface. Following the classical Stranski-Krastanov growth model, the Au growth seems to undergo a transition from 2D growth to 3D growth, in order to minimize the whole surface energy. On the other side, the strength of Au-ZnO interaction is largely weakened after too much Au is loaded on the surface, and the adatom-adatom interaction begins to dominate the growth of Au, resulting in the formation of new Au clusters.

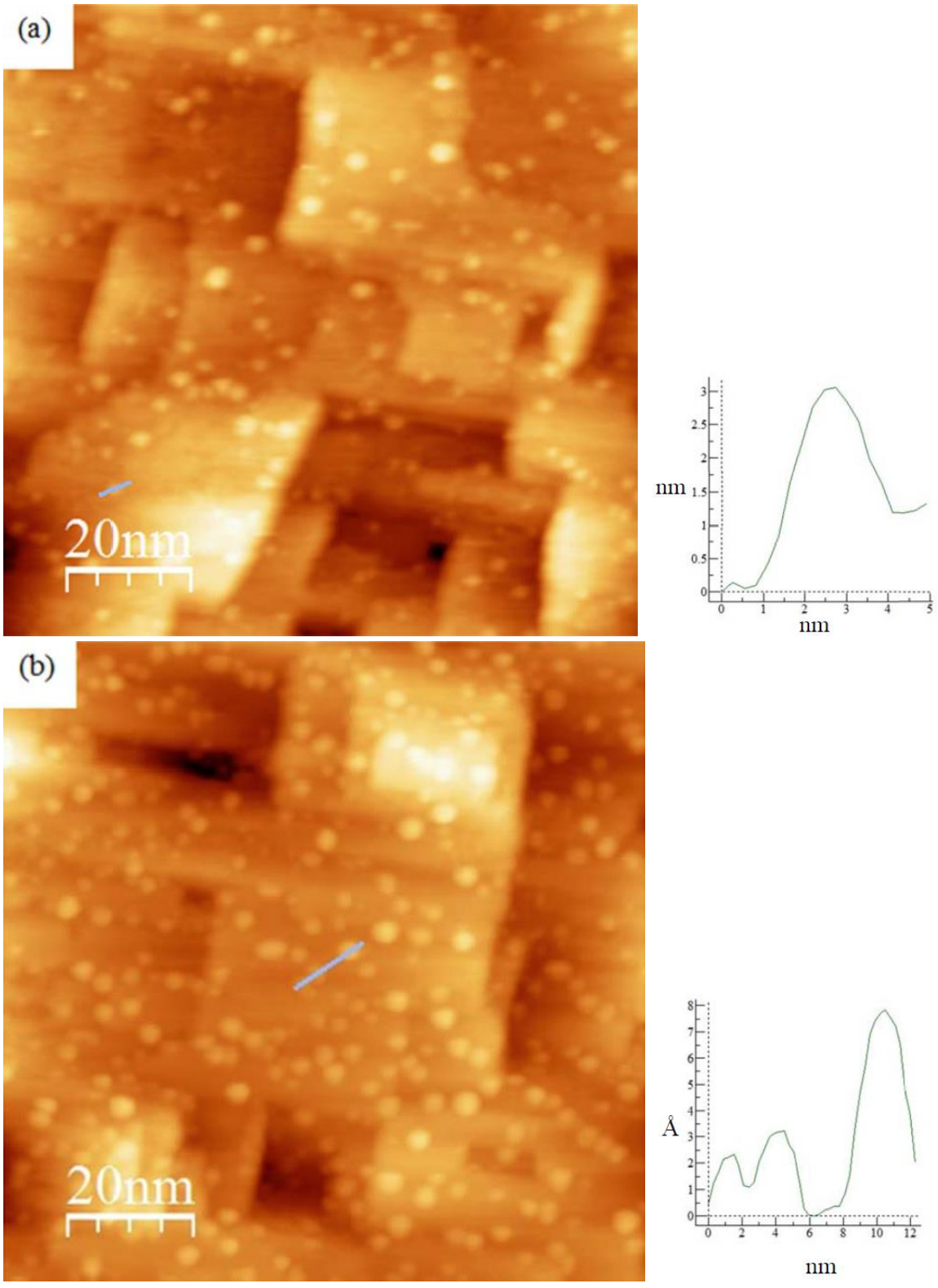

Figure 4.1 STM image of (a) 0.05 ML, (b) 0.4 ML, (c) 3ML Au on ZnO surface (Thanks Fei Wang for taking STM data) [39]

(Figure 4.1 continued)

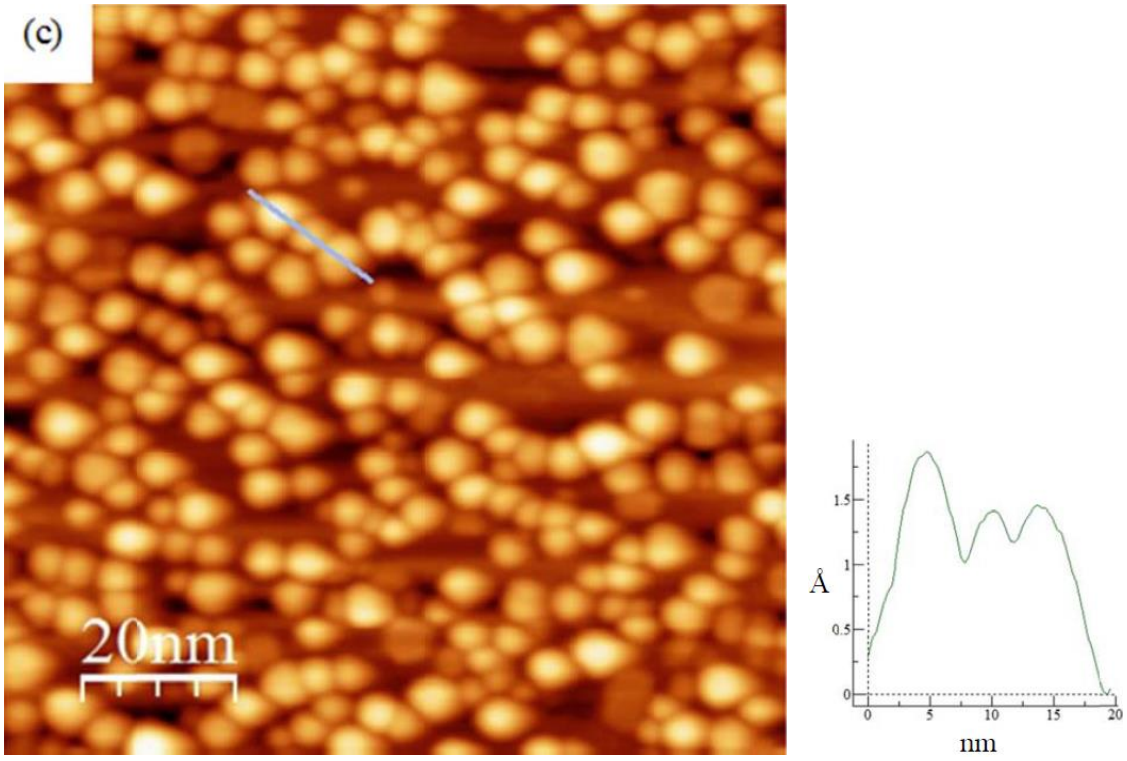

Figure 4.1 (c) exhibits the STM image of 3ML Au on ZnO with a larger size of Au clusters (7 nm across and 1.5 nm high) and no 2D Au layers could be found here. Similar to the other two samples, these Au clusters are localized at the step edges and terraces. Following the VW growth model, 3D growth of Au clusters is caused by the strong Au adatom-adatom interaction, while the ZnO support has a very small interaction with the Au adatoms. Here comes one interesting question: why the growth model of Au is so different from that of Cu? And why no favored adsorption sites are found for Au? To answer the above question, we want to notice the unique properties of Au first. Gold is known to possess the highest electronegativity and a relatively higher cohesive energy. And it also has a high electron affinity and ionization patential, which determines no stable oxide could be formed by Au. Previous studies also reveal anoth unique ability of Au known as aurophili bonding, which allows Au to interact with itself and form

superstructure of gold molecules. That is why the defect sites on ZnO surface does not affect the nucleation of Au clusters, in contrast to the Cu on ZnO system.

The above samples are annealed at 400 ℃ in UHV and their STM images are shown in Figure 4.2. The 0.4 ML Au on ZnO sample does not show any difference before and after being annealed at 400 ℃, which suggests the temperature is not sufficiently high to break the strong adatom-substrate interactiona and allow for the diffusion of Au atoms. (Figure 4.2 a) On the 3 ML Au on ZnO sample in Figure 4.2 b, Au clusters becomes larger without an increased height after high temperature pretreatment. As discussed above, the adatom-substrate interaction has been weakened at high coverage, which should be responsible for the ripening of small Au clusters into big ones. Moreover, the mean distance to nearby Au clusters at high coverage is much shorter that at low coverage, and a much lower diffusion energy is required on 3ML Au on ZnO.

4.2.2 LEIS

The surface composition is a key factor to influence the catalytic reactivity and selectivity of the heterogenous catalysts. As a surface-sensitive tool, LEIS was employed here to investigate the chemical components of the prepared samples' surface. Figure 4.3 displays how the surface components changes with the substrate temperature. Three peaks are shown at 1300 eV, 1780 eV, 1880 eV, which is corresponding to O, Zn, Au peaks respectively. We need to notice that the unexpected 1630 eV peak would decrease with the time, because of very little amount of impurities from ZnO bulk. It is suprising that the Au peak is decreased with the increasing substrate temperature. As shown in STM images, the mean size and distribution of the Au clusters does not show any difference before and after annealing treatment. The only possible reason for the reduced

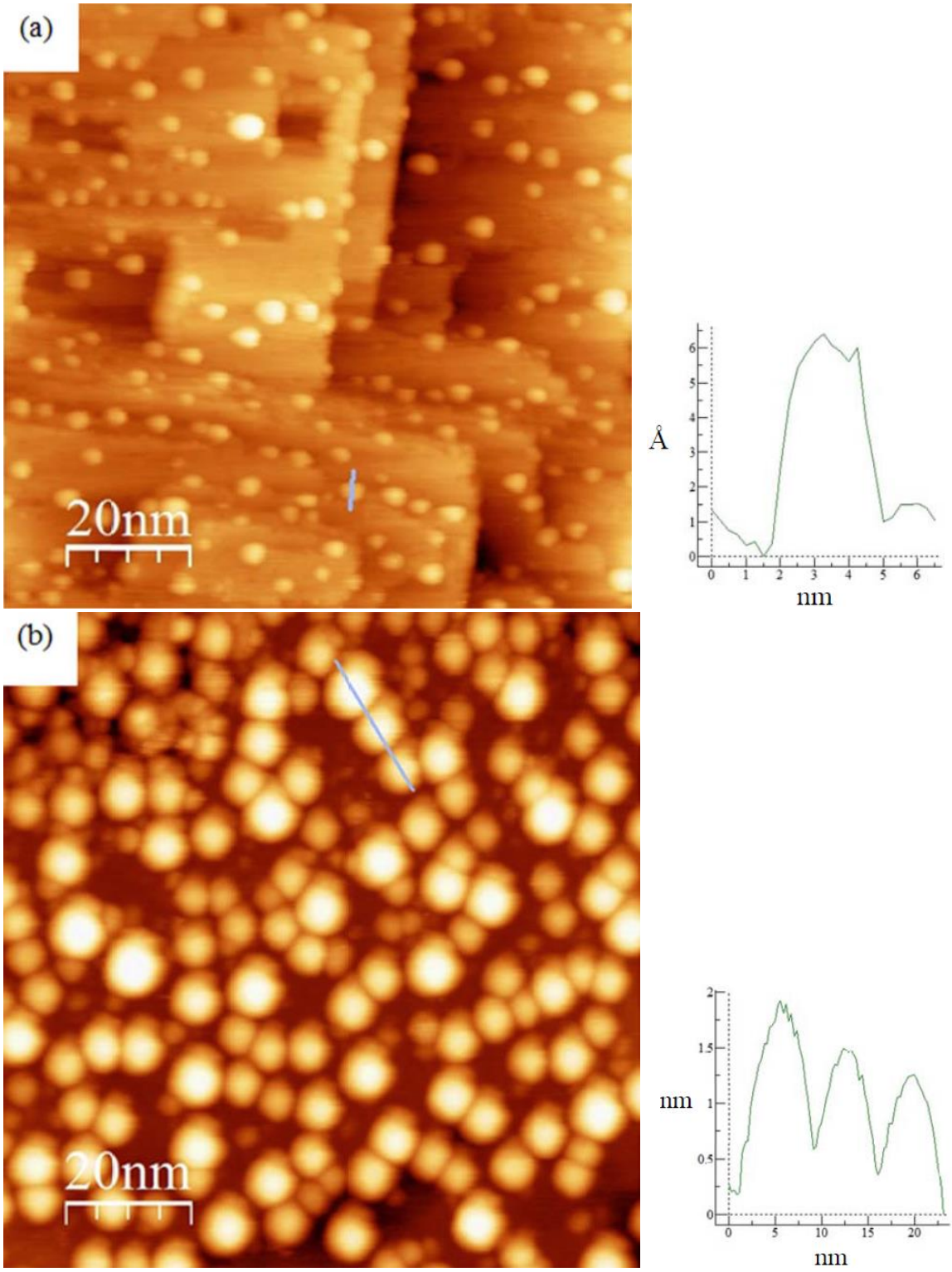

Figure 4.2 STM image of (a) 0.4ML and (b) 3ML Au on ZnO surface after being annealed at 400 ℃ for 20 min. (Thanks Fei Wang for taking STM data) [39]

Au ratio is that the perimeter of Au clusters is decorated by ZnO films. At 850 K, the Au peak is totally removed, indicative of full encapsulation of Au clusters by ZnO support. The thermal energy is no doubt the driving force of ZnO diffusion and that is why the encapsulation rate of Au is relevent to the annealing temperature. Inspired by the Cu on ZnO experiments, the Au on ZnO samples are also pretreated under the oxidizing conditions. Similar to the annealed samples, the Au peak decreases with the increasing annealing temperatureand the full encapsulation of Au clusters occurs at 750 K, which is much lower than that of the annealed sample.(Figure 4.4) As known, the heat formation of AuO_x is positive, and thus no Au clusters could be oxidized into AuO_x even under strong oxidizing conditions. The above findings deviate from those on Cu on ZnO samples, however both of them reveal an unknown significant role of oxygen gas at high

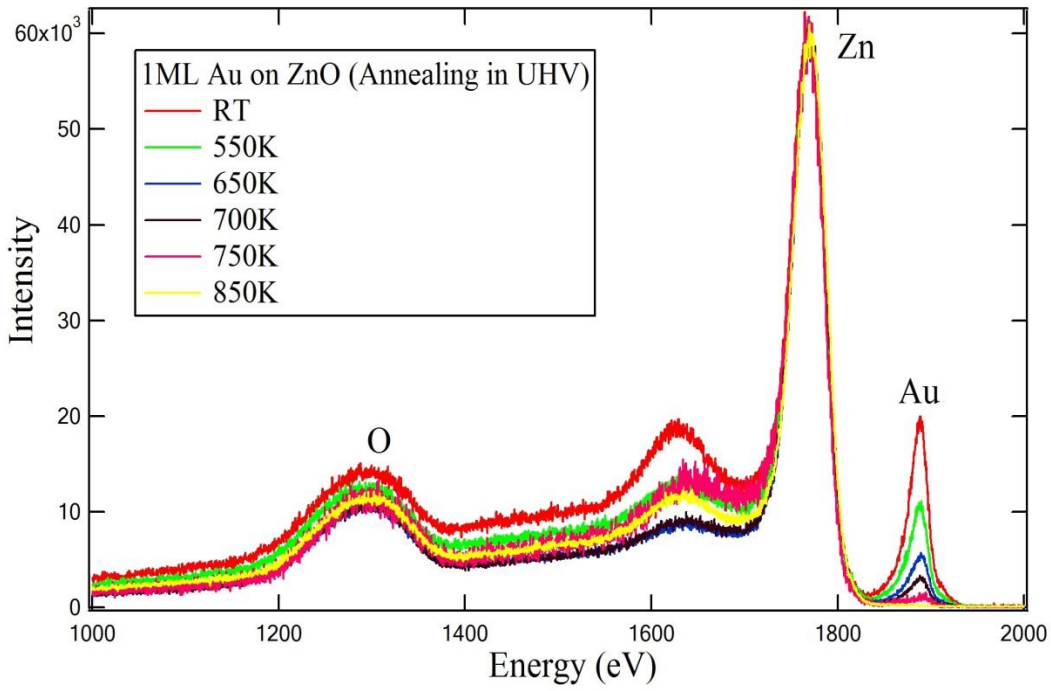

Figure 4.3 LEIS of 1ML Au on ZnO annealing in UHV at different temperatures

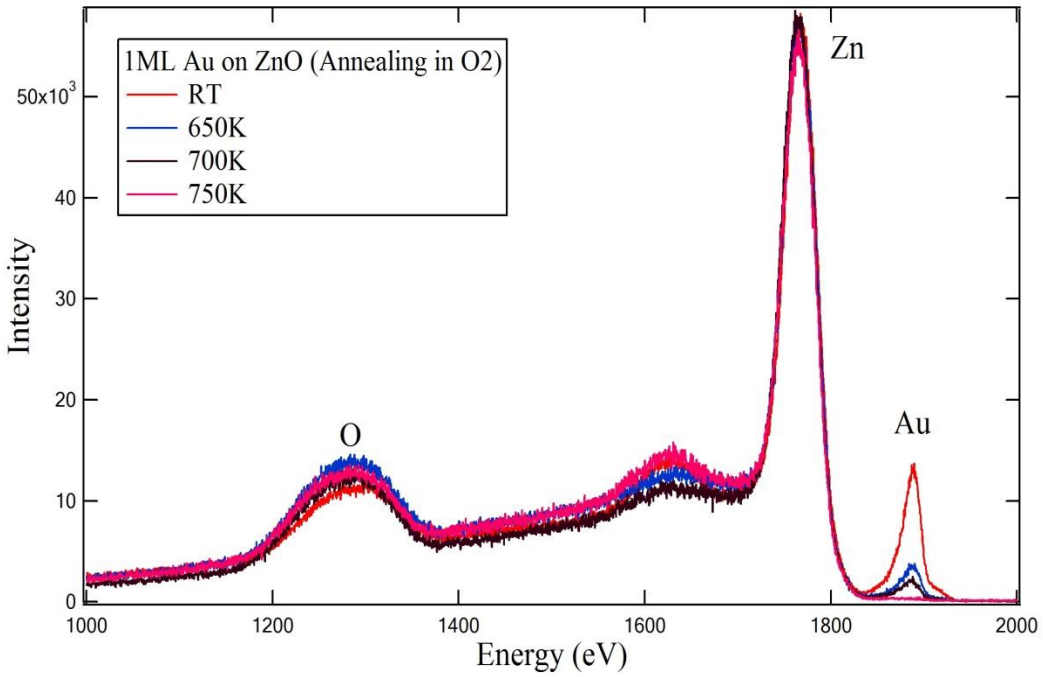

Figure 4.4 LEIS of 1ML Au on ZnO annealing in O_2 at different temperatures

temperature. The lower encapsulation temperature might be induced by the removal of the surface defects like oxygen vacancies under the oxidizing conditions, leading to a lower ZnO diffusion barrier.

Figure 4.5 presents the LEIS spectra of 2 ML Au on ZnO samples. A much higher Au peak is shown at room temperature, because of higher Au coverage. In the STM, the higher Au coverage would result in a higher density of Au clusters on the ZnO surface without the formation of larger clusters. As a function of the annealing temperature, the reduction of Au peak might be dominated by two factors: (1) the ripening and coalesence of small Au clusters, (2) encapsulation of Au clusters by ZnO. Even at 850 K, a small Au peak is still shown, suggesting that a higher aanealing temperature is required to achieve the full encapsulation. We need to notice that the annealing temperature here does not cause any change to the height of Au clusters, and would not affect the result of LEIS.

Therefore, the only possible reason for the decreased Au peak is the ZnO encapsulating Au clusters. Moreover, the higher encapsulation temperature at higher coverage indicates a higher diffusion barrier of ZnO, compared to the annealed 1ML sample.

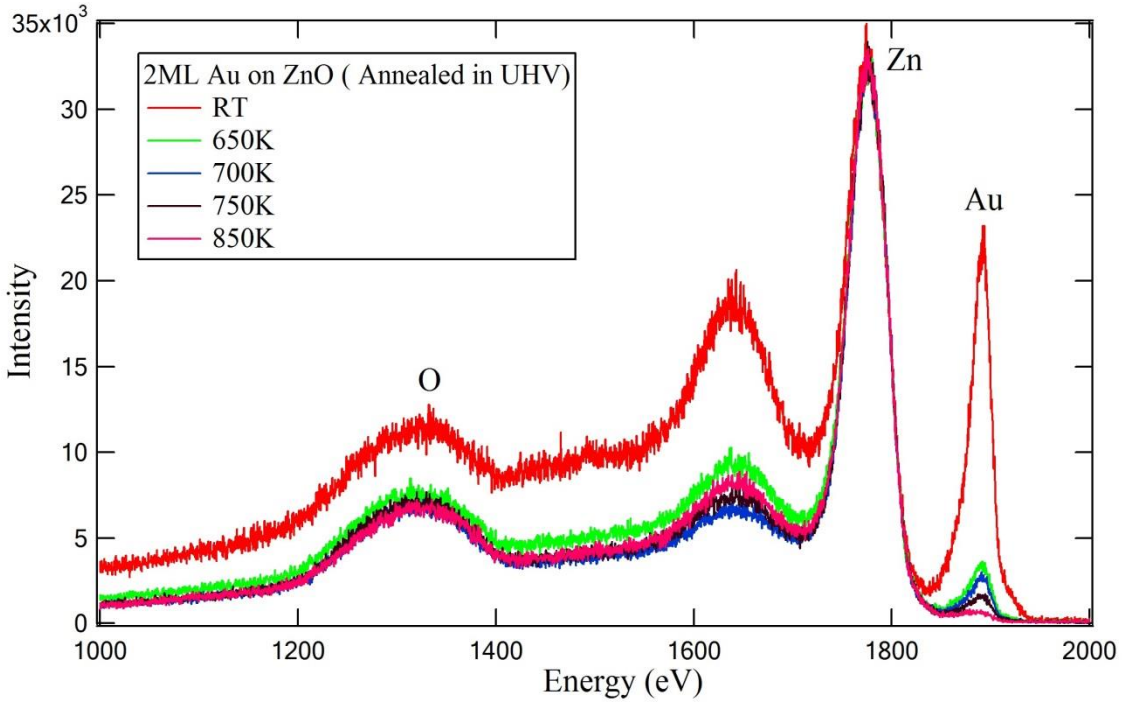

Figure 4.5 LEIS of 2ML Au on ZnO annealing in UHV at different temperatures

Followed by oxidation of the above sample shown in Figure 4.6, the Au peak at the temperature becomes lower than that of the annealed sample. The removal of Au signal occurs at 850 K, as a consequence of the surfactant role of oxygen. In addition, it also shows a higher encapsulation temperature, which supports the above hypothesis that the diffusion barrier of ZnO is highly relevent to the deposited Au coverage.

4.2.3 EELS

As introduced before, EELS is powerful tool to investigate the surface structure of the prepared samples, especially the top layers. In Figure 4.7 a, the red curve shows two

broad peaks at 2 eV and 4 eV, which are ascribed to 3*d*-interband transitions of Au nanoclusters and the interband transition from O 2p to the bottom of the conduction band

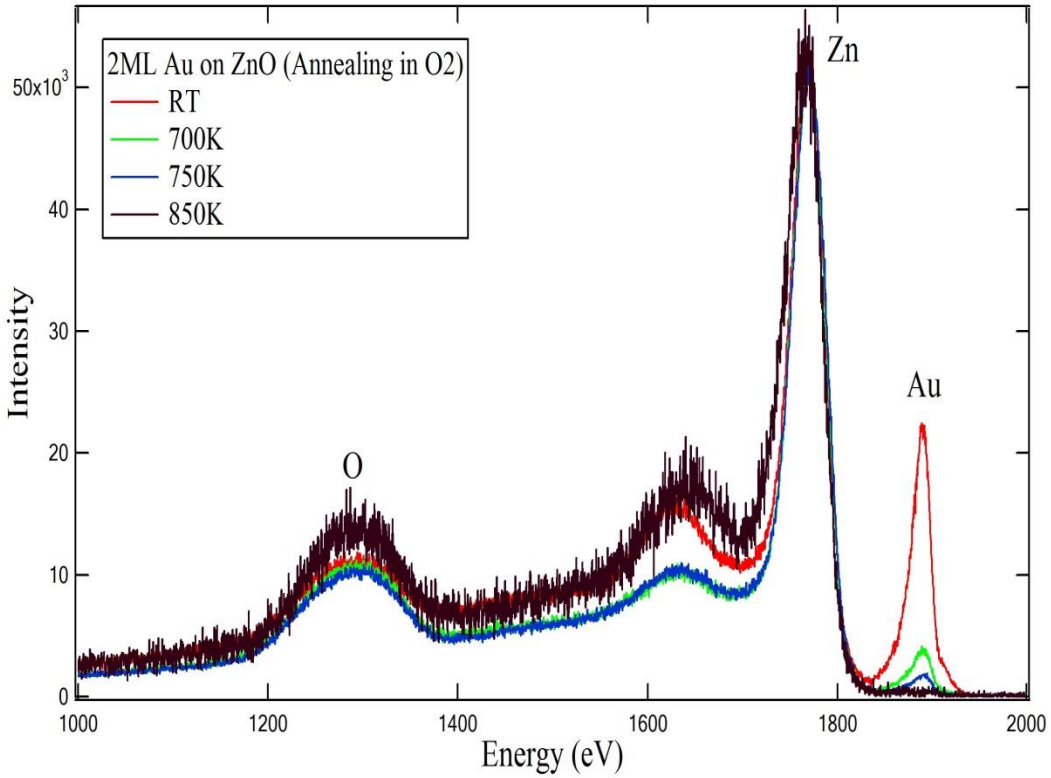

Figure 4.6 LEIS of 2ML Au on ZnO annealing in O_2 at different temperatures

of ZnO respectively. The annealing treatment greatly decreases the Au related peak, and the tiny peak (~2 eV) at 850 K reveals that some Au atoms is still lying atop the ZnO surface. This result is in a good agreement with the LEIS data, which demonstrates the annealing treatment without oxygen at 850 K could not result in full encapsulation of Au clusters.

After introducing oxygen to the chamber, 2ML Au on ZnO samples are oxidized at 750K and 850K, as shown in Figure 4.7 (b). The removal of Au signals is found in both samples, which is in good agreement with the corresponding LEIS findings. Using a combination of surface-sensitive techniques: LEIS and EELS, it comes to the same

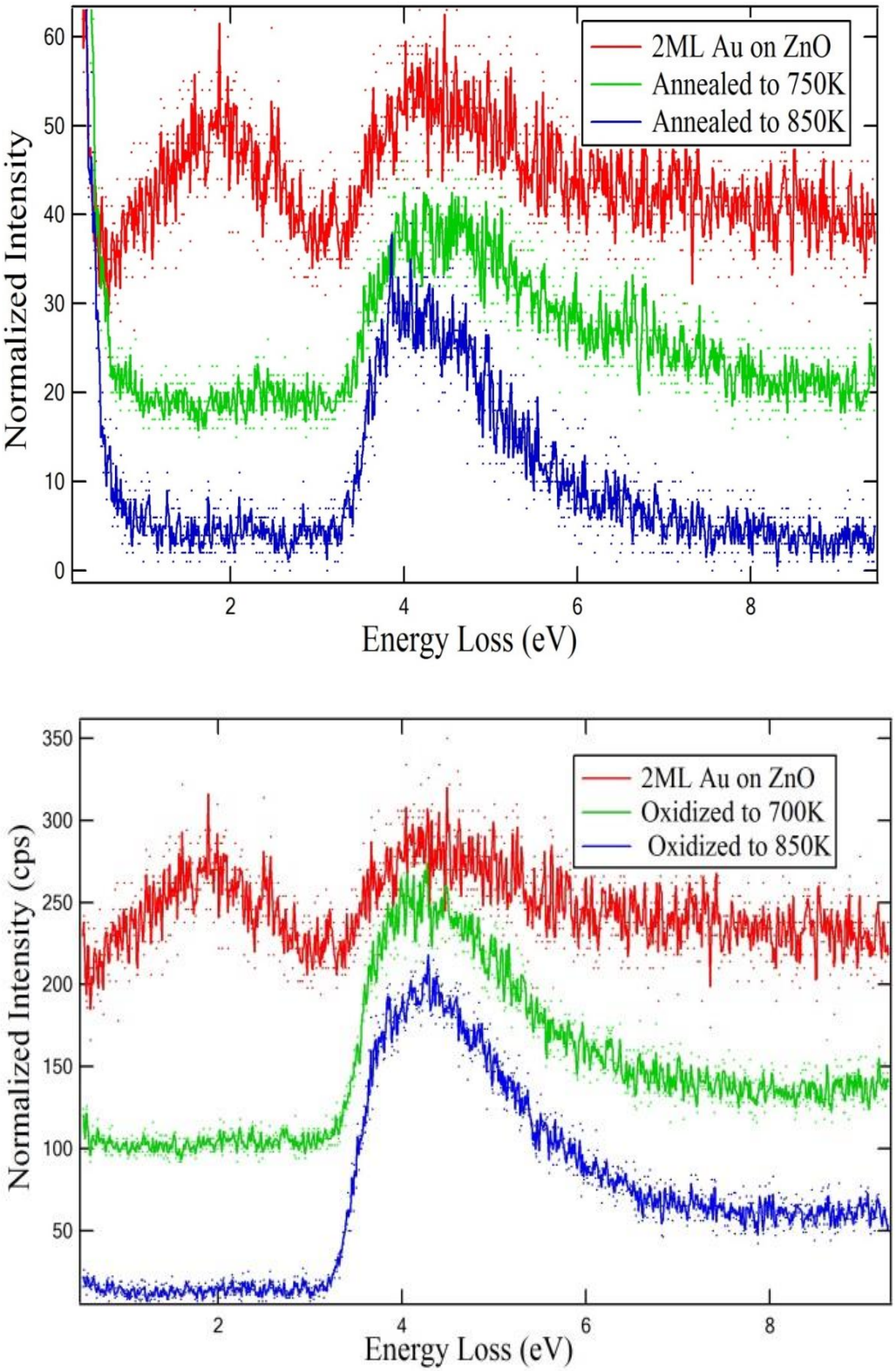

Figure 4.7 (a) 2ML Au on ZnO annealed at RT, 750K and 850K; (b) 2ML Au on ZnO oxidized at RT, 750K and 850K

conclusion that the high temperature pretreatment could result in ZnO encapsulation of Au clusters, and the addtive oxygen could affect the diffusion barrier of ZnO species.

4.2.4 CO Oxidation

From previous studies, CO oxidation is always a simple reaction to testify the catalytic performance of heterogeneous catalysts. As one significant characteristic of SMSI, the encapsulation behavior have proved to bring dramatic changes to the adsorption behavior and catalytic performance of heterogeneous catalysts, since the metal clusters are fully covered by the support. Besides the catalytic performance, it also enables us to learn the atomic and electronic structures of the prepared samples by investigating their CO oxidation behavior. Figure 4.8 shows how CO_2 formation rates varies with the reaction temperature on different pretreated 1ML Au on ZnO samples. All the three samples show very low CO oxidation rates below 650 K, and it is not surprising that all the highest reaction rates are found at 750 K. The RT 1ML Au on ZnO in the absence of interfacial SMSI effects has a lower reaction rate than the other two high temperature samples. Compared to the annealed sample, the reaction rate of the oxidized sample is slightly higher, even though the Au clusters have no changes in the presence or absence of oxygen. From the above LEIS spectra, a relatively higher encapsulation rate of Au clusters is found in the oxidized sample. Therefore, it seems more likely that the reaction rate might be dependent on the ZnO encapsulation rate of Au clusters. In other words, the active sites of CO oxidation might locate at these ultra-thin ZnO thin films, as a consequence of the SMSI effects. As shown in STM images, the low coverage samples possess higher morphological stability under the high temperature treatments and that is why the reaction rate for low coverge samples seem to remain stable.

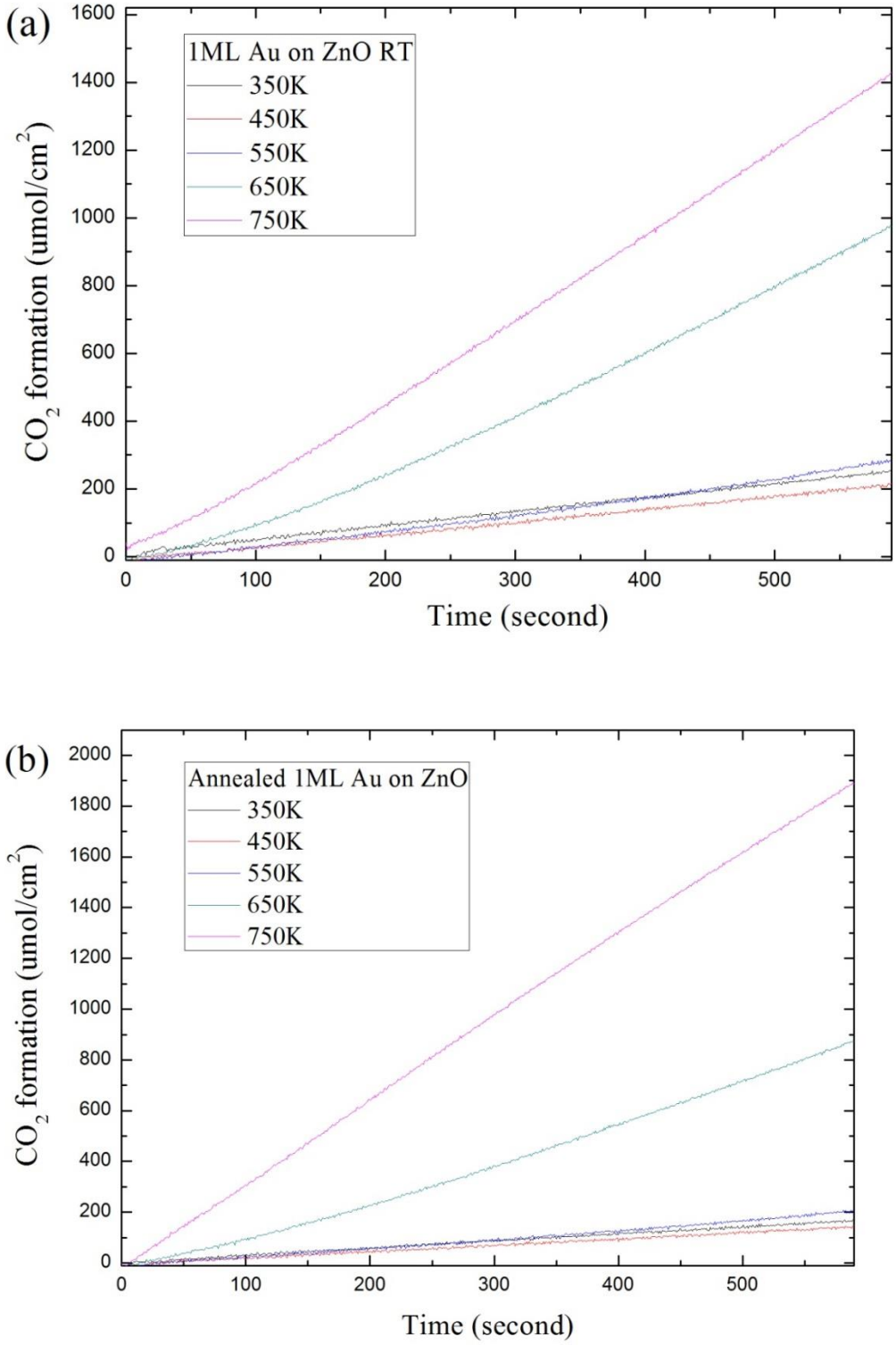

Figure 4.8 CO oxidation at 30~50 Torr CO and O_2 mixture ($CO:O_2$=2:1) on (a) 1ML Au on ZnO RT; (b) 1ML Au on ZnO annealed at 750K; (c) 1ML Au on ZnO oxidized at 750K

(Figure 4.8 continued)

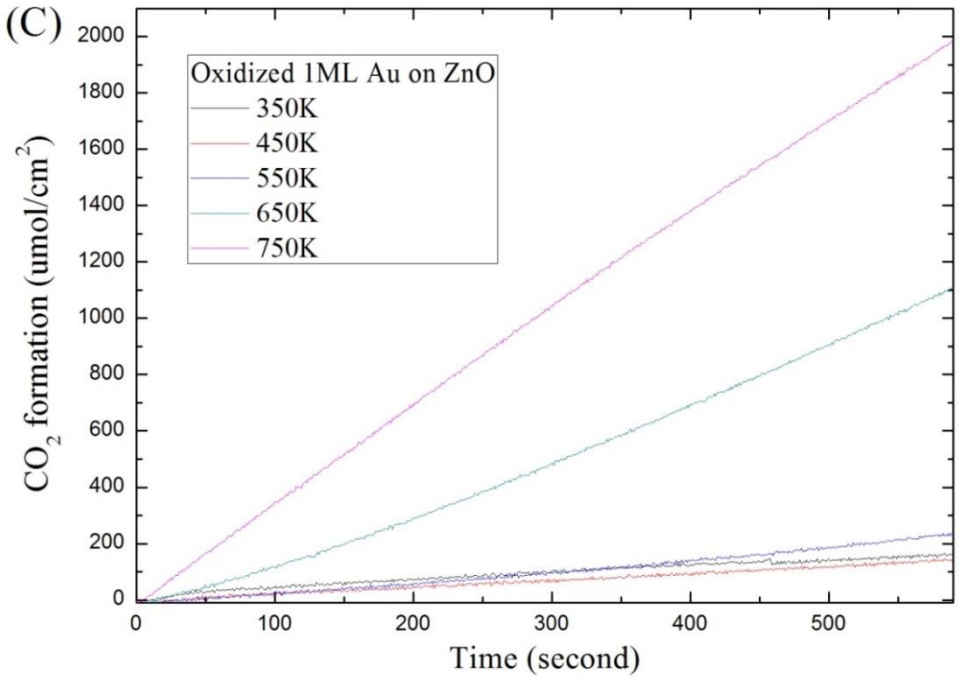

At high coverage (2 ML), the Au clusters undergo severe Ostwald ripening after annealing to 750 K and the annealed sample has a partial ZnO encapsulation of Au clusters. The highest CO_2 formaiton in Figure 4.9 are all found at the highest temperature (750 K) for the different three samples. In comparision with the low coverage samples, the CO_2 production has been greatly enhanced for high coverage smaples, in contrast with the results for Au on TiO_2 catalysts. The CO_2 formation rate at 750 K is shown in Figure 4.10 through fitting the above data. It is evident that the oxidized sample has much higher reaction rate, compared to the other two samples. Here we need to remind you about the STM images, in which the size of Au clusters becomes larger after the oxidation pretreatment. From numerous papers, larger Au cluster size always leads to lower reaction rate on the oxide supports. Therefore, it stands to a reason that the above exceptional catalytic reactivity should be ascribed to the new formed ZnO ultra-thin films

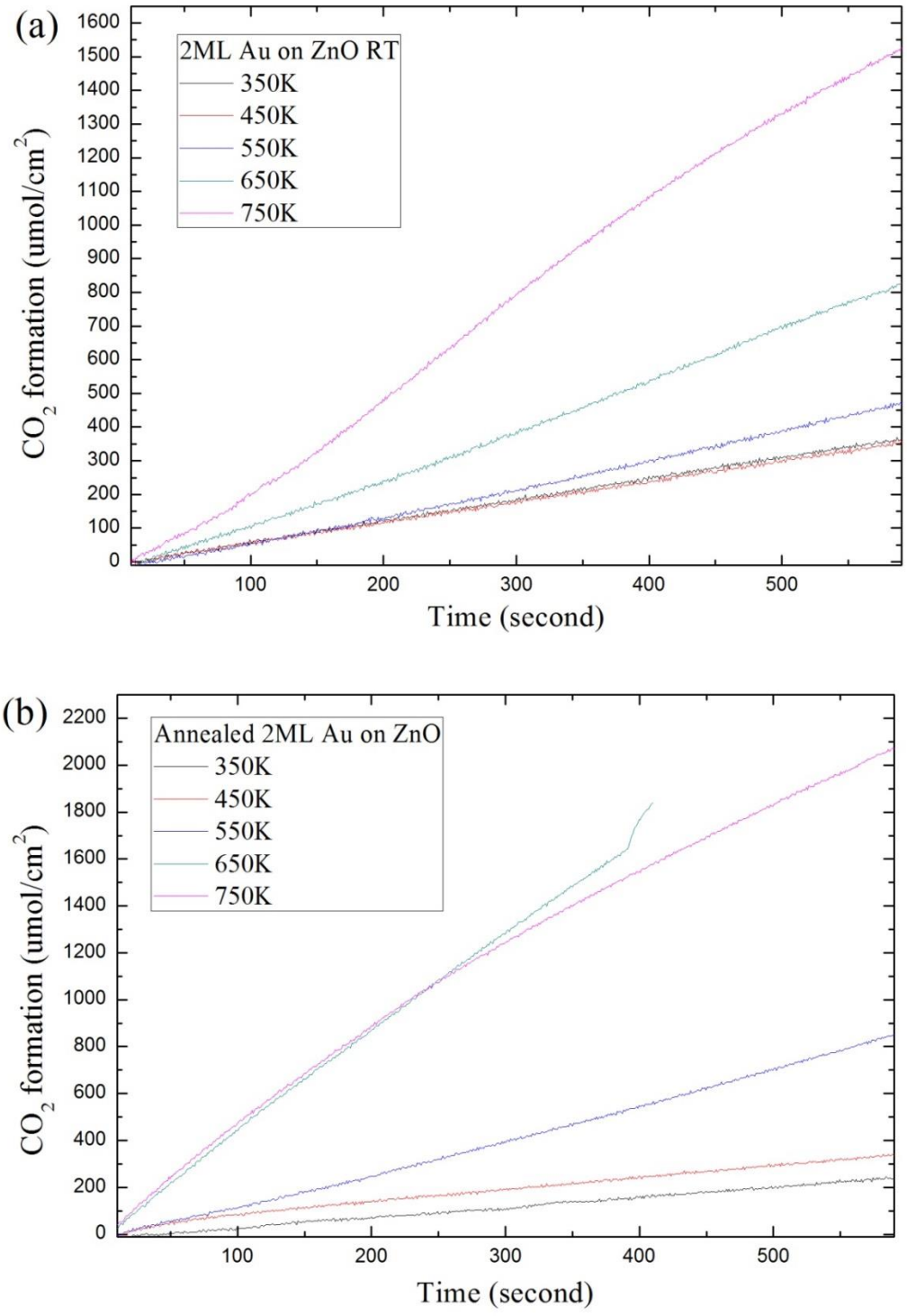

Figure 4.9 CO oxidation at 30~50 Torr CO and O_2 mixture ($CO:O_2$=2:1) on (a) 2ML Au on ZnO RT; (b) 2ML Au on ZnO annealed at 750K; (c) 2ML Au on ZnO oxidized at 750K

(Figure 4.9 continued)

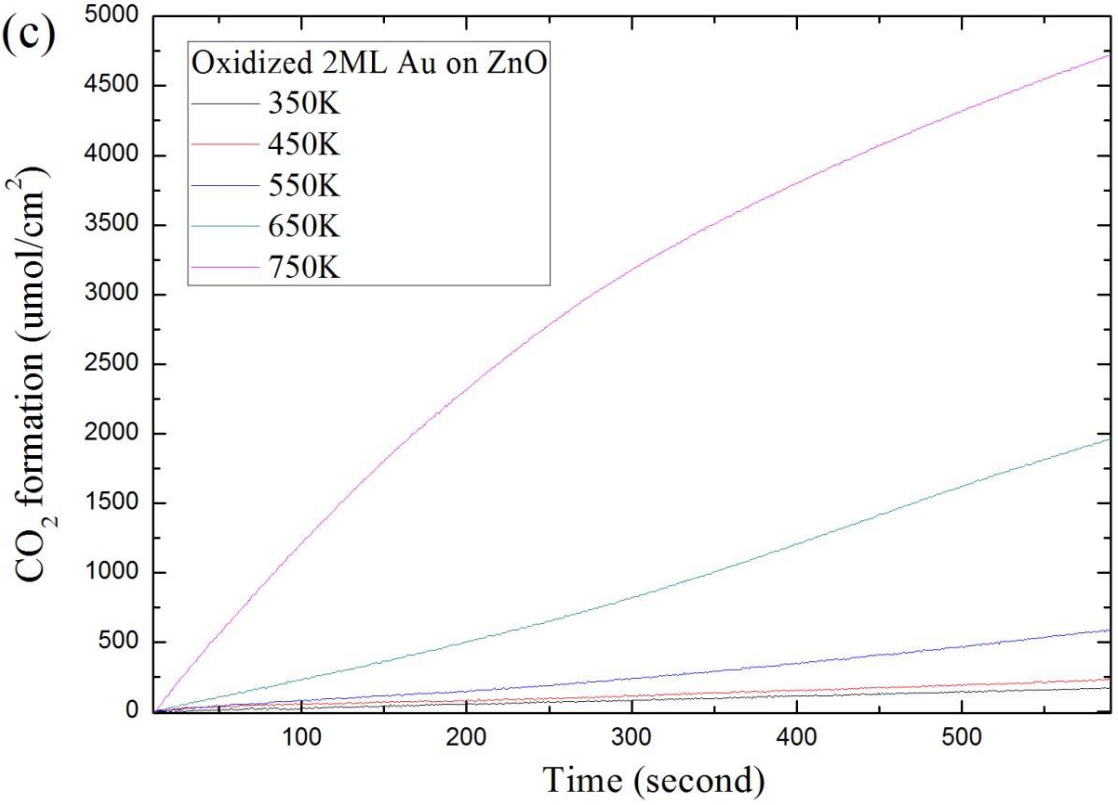

rather than Au clusters and the remarkable active sites are localized at these thin ZnO encapsulation layers. It is important to notice that the full encapsulation of Au clusters takes place at high temperature oxidation. Thus the higher Au coverage in the oxidized sample would result in higher surface area of ultra-thin ZnO films and subsequently a higher reaction rate of CO oxidation. Moreover, the CO_2 formation rate of the oxidized 2ML Au on ZnO is similar to that of the oxidized 2ML Cu on ZnO, which also indicates that the CO oxidation reaction is highly relevant to these ultra-thin ZnO films. The reaction rate of the above catalysts drops fast, which could be ascribed to the deactivation or the loss of reactants. To testify the above assumptions, we tried to perform the CO oxidation at different pressures without moving sample out of the chamber, in order to

avoid the influence of CO_2 formation. In Figure 4.11, the oxidized sample still shows a higher formation rate of CO_2 under a higher pressure, even after running in low pressures.

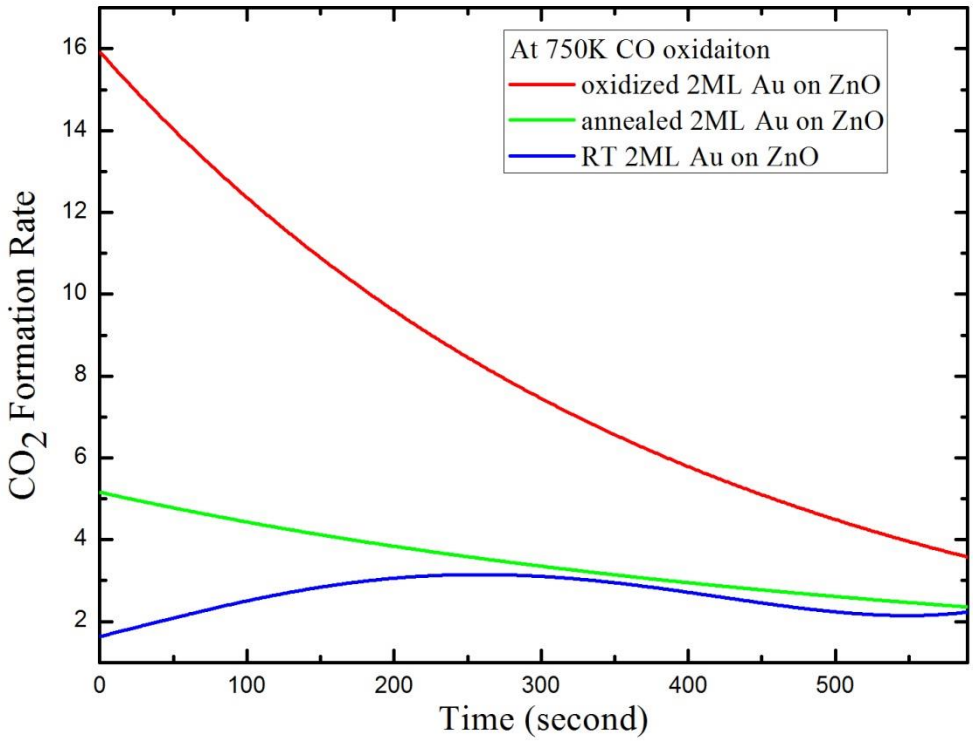

Figure 4.10 CO oxidation at 750K on the above prepared samples

Furthermore, the initial formation rate of both oxidized samples has an evident linear relation with the pressure, which provides a strong indication that no deactivation of the oxidized sample takes place during the CO oxidation reaction. As a result, the decreasing reaction rate is likely a consequence of the loss of reactants. In actual gas-phase catalytic reactions, the reaction rate depends on various factors, especially the partial pressure of reactants. That is because the probability of reactants bond to the active sites is proportional to the partial pressure of gas phase reactants. The cause for the drop of reaction rate is the ultra-high TOF of the active sites, since the reaction rate is only determined by the probability of reactants bond to the active sites. The significance of

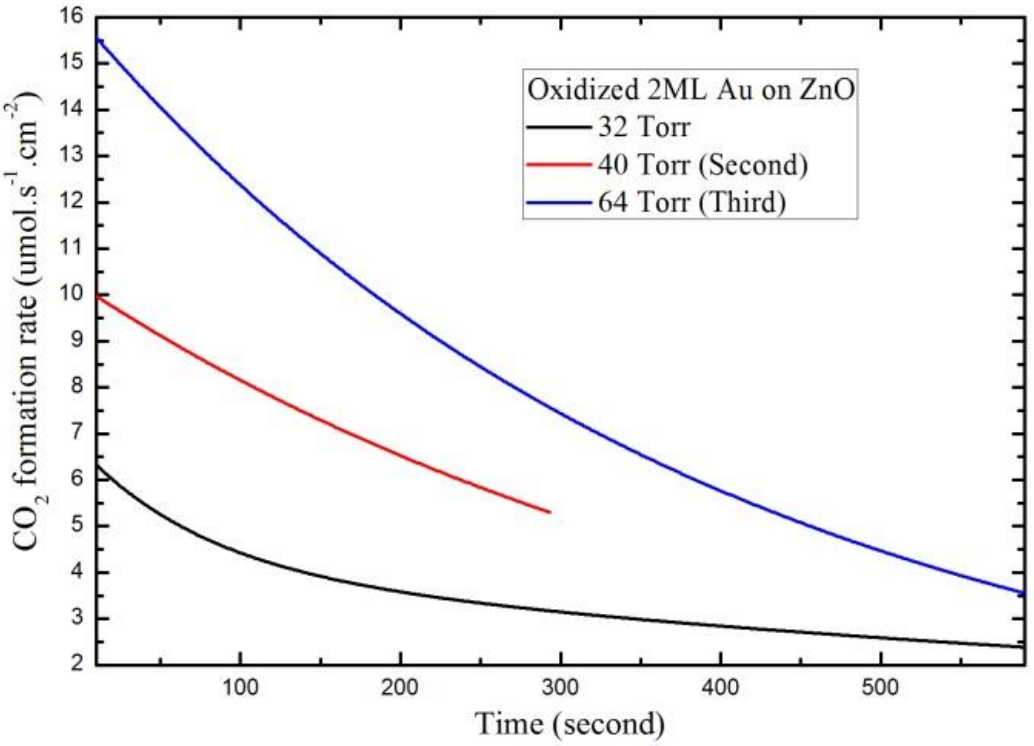

Figure 4.11 CO_2 formation rate at different pressure with a mixture of CO and O_2 (CO: O_2=2:1) on the same prepared sample. (Here the chamber is pump down to UHV and filled with the mixed gas. And then the same sample holds on to CO oxidation)

this high thermal-stability during the reaction is to demonstrate that the geometrical structure of the oxidized sample involving the encapsulation layers could be preserved in CO oxidation reactions.

After being oxidized, metal nanoparticles are encapsulated and confined inside a ZnO semisphere shell. As a consequence, the entire CO oxidation could only occur on ZnO sites of the surface. This surface phase transition from Au into ZnO should dramatically change the catalytic reaction mechanism. The ultra-thin oxide films formed on metal single crystal have proved to possess higher catalytic activity than the bare metal surfaces, although the reaction kinetics and mechanism are still subject to debate. [112] Y. Martynova has reported the reaction rate of CO oxidation on ultra-thin ZnO films (around

1ML) on Pt single crystal, is much higher than both Pt single crystal and ZnO nanoparticles. [18] The significance of above findings suggests that it should be helpful to confine our attention to the ultra-thin ZnO films, instead of the supported metal nanoclusters.

To approach a promising mechanism, it is crucial to develop an understanding of which factors determine the overall rates of the prepared catalysts. In actual catalytic reactions, the transformation of reactants into products relies on how the processed molecules fit the active sites of the certain catalyst. These metal supported ZnO thin films are shaped like semisphere, where fewer atoms participate on reconstructuring during catalytic turnover than single crystal surfaces. Thus, it is easier for the chemical bonds of reactants to rearrange on ZnO thin films and subsequently allows these chemical bonds to be broken and reformed. Therefore, a lower activation barrier is required to start the chemical reactions, as found in core-shell nanocatalysts. [113]

Atomic steps containing lower coordination sites are believed to be active sites for catalytic reactions. [108] That is why nanocatalysts always possess an exceptional reactivity, since they are believed to contain a high density of atomic steps. In our case, the high curvature of these semisphere-shaped nanostructured ZnO enables its surface to contain a large number of steps. These steps could enhance the chemical bonds of reactants and subsequently lower the activation barrier, resulting in a higher overall reaction rates.

Beside the above shape effects, charge transfer is always controversial, which alters the catalytic properties by changing the electronic structure of catalyst. The charge state of ultra-thin ZnO films is determined by the interaction between ZnO and the metal

nanoparticles. The electron is found to transfer from metal nanoparticles to ZnO, based on previous UPS data. The charge transfer would result in reduced ZnO species on metal nanoparticles, in good agreement with the findings in Cu-ZnO synergy from industrial catalysts. [115, 116] Previous studies of thin oxide films deposited on metal single crystal show that the charge transfer is very pronounced in ultra-thin films and decreases for thicker films. So it is possible to hypothesize that the ultra-thin ZnO layers should be highly charged, because of its limited thickness. Here we need to note that the modified charge state of ultra-thin ZnO layers varies with the supported metal nanoparticles, and subsequently leads to different selectivity. For instance, the catalyst for WGS reaction is CuO-ZnO-Al_2O_3 oxides, while Cu/ZnO/Al_2O_3 is preferred for methanol synthesis. [114, 115, 116]

Accordingly, the atomic and electronic structure varies with mass and charge transfer at high temperature pretreatment. The induced ZnO encapsulation layers with high density of atomic steps modify adsorbate bond strength, and therefore catalytic activity. The previous mechanisms based on metal surface (the Mars-van Krevelen and Langmuir-Hinshelwood mechanism) suggest that gas molecule (for example CO) react with lattice oxygen from the oxide or dissociated oxygen atoms on metal or oxidized metal surface to form the product. [114] In our case, the surface structure undergoes the transition from the metal phase to the oxide phase, definitely leading to a different mechanism of catalytic reactions. The O_2 dissociation could be dramatically facile at the atomic steps of ultra-thin ZnO layers, due to the interfacial charge transfer and low-coordinated ZnO dimers at the steps. In the meanwhile, Zn sites at ZnO surface are much better absorption sites for CO, compared to Cu single crystal and nanoparticles. So it enables the CO to

react with the nearby dissociated O atoms, avoiding the difficult O atom diffusion process. Thus, it would lead to lower activation barrier, higher surface area (instead of just the perimeters) and subsequently very high catalytic activity.

4.3 Summary

As another ZnO supported heterogeneous catalyst, Au on ZnO shows a simliar catalytic performance to Cu on ZnO in the same reactions: WGS reaction, methanol synthesis, methanol reforming. Previous efforts to understand this interesting phenomenon have relied on the support role of ZnO to determine the metal nanoparticles' catalytic properties. However, these earlier studies have generally failed to capture the nature of this important support role of ZnO. Here we have attempted to demonstrate an exceptional reactivity and stability by control over the atomic structure of the prepared samples.

Au deposited under UHV condtions appears to grow initially on the ZnO surface in a quasi-2D form, whereas Au forms 3D islands at a higher coverage. The cause for this unusual growth model is the strong interaction between Au and ZnO substrate. SMSI plays a decisive role in modifying atomic and electronic structure of heterogeneous catalysts. As part of SMSI, encapsulation is always of importance to understand the nature of SMSI, especially in TiO_2 supported cases. In contrast to the classical cases, encapsulation in our ZnO supported Au catalyst are found to be induced by the high temperature pretreatment, whereas the oxidation rather than reduction could promote the growth of ZnO thin films on Au nanoclusters. The activity difference under realistic conditons could be explained by considering the encapsulation rate of Au nanoclusters by ZnO support, which is ascribed to the various pretreatments. The ZnO thin films

isolate the Au nanoclusters and therefore inhibit the direct access of reactants to the Au nanoclusters. This transition of the catalyst surface dramatically changes the catalytic reaction mechanism, differing from the tranditional metal nanoparticles based mechanism. The SMSI effects, especially the charge transfter in the interface, contribute to the observed stability of the ZnO thin films both in morphology and chemical states. In this work, the structure of interface and nanostructured ZnO, are interlinked to its catalytic function, bridging the gap between surface science and catalysis. That is why it is the special combination of Au and ZnO possess a much higher catalytic performance than the individual Au and ZnO system.

Chapter 5: Cu on TiO_2

5.1 Introduction

The TiO_2 has always been a popular topic among the transition metal oxide, because of its wide applications: photocatalyst, heterogeneous catalyst, gas sensor *etc.*. [123, 124, 125] As a well-characterized material, TiO_2 has been proposed as a perfect model system for surface chemistry experiments, allowing experimentalists to study the mechanism of catalytic reactions by investigating the surface of TiO_2. Many different growth methods of metal clusters on TiO_2 have been developed to prepare various heterogeneous catalysts, and the presence of these metal nanoparticles greatly enhances the selectivity and reactivity of such heterocatalysts. In particular, TiO_2 as an important support plays a significant role in modifying the atomic structure of metal particles. For instance, the strong metal support interaction (SMSI) is owing to encapsulation of the metal particles by a reduced TiO_x overlayer, resulting in different adsorption behavior and catalytic reactivity. [123]

Metals have been explored for their catalytic properties over one hundred years. Among these metals, Cu based catalysts have attracted enormous attention, due to their numerous industrial and academic applications. In general, Cu based catalysts have higher activity, stability, and selectivity for desired products and Cu/TiO_2 has become one of the promising alternatives for precious metals in reducing CO_2 into fuel products. Based on Cu/TiO_2, a great number of catalytic experiments have demonstrated CO_2 reduction into CO, methane, and methanol, but the function of surface Cu species and the support role of TiO_2 are still under debate. [143, 144] According to previous studies on

the well-characterized TiO_2, pioneering surface-science investigations have been conducted to construct the mechanism of CO_2 adsorption and/or reduction on the surface. These previous studies have presented the importance of surface or subsurface defects, which have dramatic effects on CO_2 adsorption and catalytic reactivity of the surface. Highly dispersed Cu^+ species in TiO_2 have been suggested to be essential elements, whereas Cu^{2+} species show higher reactivity than Cu^+ and Cu^0 in Slamet's work. [136, 137, 138, 139, 140] Liu *et al.* reveals that surface oxygen vacancy provides the electron center (Ti^{3+}) and could work as active site to attract the oxygen atom of CO_2, while the deposition of Cu on TiO_2 helps dissociate the adsorbed CO_2. [142] And Qin *et al.* demonstrated that the heterojunction between CuO and TiO_2 could greatly enhance the reactivity. [141]

As one of SMSI materials, TiO_2 supported metal nano-particles always have a higher performance compared to non-SMSI support. And the geometric and electronic structure changes have been attributed to the strong interaction between the oxide support and metal nanoparticles. The geometric effect is assumed to change the area of the active metal surface in the catalytic reactions, while the electronic effect is induced by the charge transfer between the metal and the oxide support. That is how the SMSI tailors the selectivity and reactivity of a certain catalyst.

In this chapter, we would discuss the nature of SMSI effects on Cu/TiO_2 and these Cu nanoclusters are encapsulated by the reduced TiO_2 thin films, as found in other TiO_2 supported metal nanoparticles. Moreover, these SMSI effects have found to alter the electronic structure, resulting in different chemical adsorption of CO and subsequently the catalytic performance of CO oxidation.

5.2 Bulk Defect

Similar to the other metal oxides, bulk defects of TiO_2 are of particular interest, due to its significant role in a variety of surface phenomena, for instance the encapsulation of metal nanoparticles takes place while annealing to high temperature or reduced in H_2 is required. Li *et al.* have investigated the relation between crystal colors, conductivity, and bulk defects through EPR measurements. [118] These defects in reduced TiO_2 are very complex with various types, for example oxygen vacancies, Ti^{3+} and Ti^{4+} interstitials. That is why the defect chemistry of TiO_2 is highly dependent on the substrate temperature, oxygen pressure, and impurities. However, it is still a question how the above factors change the type of dominant defects in the crystalline. To answer the above question, a large number of research groups have focused on the diffusion mechanism of these

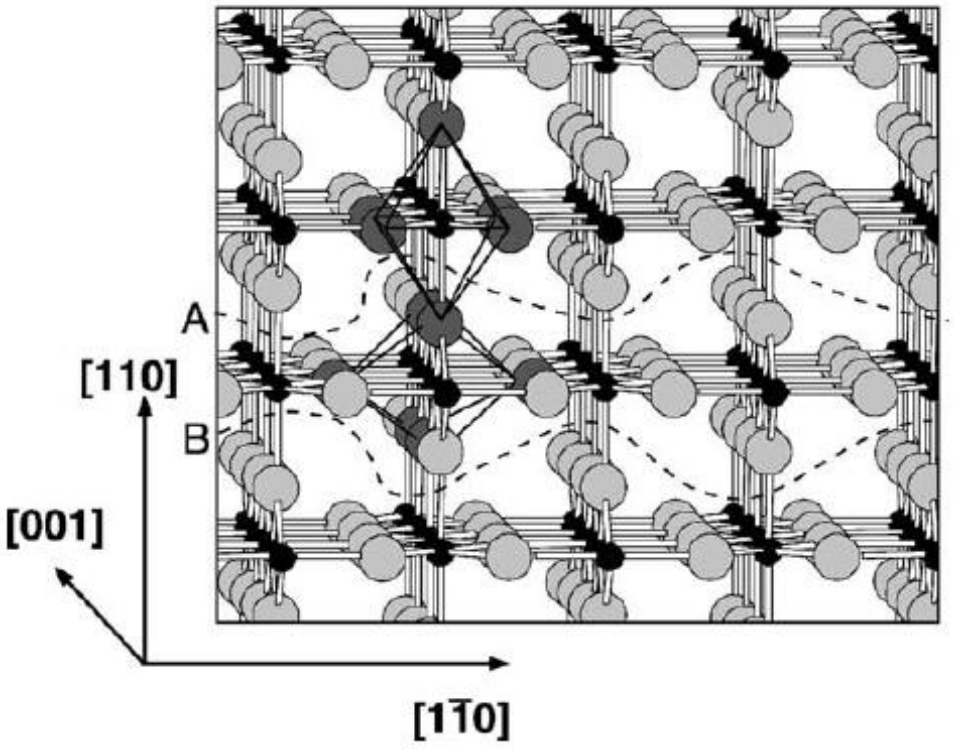

Figure 5.1 Ball and stick model of the rutile crystal structure. [127]

defects. From previous studies on TiO_2, the oxygen could migrate through a normal site exchange (vacancy diffusion) mechanism, while Ti interstitials are found to diffuse as interstitial atoms. [119, 120] Figure 5.1 shows how the Ti interstitials diffuse through the slightly distorted octahedral along the [001] direction. [121, 122]

5.3 Surface Defect

5.3.1 Step Edge

Clean TiO_2 surface are with a well-defined terrace structure, which could be attained by employing STM. Fischer has revealed the terrace size is increasing with the annealing temperature. [126] U. Diebold has shown a typical terrace-step structure in Figure 5.2 and the steps are 0.32 nm in height expected from the rutile structure. [128] In addition, step edges and kink sites are also of importance to surface chemistry, since they contain lower coordination number of surface sites, resulting in higher chemical reactivity.

5.3.2 Oxygen Vacancy

Oxygen Vacancy (O_v) plays an important role on surface chemistry of TiO_2, and could be produced by simple annealing pretreatment. Oxygen vacancies have been proposed by researchers to be the active sites for water splitting and CO oxidation. [123, 130] In Figure 5.3, it shows a STM image of TiO_2 surface and 'A' points are assigned as oxygen vacancies. [127] The size of bright spots is around 0.15 nm, in order of one single atom. These O_v defects could be healed by exposing oxygen into UHV chamber, in a good agreement with the decreased density of bright spots in STM. [129]

5.3.3 Ti^{3+} Defects

Besides oxygen vacancies, Ti^{3+} defects are another type of dominant defects on TiO_2 surfaces. As important agents for many adsorbates, Ti^{3+} defects could influence the

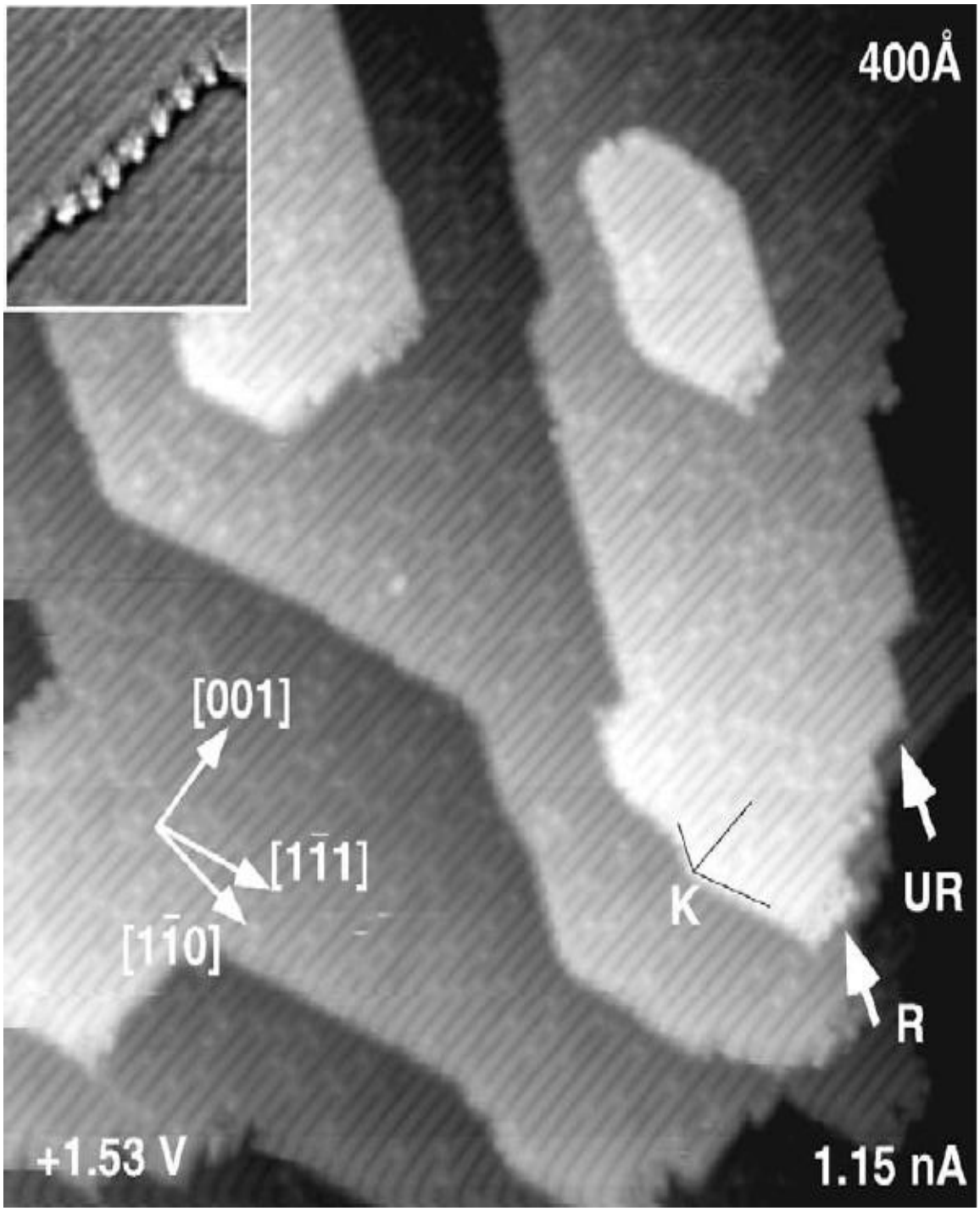

Figure 5.2 STM image of a clean TiO_2 (110)-(1x1) surface after sputtering and annealing to 1100 K in UHV. The step structure is dominated by step edges running parallel to (1-10) and (001) directions. A kink site at a (1-11) step edge is marked with 'K'. Smooth (UR) and rugged (R) (001)-type step edges appear with roughly equal probability and are marked with arrows. The inset shows a 10 nm x10 nm image of a reconstructed step edge. [127]

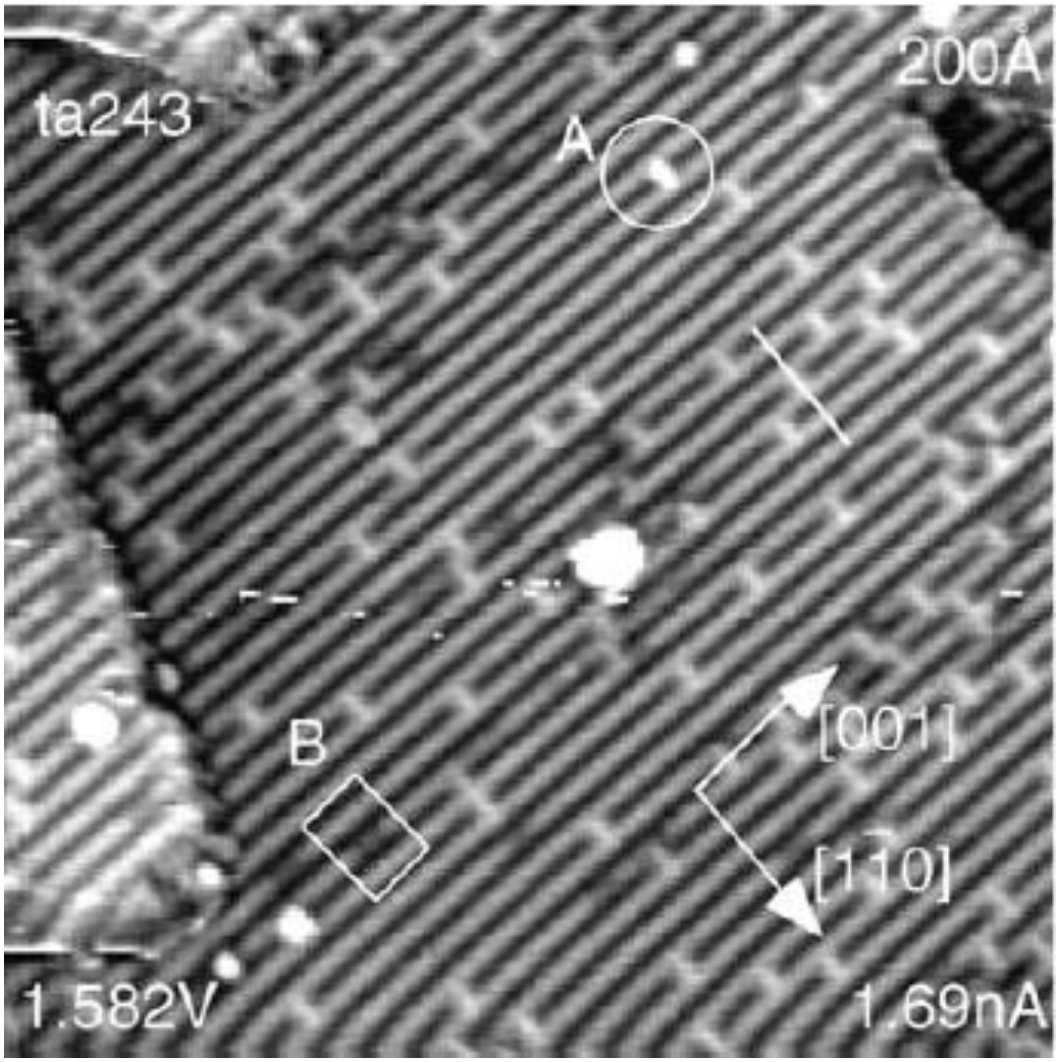

Figure 5.3 STM image of TiO_2 (110) surface, annealed in UHV to 1100K for 10 min. [135]

chemical reactions on these point defects. Moreover, it also plays a significant role in stabilizing the supported metal particles and enhancing their dispersion on TiO_2 surface.

Due to its importance in applications, many methods have been applied to produce Ti^{3+} defects, such as UV irradiation, heating under vacuum, reducing pretreatments. [131, 132, 133] And many techniques (XPS, TPD, EPR) have been employed to obtain valuable information to draw a figure of Ti^{3+} defects, in order to understand how these Ti^{3+} defects affect the reactivity and overall catalytic performance in certain reactions. It

is still under dispute that whether Ti^{3+} should be taken as the active sites for the desired catalytic reactions.

In Figure 5.4, it shows how the density of Ti^{3+} defects and oxygen vacancies changes with the annealing temperature in H_2 atmosphere. [134] The formation of Ti^{3+} defects could be completed through the electron transfer from oxygen vacancies to Ti^{4+}. These reduced TiO_2 species have high mobility and could diffuse to form the encapsulation

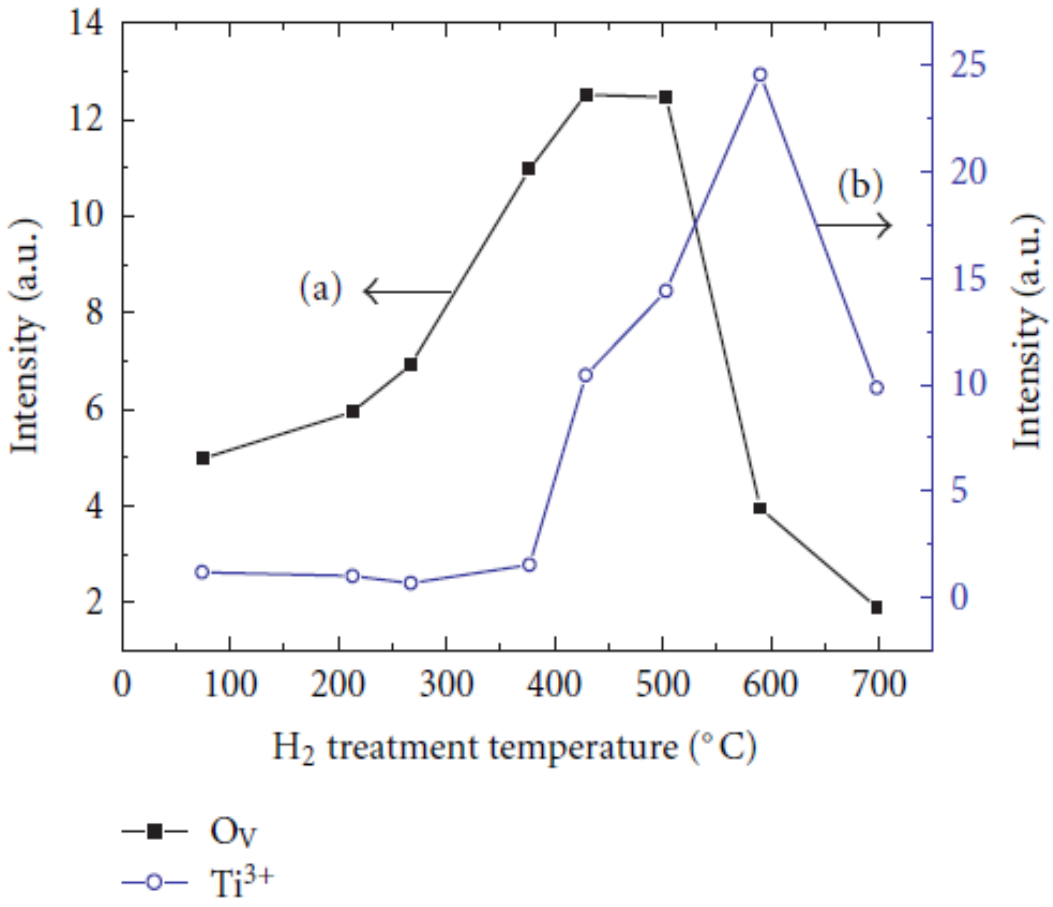

Figure 5.4 EPR intensity of Ti^{3+} and oxygen vacancies versus H_2 treatment temperature during the H_2 treatment. [134]

layer of metal nanoparticles. Moreover, the strong interaction between the metal particles and TiO_2 could change the pathway of the supported reactions. Previous studies

demonstrate that polar oxide films could be stabilized by the metal support but at a limited thickness of only a few atomic layers. This phenomenon is proposed to be the physical reason for the existence of ultra-thin encapsulation layer with the self-limited thickness. [19] The encapsulation is considered to be the characteristic of SMSI, which plays a decisive role in modifying atomic and electronic structure of the surface in heterogeneous catalysts.

In principle, both bulk and surface defects of TiO_2 play significant role on its electrocatalytic and photocatalytic reactions. M. Kong has reported the decreased concentration ratio of bulk defects to surface defects in TiO_2 nanocrystals results in a higher *e-h* separation efficiency and subsequently the enhancement of the photocatalytic performance. [135] The above findings reveal the bulk and surface defects have sort of internal relations, and thus the diffusion or transformation between them could bring changes to its chemical properties. Therefore, it may be possible to explain why the TiO_2 supported photocatalyst becomes deactive during the photocatalytic processes, if oxygen vacancies are taken as the active sites.

5.4 Experiments And Results

All the experimental work was performed in UHV chambers with a base pressure of less than $2x10^{-10}$ Torr. TiO_2 (110) single crystals were cleaned by several cycles of Ne^+ sputtering and annealing (650 ℃, 30 min). The surface was investigated by Auger spectra and LEED. This pretreatment was not completed until a clear LEED pattern was observed. The color of TiO_2 crystal changes from transparent to blue or black after the high temperature pretreatment. Therefore, a reduced TiO_2 surface with a relatively high density of oxygen vacancies results from the above pretreatment, and the dosage of

oxygen at a certain temperature could remove these oxygen vacancies. It was evident that these two types of TiO_2 (with defective and non-defective surfaces) would lead to different atomic and chemical structures of the surface, and subsequently result in different catalytic performance. After obtaining a clean surface, Cu was deposited at room temperature, using an e-beam evaporator with 99.999% Cu source. The deposition rate was calibrated from the STM images and the coverage of Cu could be controlled by changing the length of deposition time.

5.4.1 STM

Figure 5.5 shows different coverages (from 0.1 ML to 3ML) of Cu deposited on TiO_2 (110) at room temperature. It is evident that Cu undergoes 3D growth model for all the prepared samples, which indicates the interaction between Cu and Cu is stronger than that between Cu and TiO_2. As shown in Figure 5.5(a), Cu clusters are located at step edges and the arragement of these Cu clusters shows a prefered orientation. The step edges across the [001] direction are stacked with Cu clusters, whereas very few Cu clusters could be observed parallel to [001] direction. At higher coverage, Cu clusters begin to grow on the terraces, which becomes obvious in 3ML Cu on TiO_2. (Figure 5.5(d)) At 0.1 ML coverage, the average size of Cu cluster is around 5 nm in diameter and 1 nm in height, which equals to 3-4 Cu atomic layers. After increasing the Cu coverage to 0.5 ML, the average size of Cu clusters becomes 7 nm in diameter and 2-2.5 nm in height, where the number density of clusters remains the same, due to the limited number of favored nucleation sites on the step edges. 1 ML Cu on TiO_2 (110) and 3 ML Cu on TiO_2 (110) samples are exhibited at Figure 5.5(c) and (d) respectively. The average size of Cu clusters does not change with the Cu coverage, and the smooth terraces become new

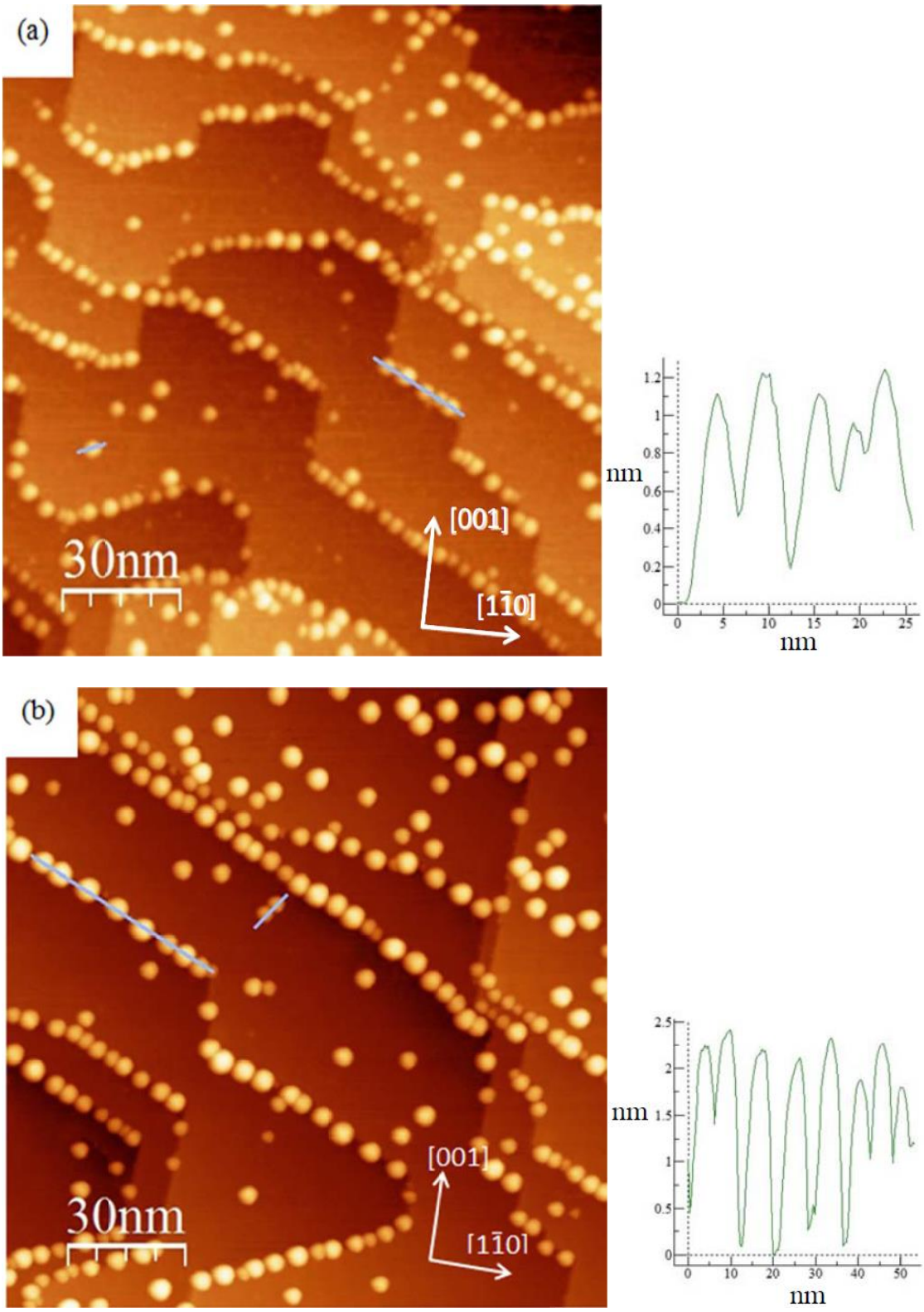

Figure 5.5 STM images of (a) 0.1 ML; (b) 0.5 ML; (c) 1ML; (d) 3ML Cu on TiO_2 (110) surface deposited at room temperature. (Thanks Fei Wang for taking STM data) [39]

(Figure 5.5 continued)

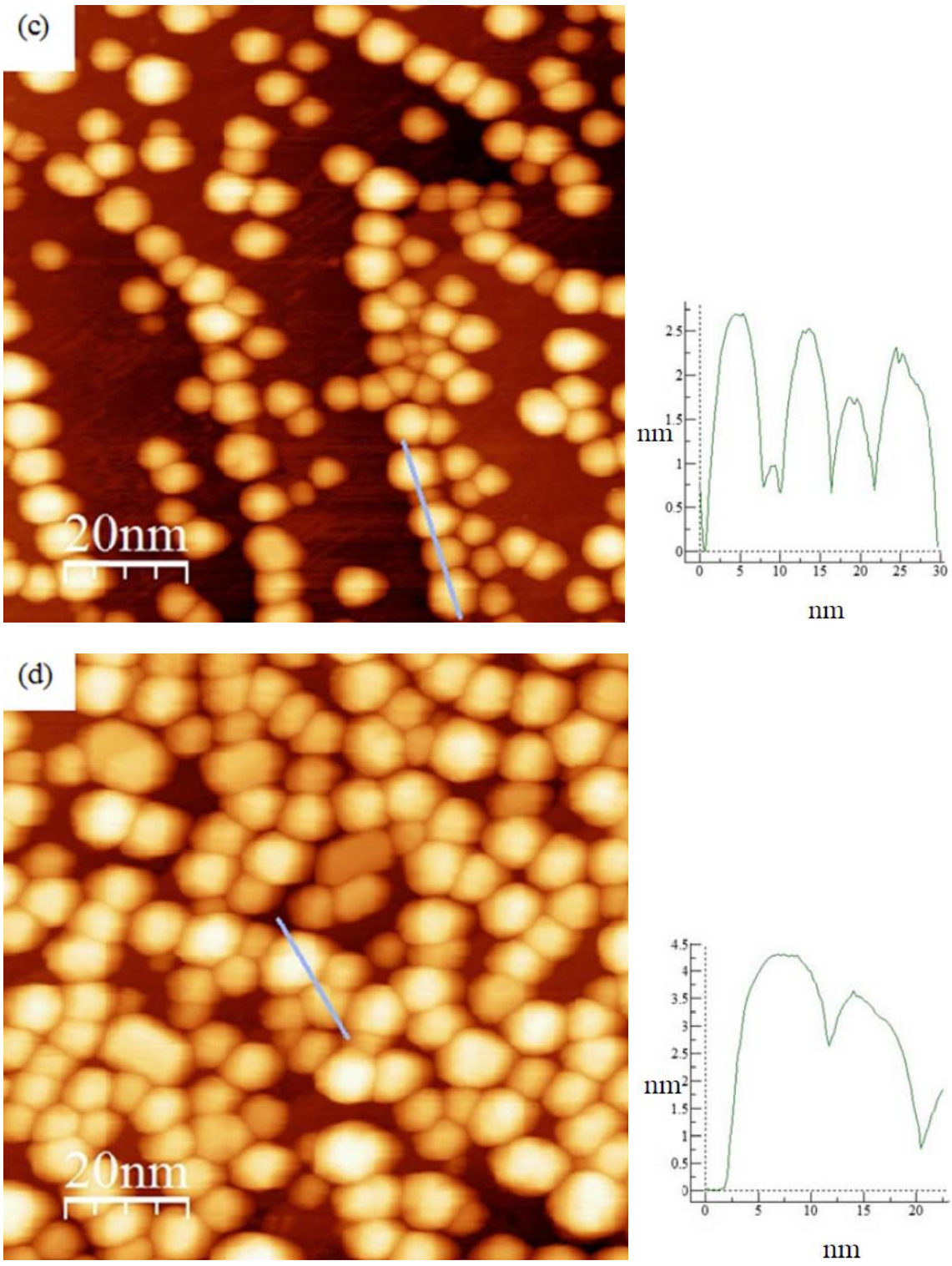

nucleation sites for the further deposited Cu clusters, as seen in our Cu on ZnO samples. [93] Addtion to the effect of Cu coverage, the annealing temperature is another factor to be paid attention, which plays an important role in modifying the surface structure. 0.5 ML and 3 ML Cu on TiO_2 (110) samples were annealed at 450 ℃ for 15 min and their STM images are shown in Figure 5.6 (a) and (b). No visible difference is observed both in size and density before and after the annealing pretreatment. Here we need to notice that the SMSI effects have been found in previous TiO_2 supported Cu clusters studies. The thickness of encapsualtion layers is usually self-limited to 1-2 layers, which just brings slight change to the clusters size. In spite of the ZnO burial, the sintering of Cu clusters does not take place at 400 ℃, since the annealing temperature is not sufficiently high. Cu clusters in previous study has shown to undergo ripening process at a higher annealing temperatures.[145] Compared to Cu on ZnO STM results, the ripening and/or sintering is stronger in Cu on TiO_2 case.

In Cu on ZnO experiments, the additive O_2 could react with Cu nanoclusters into Cu_2O and result in a lower diffusion barrier of ZnO. The following adsorption of CO_2 and CO oxidation experiments give quite disparate results before and after the oxidation of Cu clusters on ZnO. Moreover, the introduction of O_2 plays a dramatic role in reducing the surface oxygen vacancies. Here we attempted to anneal the above 0.5 ML Cu on TiO_2 in a low pressure of O_2. The Cu clusters have a significant change in Figure 5.7, due to the high temperature oxidation. The average size of these clusters becomes 8 nm in diameter and 4nm in height, which is much larger than the other two samples. It may result from three possible reasons: (1) O_2 could remove the surface oxygen vacancies, which could enhance the diffusion length of reduced TiO_x; (2) O_2, working as surfactant,

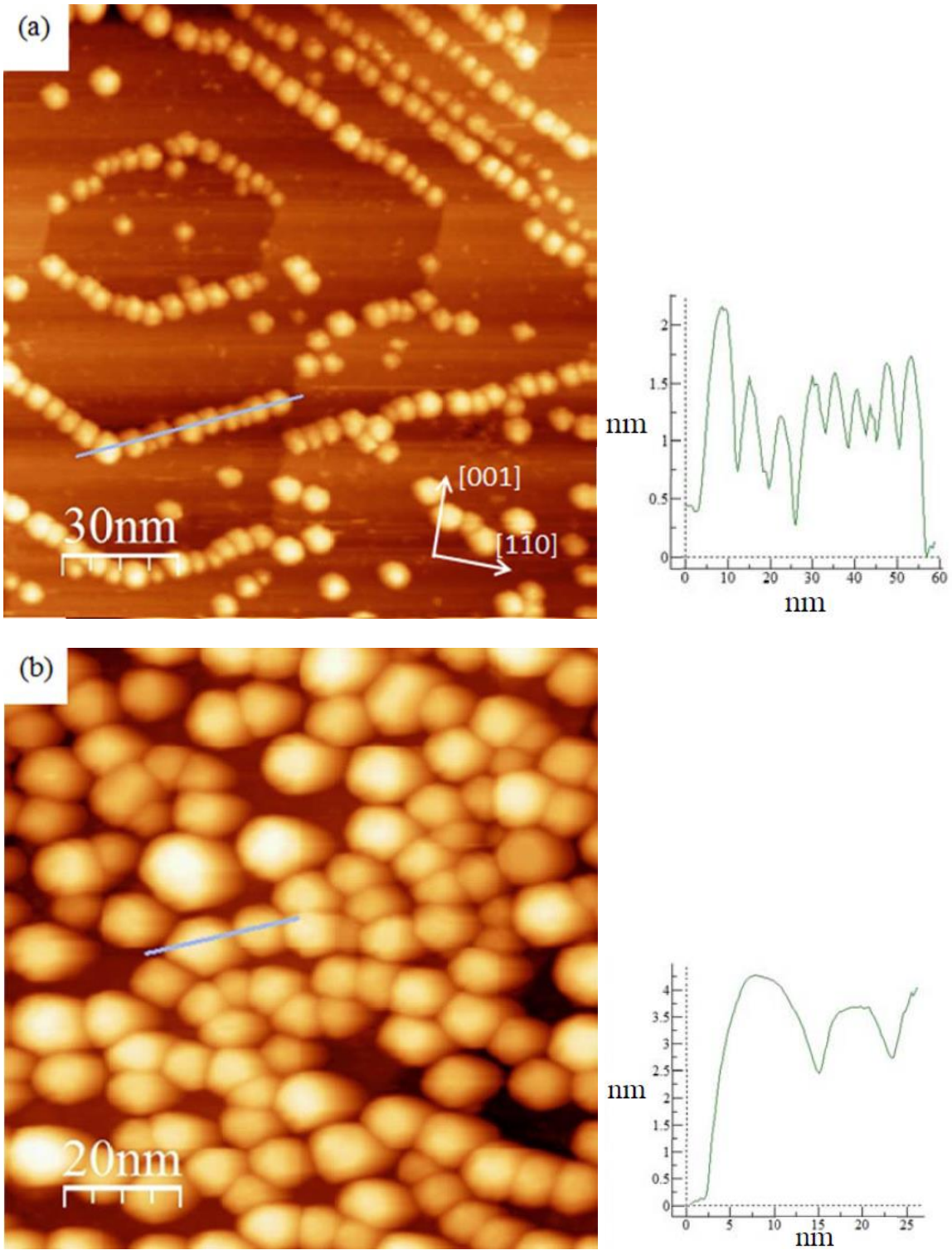

Figure 5.6 STM images of (a) 0.5 ML and (b) 3ML Cu on TiO_2 (110) after being annealed at 450 ℃ in UHV for 15 min. (Thanks Fei Wang for taking STM data) [39]

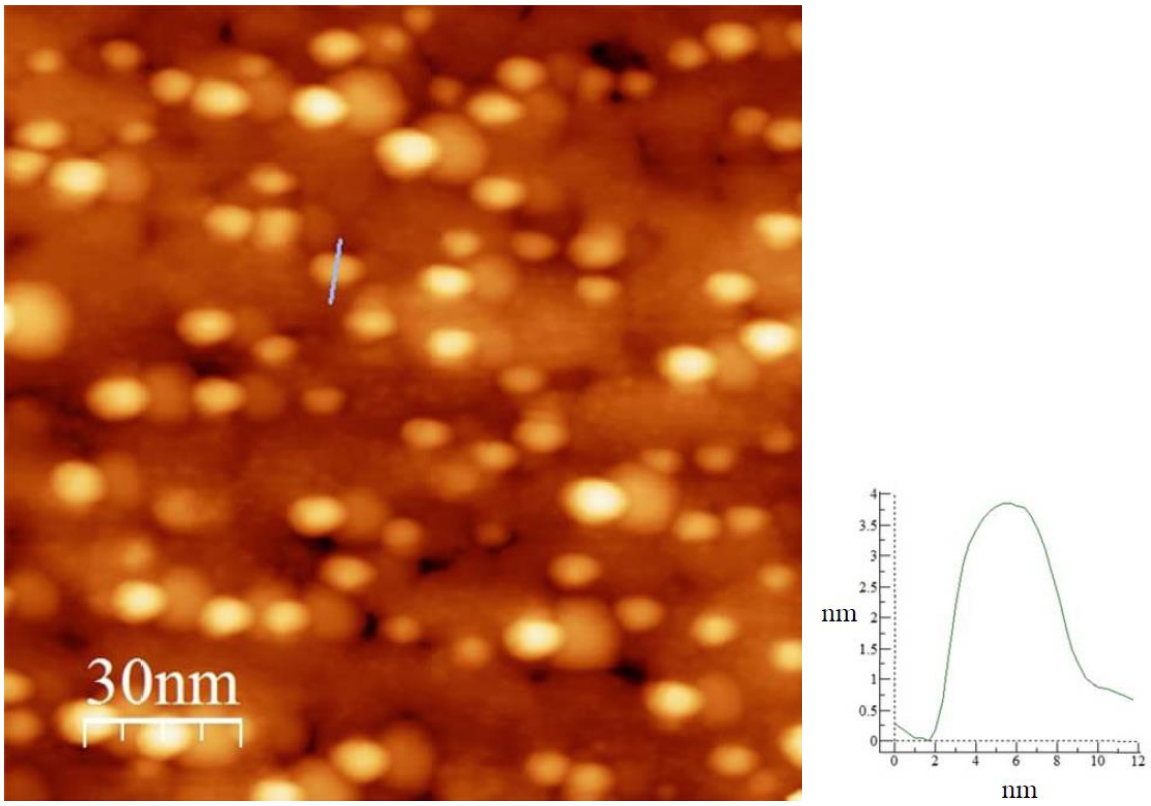

Figure 5.7 STM image of 0.5 ML Cu on TiO_2 after being annealed at 450 ℃ in $2x10^{-7}$ Torr O_2 for 15 min. (Thanks Fei Wang for taking STM data) [39]

reduces the diffusion barrier of Cu atoms, as reported in previous study that O_2 could be used as surfactants in Ag growth; [150] (3) The Cu clusters react with O_2 into CuO_x, which could reduce the total surface energy. The above factors may act together to yield the dramatic increase of the Cu clusters.

5.4.2 LEIS

To investigate the encapsualtion behavior, LEIS is employed to find out the chemical composition of the above samples' surface . The gas source used in this experiment is He, which shows a better resolution than Ne. First we start the new discussion with 1ML Cu on TiO_2 (110) sample. Figure 5.8 shows three peaks at room temperature for 1ML Cu on TiO_2: O peak (1250 eV), Ti peak (1660 eV), and Cu peak (1775 eV), respectively. The removal of Cu peak are induced by high temperature pretreatments, indicative of TiO_2

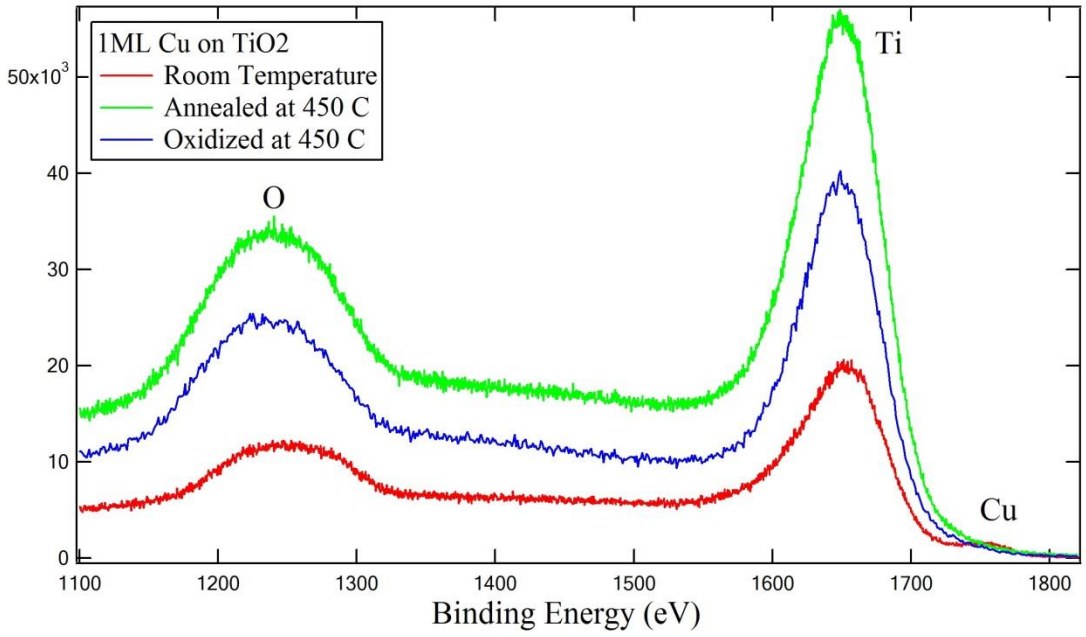

Figure 5.8 LEIS spectra of 1 ML Cu on TiO_2 under different pretreaments

encapsulating Cu clusters. Another interesting finding is that the ratio of Ti to O is the same in both annealed and oxidized samples, which suggests that the reduced TiO_x species are thermally stable under high temperature oxidation.

In Figure 5.9, 2 ML Cu on TiO_2 samples are prepared in a function of substrate temperature. The Cu peak is decreasing with the annealing temperature, whereas the O and Ti peaks are increasing. Furthermore, the removal of Cu clusters takes place at 350 ℃, indicative of encapsulation of Cu clusters by reduced TiO_2 species. It is important to note that STM images show a similar nanostructrure of the surface between the annealed and room temperature samples, which verifies the above assumption. Moreover, the drop of Cu peak at 250 ℃ should be owing to partially encapsulating Cu clusters by reduced TiO_x. It is evident that the thermal energy is the driving force for TiO_x diffusion, as found in other TiO_2 supported noble metal experiments.

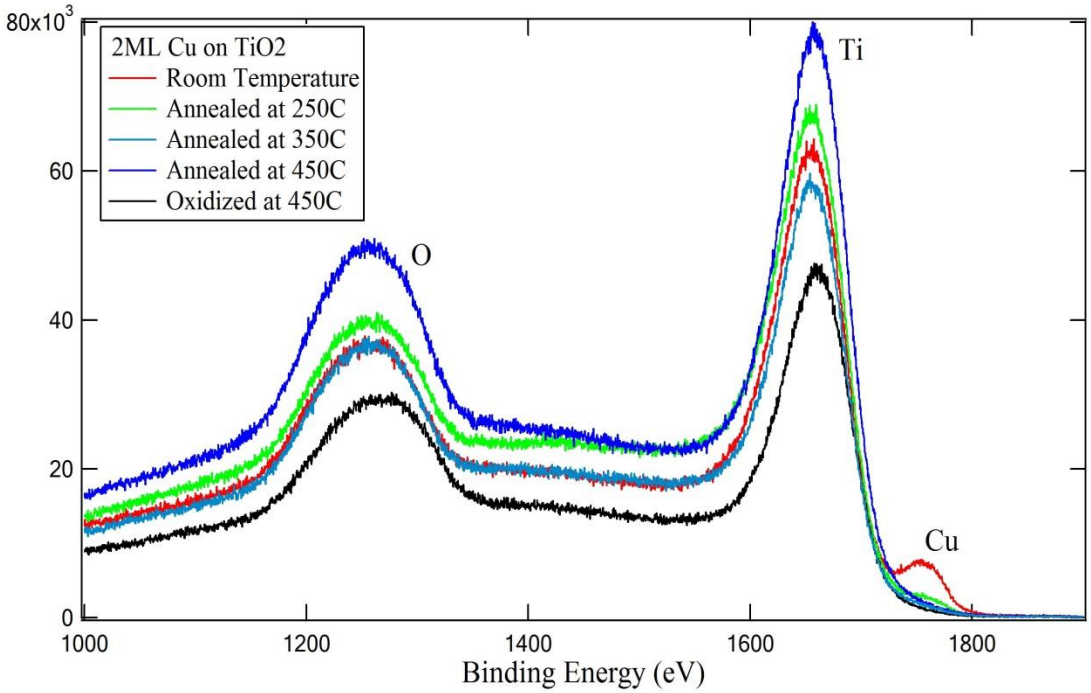

Figure 5.9 LEIS spectra of 2 ML Cu on TiO_2 under different pretreaments

Similar phenomena are also observed on 4 ML Cu on TiO_2 samples, as shown in Figure 5.10. The higher Cu coverage does not lead to a higher encapsualtion temperature, which could be ascribed to the high mobility of TiO_x species. It is important to mention that the average size of Cu clusters is significantly larger in oxidized samples than that in annealed samples. Thus it is possible to hypothesize that the sintering and/or ripenning of Cu clusters could still proceed underneath the TiO_x encapsulation layers, since the reduced TiO_x species are highly flexible at high temperature.

5.4.3 EELS

EELS is another surface-sensitive tool, which is employed to understand the electronic structure of the surface. If the encapsulation takes place, the removal of Cu signals should be also observed in EELS of high temperature samples. In Figure 5.11, three peaks are found: 0.3 eV (oxygen-deficiency defects), 2.4 eV (Cu), 5 eV (TiO_2). Clean TiO_2 has a

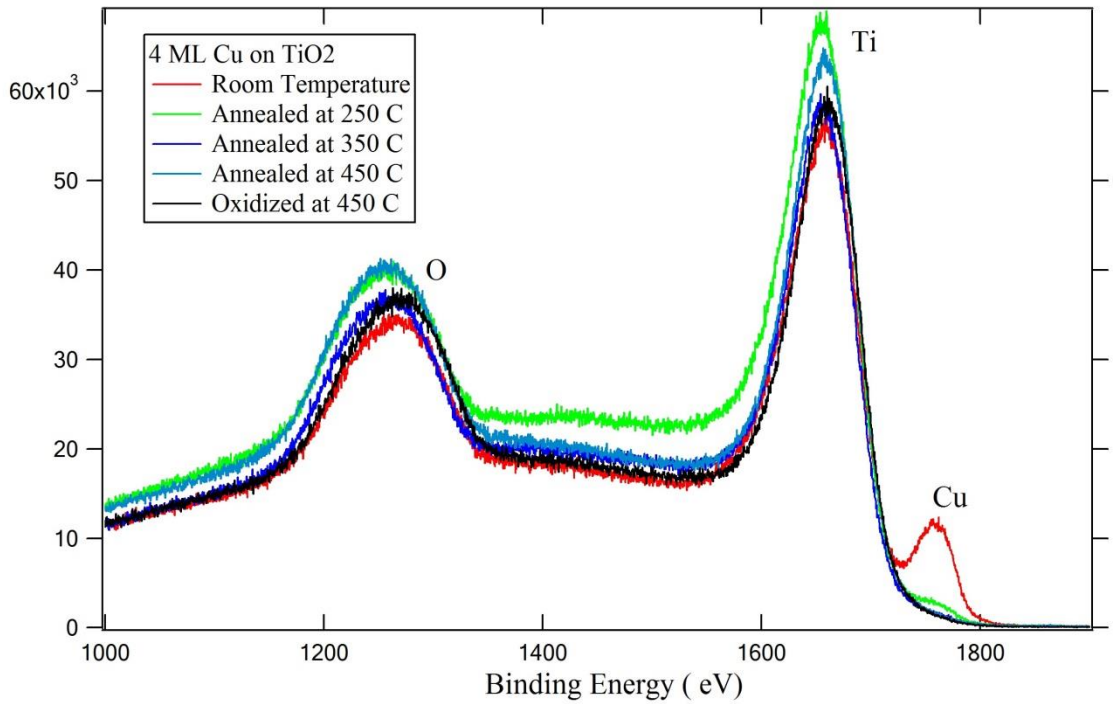

Figure 5.10 LEIS spectra of 4 ML Cu on TiO_2 under different pretreaments

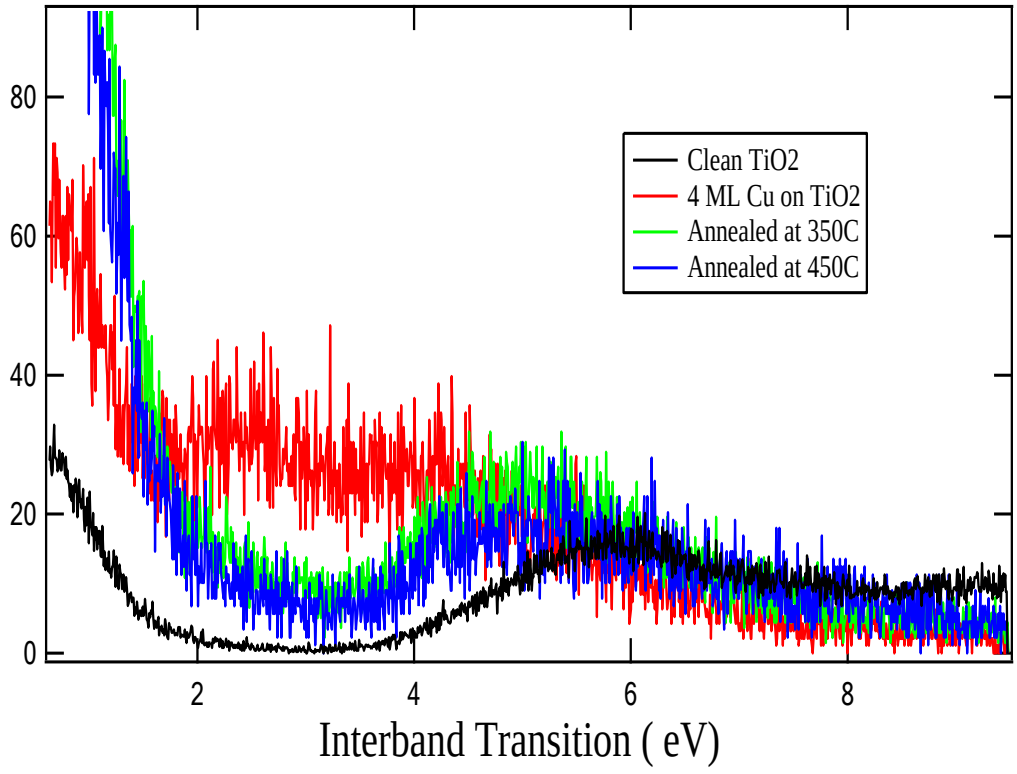

Figure 5.11 Interband transition of 4 ML Cu on TiO_2 (110) under different pretreatments

0.3 eV peak with relatively lower intensity, whereas the high temperature samples have a similar peak with much higher intensity, which indicates that these oxygen-deficiency defects are stable even under the oxidizing conditions. In both high temperature samples, the Cu peak signal is removed, due to the same TiO_x encapsulation. It is essential to note that the TiO_2 interband-transition peak in these high temperature samples, compared to clean TiO_2, has a red shift (1.1 eV), which results from the formation of new reduced TiO_2 (TiO_x) species on the surface through high temperature pretreatments.

5.4.4 UPS

Here we employ UPS to investigate the electronic structure of the prepared samples, in order to understand how the chemical states of surface vary with the experimental conditions. In Figure 5.12, it shows how the O and Cu peaks change with the different Cu coverages deposited at room temperature. It is clear that the metallic Cu peak (2.2 eV and 3.2 eV) is increasing as a function of Cu coverage, whereas the O peaks (3.8 and 5.2 eV) are decreasing. It is important to note that all of the above peaks do not have any shifts, which indicates that no charge transfer takes place between the Cu clusters and TiO_2 substrate.

The 8 ML Cu on TiO_2 sample exhibits a very high metallic Cu peak, while the original 3.8 eV peak shifts to 3.2 eV. At a high coverage, Cu thin films are formed on the surface rather than the Cu clusters, which could be responsible for the big shift in Cu peaks.

According to the above STM images, the surface structure of the annealed sample deviates from that of the oxidized sample, due to the introduction of O_2. As mentioned before, the atomic structral reconstruction could definitely bring changes to the electronic structure. It becomes important to investigate 1ML Cu on TiO_2 samples under the same

conditions in STM experiments. From Figure 5.13, the peaks of annealed sample are almost the same as those of the oxidized one. At these high temperature samples, two new peaks are shown at 0.8 eV and 2.2 eV, which are attributed to oxygen-deficiency defects and Cu_2O respectively. Moreover, the O peaks (5.6 eV and 4 eV) show significant red shifts, compared to the room temperature sample. These red shifts might result from the charge transfer bewteen Cu clusters and TiO_2 substrate. It needs to note that the interesting findings are the similar electronic structures between these two high temperature samples in the presence or absence of O_2. In the absence of O_2, the oxygen spillover from TiO_2 to the supported Cu atoms should be responsible for the formation of Cu_2O. In the oxidized sample, the intensity of these oxygen-deficiency-defects is not reduced, even under high temperature oxidation. As two type of dominant defects, the oxygen vacancies and Ti interstitials have proposed to be the cause of these oxygen-deficiency-defect states. In our case, the high thermal stability of these defects under the oxidizing conditions suggests that these oxygen-deficiency-defects are more likely Ti interstitials, rather than oxygen vacancies.

Another important issue that must be addressed is that the oxidation states of Cu on both samples are the same and no CuO could be found. The above finding could be explained by two possible effects: quantum size effect and confinement effect. Under high temperature pretreaments, the size dependence of the oxidation state is obvious, since metal clusters composed of small number of atoms exhibit different physical and chemical properties from the bulk materials, resulting in different chemical states for small clusters of few atoms in homogeneous catalysts. [147, 148, 149] Another important confinement effect, due to the interface SMSI, may favor the partial oxidation of the

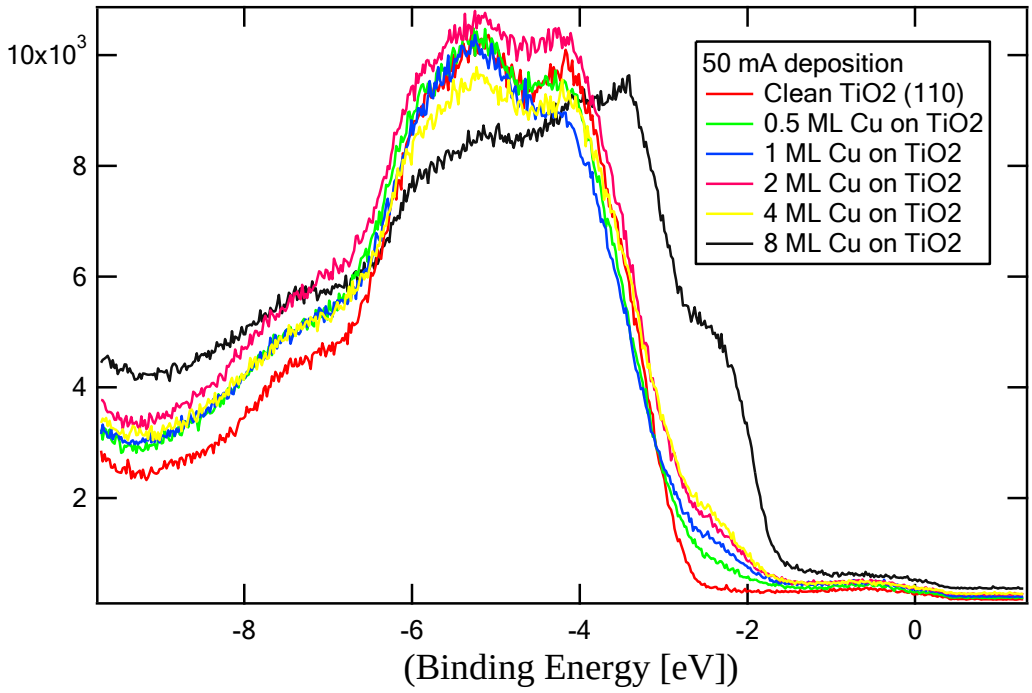

Figure 5.12 UPS data of different Cu coverage deposited on clean TiO_2 (110) surface

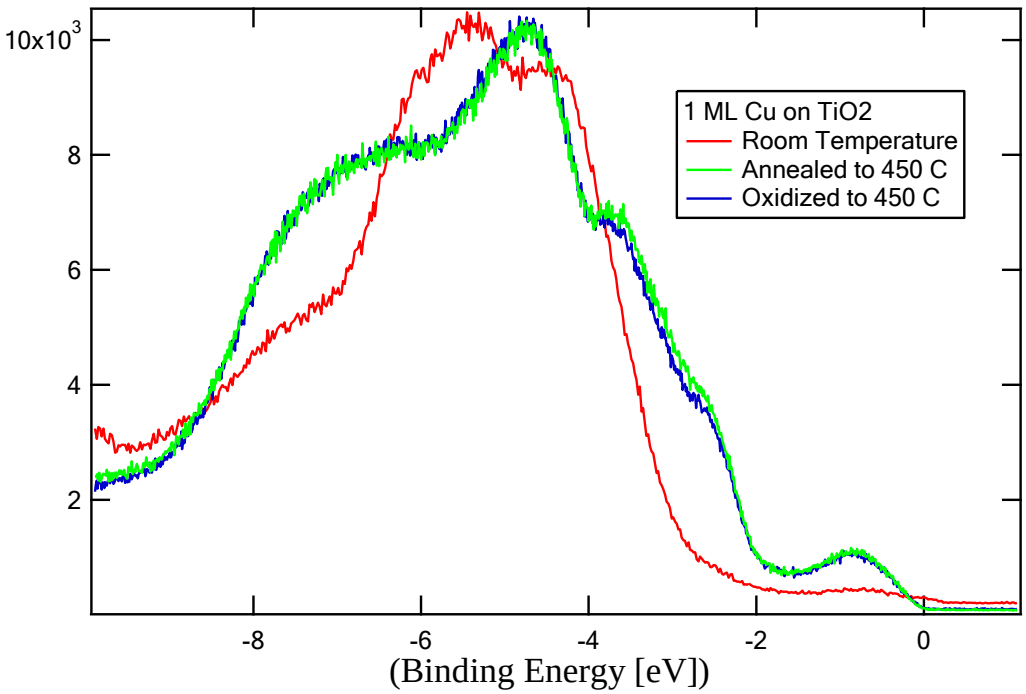

Figure 5.13 UPS data of 1 ML Cu on TiO_2 under different pretreatments

oxide supported metal nanoparticles and stabilize the particular states of surface defect. [146] The nature of confinement effect can be ascribed to the encapsulation behavior associated with the modification of electronic structure and therefore forbids the further oxidation of Cu_2O into CuO.

5.4.5 CO Adsorption From UPS

CO dosing was achieved by simply back filling the UHV chamber up to a maximum pressure of $2x10^{-7}$ Torr. The sample was cooled down to 90 k by liquid nitrogen and the low temperature was maintained during the whole experiment. As shown in Figure 5.14, the O peak (4 eV) has a small blue shift (0.17 eV) induced by the band bending after dosing CO and the increasing intensity of the peak at around 7 eV is associated with the CO dosage.

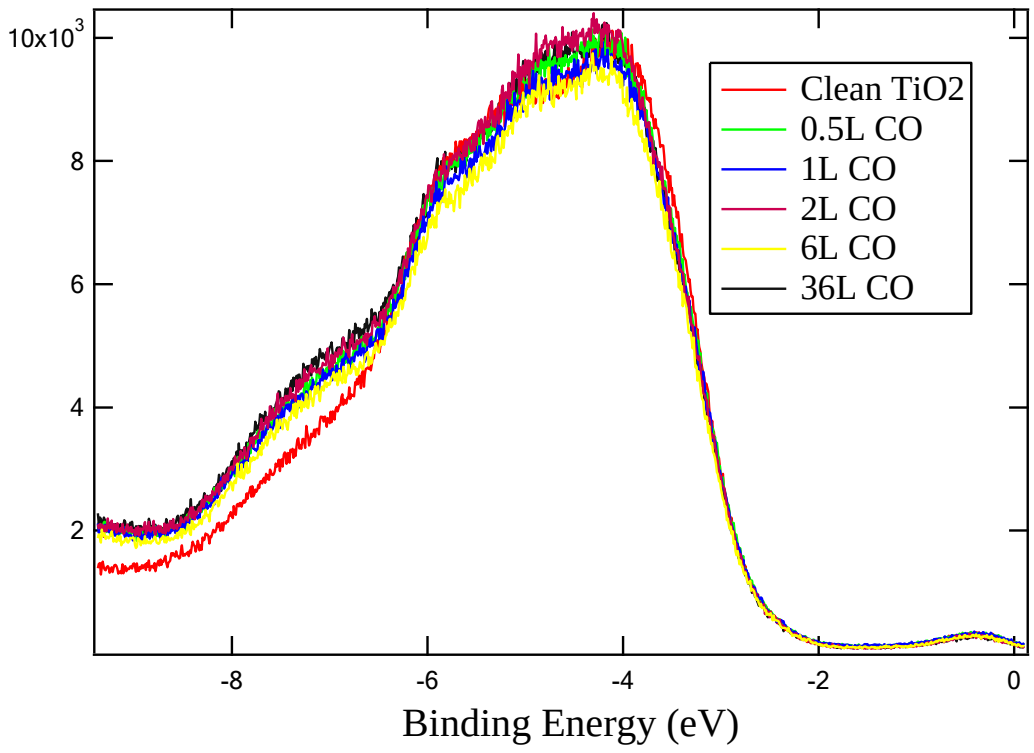

Figure 5.14 CO adsorption on clean TiO_2 at 90K

The encapsulation behavior has been previously reported to have a strong effect on the atomic and electronic structur, resulting in different catalytic performance. Here we employ CO as probe molecules to investigate the 1 ML and 8 ML CuO_x on TiO_2 samples in Figure 5.15 and Figure 5.16, respectively. It is evident that no CO adsorption could be observed in both samples even in a low dosage, as a consequence of the formation of reduced TiO_x encapsulation layers.

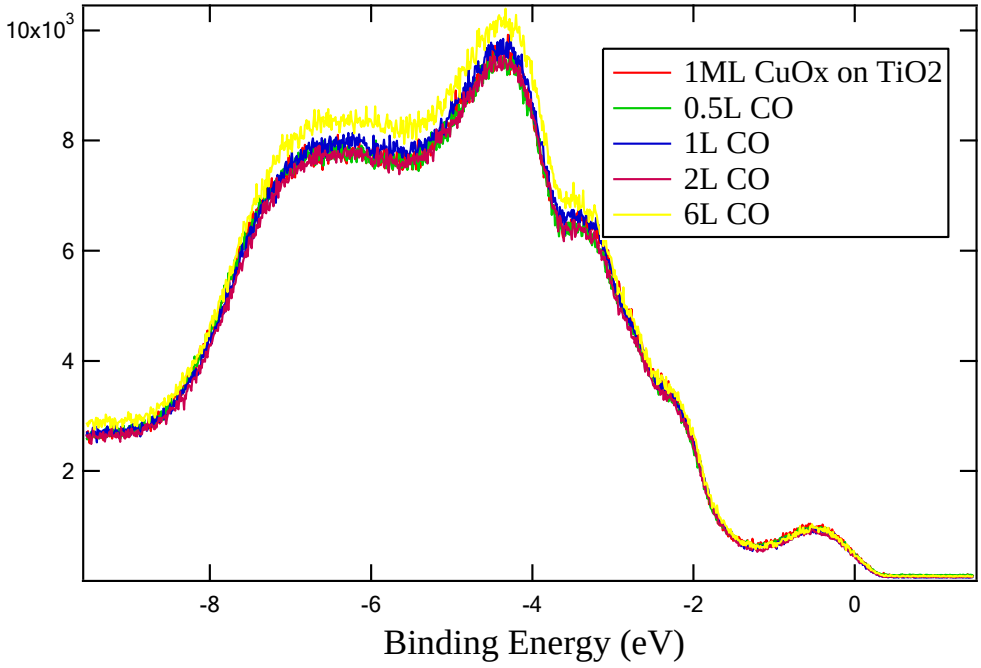

Figure 5.15 CO adsorption on oxidized 1 ML Cu on TiO_2 at 90K

Previous SMSI studies on TiO_2 supported metal nanoparticles have shown the strong metal-support interaction decreases the adsorption of hydrogen on the surface essentially to zero. [151] In Figure 5.17, the reduction of ratio of hydrogen atoms to metal atoms is associated with the increasing annealing temperature. However, these heterogeneous catalysts show superior activity and selectivity, which is highly relevent to their unusual chemisorption properties of CO and H_2. In our case, the interface SMSI has resulted in a

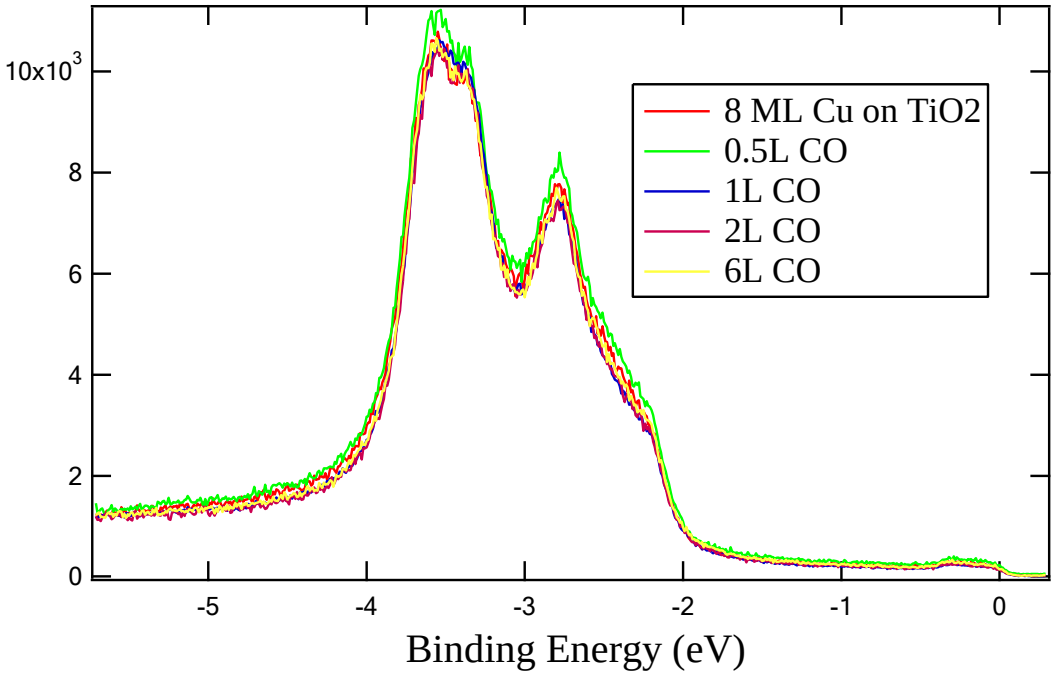

Figure 5.16 CO adsorption on oxidized 8 ML Cu on TiO_2 at 90K

decreased ability of CO adsorption, resulting from the modification of the surface structure. It is interesting to find out if this unusual CO chemisorption property lead to a superior catalytic reactivity.

Table 1. Hydrogen chemisorption on TiO_2-supported group VIII noble metals.

Metal (2 percent by weight)	Ratio of hydrogen atoms adsorbed to total metal atoms	
	Reduction at 200°C	Reduction at 500°C
Ruthenium	0.23	0.06
Rhodium	0.71	0.01
Palladium	0.93	0.05
Osmium	0.21	0.11
Iridium	1.60	0.00
Platinum	0.88	0.00

Figure 5.17 the hydrogen chemisorption on TiO2 supported noble metals. [151]

5.4.6 CO Oxidation

We now turn our attention to the CO oxidation, in order to testify the catalytic activity of the above samples. All the figures are shown in the yield of CO_2 and the slope stands for the reaction rate or formation rate of CO_2. As known, the atomic and electronic structure plays a key role in determining the catalytic reactivity. In situ reactions is expected to bridge the existing gap between surface science and catalysis. Here it is helpful to temporarily confine our attention to the highest reaction temperature.

In Figure 5.18, the CO_2 formation rate of 2ML Cu on TiO_2 is almost the same below 550K whereas the rates above 550K are much higher. The formation rate maintains constant when the substrate temperature is held fixed, even at high temperature range, which indicates high thermal stability of the sample. Different 2 ML Cu on TiO_2 samples are prepared in the presence and absence of O_2 at different annealing temperatures and then hold on to the CO oxidation. Their CO_2 formation rate were shown in Figure 5.19, Figure 5.20 and Figure 5.21, respectively. At 650K, a lower formation rate was found for 2 ML Cu on TiO_2 annealed at 500K, and a similar higher formation rate is found for the other two samples. One has to keep in mind that the significance of the above studies is to demonstrate that the modification of atomic and electronic structure is dependent on the interface metal-support interaction, which is associated with the substrate temperature. The lower formation rate at 550K is likely a consequence of the weaker interface interaction. It is not surprising to have a very similar formation rate for the other two samples annealed at 650K with/without oxygen, since both of them have very similar electronic and atomic structure.

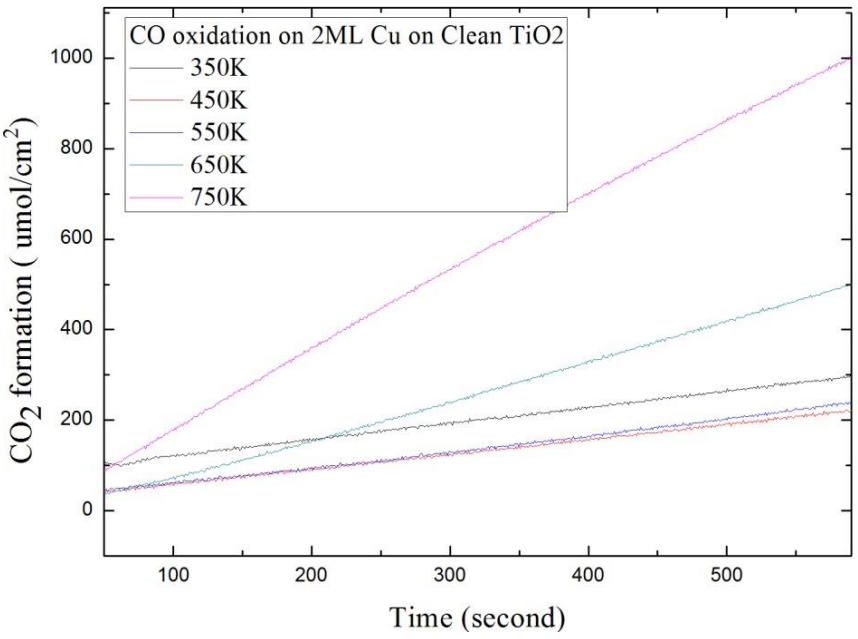

Figure 5.18 CO oxidation 2 ML Cu on TiO_2 under CO and O_2 mixture (O_2:CO=1:2)

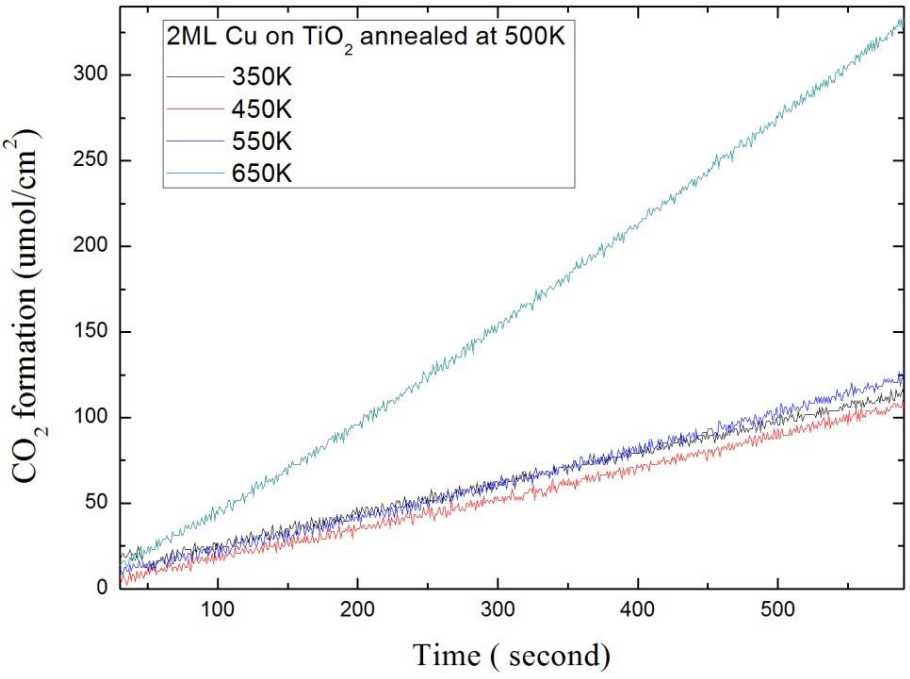

Figure 5.19 2 ML Cu on TiO_2 annealed at 500K under CO and O_2 mixture (O_2:CO=1:2)

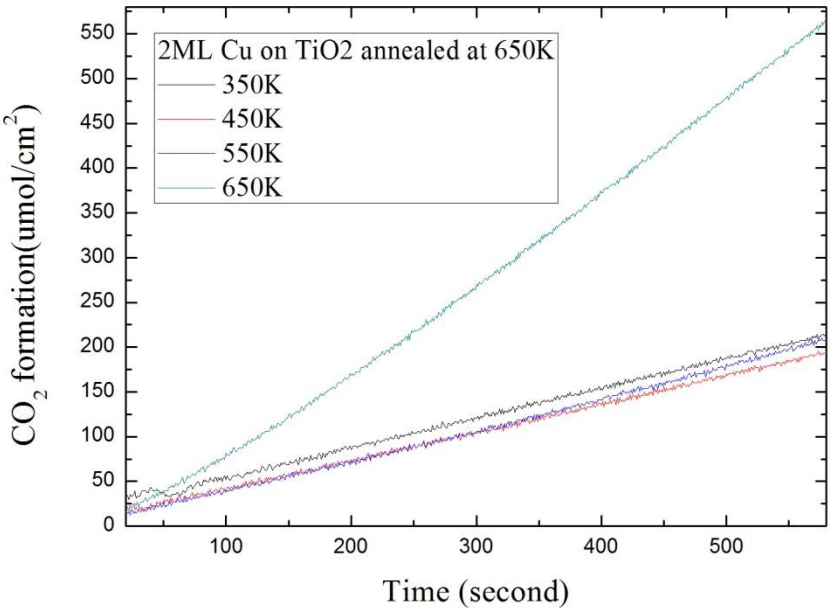

Figure 5.20 2 ML Cu on TiO_2 annealed at 650K under CO and O_2 mixture (O_2:CO=1:2)

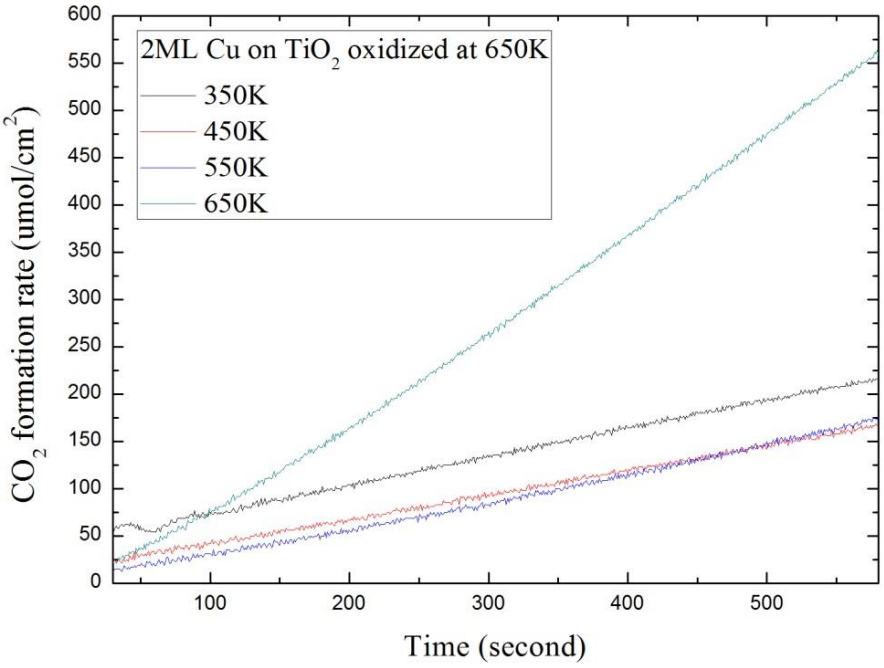

Figure 5.21 2 ML Cu on TiO_2 oxidized at 650 K under CO and O_2 mixture (O_2:CO=1:2)

At high substrate temperature, encapsulation of Cu clusters is induced by the diffusion of reduced TiO_x species. As the Cu clusters are trapped inside a TiO_x shell, the classical bifunctional mechanism can not be implicated here, since no Cu atoms are exposed to CO molecules. As shown in UPS, a high density of oxygen-deficiency defects are localized at the surface, especially at the ultra-thin TiO_x films. These defects are prefect active sites for dissociating O_2 molecules, since the O_2 dissociation is more facile at these low-coordinated Ti-O atoms than TiO_2 bulk. The high thermal stability of these defect states under the oxidizing conditions may be the cause for constant reaction rates during the CO oxidation experiments.

5.5 Summary

As potential photocatalysts, Cu on TiO_2 have shown a high thermal stability of the morphology and catalytic performance. The encapsulation behavior, as found in other TiO_2 supported metal nanoparticles, plays a decisive role in modifying the atomic and electronic structure of the surface. These encapsulation layers are self-limited to one to two layers thick, and helps to disperse the supported metal nanoparticles. The O spillover from the TiO_2 substrate to Cu nanoparticles should be responsible for the oxidation of Cu, even under high oxidizing conditions. It is also of importance to note that the substrate temperature is the key to controlling the strength of metal-oxide interaction, since the thermal energy is the driving force for TiO_x diffusion. These SMSI effects in the interface have led to different CO adsorption behavior and therefore altered the catalytic performance. Another significance of the above studies is to demonstrate the high thermal stabiliy of the defect states as well as catalytic performance, and the active sites should be the defect sites on the reduced TiO_x thin films.

Chapter 6: Summary

A mass of industrial catalysts of commercial importance are known to be comprised of metal nanoparticles and metal oxides, and these heterogeneous catalysts form the basis of modern chemical manufacturing. On these heterogeneous catalysts, the active sites are considered to directly catalyze the expected reactions and form the desired products. Therefore, it becomes urgent to understand the nature of these active sites, especially their chemical composition and atomic structure. Unfortunately, the complex interfacial interactions between the metals and the oxide supports make understanding the nature of these important active sites extremely challenging, since these interface interactions are highly sensitive to the environmental and reaction conditions. As a consequence, it becomes very hard to control the physical and chemical structure of the heterogeneous catalysts.

One possible promising approach to understanding active sites is using the combination of surface science and accurate theoretical calculations to provide deep insights into chemical composition and electronic structure of these active sites, which play a direct role on chemical and physical properties of the heterogeneous catalysts. These unique properties of heterogeneous catalysts arise from the interactions of their surfaces with the reactive environments and determine the surface dynamics and possible reaction paths on the active sites, which provides the fundament of catalytic reactions and opens new perspectives for the redesign of new catalytic materials.

In this dissertation, we have studied three oxide supported metal catalyst systems where the strong metal-support interaction is found to dominate their surface chemistry and adsorption behavior: Cu on ZnO, Au on ZnO, and Cu on TiO_2. In addition, we are

trying to demonstrate the atomic and electronic structure of the above prepared samples through the accurate surface investigations through surface-sensitive tools. The comprehensive studies help to answer the questions: how these metal atoms grow on the metal oxide surface? What are the kinetics and thermodynamics that control the growth of the metal atoms? How the physical and chemical properties of the deposited metal atoms are related to experiment conditions? How these unique properties determine the catalytic performance? All the experiments in our work are designed and analyzed to answer the above questions.

On the Cu on ZnO samples, the growth of Cu is in a manner of Volmer-Weber (VW) model, and the step edges are energetically favored for the growth of Cu clusters, which indicates the defects sites on step edges are adsorption sites for Cu adatoms. The Cu coverage has no significant effect on the formation of Cu clusters, and the mean cluster size is highly dependent on the experimental conditions, especially the substrate temperature. As found in original SMSI cases, the encapsulation of Cu clusters by ZnO support is induced by the high temperature pretreatments and associated with the charge transfer in the interface. The modified atomic and electronic structure has been observed to dramatically alter the catalytic performance from the CO_2 adsorption and CO oxidation experiments.

On the Au on ZnO samples, the initial growth of Au prefers a quasi-2D growth, and forms 3D clusters at higher coverage. That is because the Au-ZnO interaction is relatively stronger than Au-Au interaction at low coverage and is largely weakened at high coverage. Similar phenomena of Cu on ZnO samples take place to Au on ZnO samples, whereas a higher substrate temperature is required to induce the surface reconstruction. In

both Cu and Au on ZnO cases, the introduction of oxygen plays a significant role in lowering the diffusion barrier of ZnO dimers and therefore resulting in a higher encapsulation rate of metal nanoclusters, however the origin of this essential effect remains poorly understood. The fully encapsulated samples represent the best catalytic performance, where the metal clusters is isolated by the ZnO ultrathin films. It reveals that the ZnO ultrathin films are of crucial importance to carry out catalytic reactions and thus the CO oxidation reaction should proceed through a different catalytic reaction mechanism.

In order to understand the encapsulation behavior and the resulting abnormal catalytic performance, it becomes important to compare our ZnO based heterogeneous catalysts with the classical SMSI catalysts. According to previous studies, the formation of ultrathin oxide films on the supported metal nanoparticles is always complex and is highly dependent on the important surface and subsurface diffusion process. The high temperature and even reduction treatments are required to transfer the stoichiometric oxides into the reduced phases. That is because the metal and oxygen atoms/ions are known to have a higher mobility in the reduced oxide phases. [146] In contrast to the encapsulation behaviors on the other reducible oxides, ZnO encapsulation behavior has a strong preference of oxygen during the annealing treatment, which provides a strong indication that the diffusion of ZnO should proceed by a different mechanism.

In analogy with current models of the TiO_2 diffusion mechanism, it is difficult to reconcile why oxidation rather than reduction could improve the mobility of ZnO, if Zn ions and/or Zn interstitials are proposed to be responsible for the formation of ZnO encapsulation layers. [63, 84] Moreover, there is no direct evidence from our

measurements of XPS, UPS, and EELS that the alloy formation such as Zn-Cu, or the complex compound Zn_xCu_yO takes place after being annealed in UHV or oxygen. Besides the alloy formation, no large amount of point defects states such as O and/or Zn vacancies could be observed even in the near surface area. Therefore, it is believed that the ZnO encapsulation of Cu nanoclusters is likely a result of the surface or subsurface diffusion of ZnO dimers, or the atomic $(ZnO)_x$ clusters. From Dominik's calculation, formation energy of ZnO dimer vacancy is much lower than that of Zn vacancy or O vacancy, and could be the most favorable atomic defects in ZnO. [90] In other words, the ZnO dimers should have a much higher mobility or larger diffusion length than the Zn and O atoms/ions. In the encapsulation process, the oxidation treatment might have two important roles: (i) the removal of oxygen-deficiency defects states on the surface, which could greatly enhance the diffusion length of surface ZnO dimers; (ii) the transformation of the surface of metallic Cu clusters into partially oxidized CuO_x, which modifies the interfacial energy between metallic Cu and ZnO and the corresponding diffusion barriers over the nanoclusters. That explains why the ZnO encapsulation behavior has a strong preference of oxygen during annealing treatment.

Naturally, the geometric and electronic structure of the resulting ZnO encapsulation layers is governed by the Cu nanoclusters underneath. Upon completion of the ZnO encapsulation layer, the resulting crystallographic structure of the ZnO encapsulation layers differ from that of the bulk due to lattice mismatch and corresponding charge redistribution. The unique electronic/atomic structure of the ZnO overlayer self-limits further growth. As such, 3D cluster growth of ZnO on the Cu nanostructures is mitigated;

in accordance with the EELS, LEIS, and UPS data above, it is believed that encapsulating layer is best described as 1-2 bilayers ZnO on the Cu nanoclusters.

In systems such as Pt/TiO_2, or Pt/Fe_3O_4, it is known that the chemical composition of the encapsulation layers is relevant to the experimental conditions that produced it, controlling the resulting stoichiometry, determined by the oxidation state of the support, and the corresponding interface energy of the encapsulation layer. [29, 98, 121] In this context, ZnO is very different from other complex oxides (TiO_2, Fe_3O_4, CeO_2), which also form encapsulation layers, in that there are no known sub-oxide species. Because of stability of the ZnO species, the chemical composition of the encapsulation layer is resistant to either oxidation or (weak) reduction. This constant stoichiometric assertion is bolstered by our LEIS data, in which the ratio of Zn/O is always 1:1 in all of the samples that we studied.

Finally, for other SMSI systems, encapsulation of supported metal nanoparticles is generally characterized by a drastic attenuation of adsorption behavior. In contrast, our UPS data reveals that upon full ZnO encapsulation of the Cu nanoparticles, the adsorption of CO_2 is markedly higher than either Cu nanoparticles or clean ZnO $(10\bar{1}0)$ surface. In our case, the ZnO encapsulation layers are found to be negatively charged, due to the charge transfer from the Cu nanoclusters, and assumed to have perturbed crystallographic structure, in order to compensate the mismatch-induced stress in the interface. As a consequence, the adsorption of CO_2 is greatly enhanced on this unique ZnO encapsulating layer.

These ZnO ultrathin films have several advantages over the bulk ZnO: (1) low-coordinated atoms; (2) slightly negatively charged surface; (3) higher-thermal stability.

As shown in CO_2 adsorption experiments, these ZnO ultrathin films could donate much more electrons to form the covalent bonds with the adsorbed CO_2 molecules. That is why the oxidized samples have the highest CO oxidation rate, while the mean size of the supported metal clusters is much larger. It is evident that the above unique properties of ZnO ultrathin films have distinct effect on lowering reaction barrier, resulting in a higher reaction rate. The high-thermal stability of the special ZnO thin films solves another important problem: how these active sites survive under reaction conditions, in particular when dealing with oxidation reactions and the presence of a high oxygen partial pressure like realistic conditions.

On the Cu on TiO_2 samples, Cu forms 3D clusters and these Cu clusters remain stable even at relatively high temperature. Similar to Cu on ZnO, the Cu adatoms are located at the defect sites on the step edges. The encapsulation takes place at a lower temperature, and is not dramatically influenced by the Cu coverage. In contrast to the ZnO supported catalysts, the oxidation does not promote the encapsulation of Cu clusters by the TiO_x thin films, which is ascribed to the different chemical and physical properties of TiO_2. The electronic structure of the oxidized and annealed sample does not show any difference in both physical and chemical structure, which implies the encapsulation layers possess a very high thermal stability. This significant importance of this amazing finding is that the defect states could be preserved even under strong oxidizing conditions, which plays a key role in catalytic performance of the prepared samples. Thus it is not surprising to find a very stable reaction rate of CO oxidation on the above samples. In comparison with Cu on ZnO system, it clearly demonstrates how the different metal oxide supports affect the growth of metal nanoparticles and the formation of interface

energy, due to their different chemical and physical properties. As known, the driving force of encapsulation behavior is the interfacial charge redistribution and the mass transport in the interface. That is why the above two systems present different encapsulation behaviors, and the strong preference of oxidation in Cu on ZnO samples is still mystery. There is a need for further studies exploring the deep information of the interface.

The above pioneering work was motivated by numerous reports on the ultra-high selectivity at polycrystalline ZnO catalysts. In addition to the high selectivity of pure ZnO, an effective industrial Cu on ZnO methanol catalysts always require a high free ZnO surface area and an proper mixture of Cu and ZnO. The previous studies have demonstrated the decisive role of ZnO and assigned it to the puzzling support effect. However, the catalysts comprised of either Cu nanoparticles or polycrystalline Cu do not show any unique properties of methanol synthesis. So it is very likely that ZnO are working more than a simple support and the understanding of its unique role is required to form the basis of mechanism of methanol synthesis.

By taking full advantage of the synergy between the surface-science and catalysis communities, we redefine the geometric and electronic properties of ZnO supported catalysts, which is highly relevant to their catalytic performance. Due to its simplicity, CO oxidation is applied to elucidate the reaction mechanism and identify the active sites. By encapsulating nanoparticles in well-defined structure, a much higher reaction rate is obtained. In these encapsulated samples, no reactants (CO and O_2) could access to these metal nanoparticles and form new CO_2 molecules, which gives evidence to the fact that these ultra-thin oxide films play a decisive role in the exceptional catalytic activity of the

above heterogeneous catalysts. The above findings show the importance of the combination of Cu and ZnO and how the experimental conditions affect the formation of ZnO encapsulation layers. It could be helpful to explain why the combination of Cu and ZnO shows a much better catalytic performance than either Cu or ZnO, as called synergy effect.

The above studies of model catalysts form the solid basis of methanol synthesis from syngas, since the reactivity and selectivity of the catalysts are determined by the atomic and electronic structure of surface and/or near surface. In our experiments, the CO_2 adsorption and CO oxidation could be taken as the initial steps for CO_2 or CO hydrogenation into methanol. In order to achieve a complete understanding, the in-situ reaction of CO or CO_2 hydrogenation is highly recommended for future studies. The in-situ reaction could help us gain the information of intermedia products and understand the multi-process synthesis of methanol. Moreover, it is critical to define the active sites of fully encapsulated samples, and connect catalytic reactivity and selectivity to the nature of these catalytic sites.

The further CO_2 and CO adsorption in in-situ FTIR also provides a possible method to understand the reaction pathways and the dynamics of the individual reaction steps. The DFT calculation could help develop the systematic approaches to characterize the adsorption sites or active sites at atomic level, which provides us the essential understanding about how to direct the desired chemical reactions.

The atom-resolved STM could also be used to image the surface structure of the above prepared samples and the adsorption of CO or CO_2 on the surface could offer us detailed information of the individual adsorbed CO_2 molecules. It becomes possible to find the

atomic structure of active sites on these ultra-thin ZnO films and how the interfacial charge transfer modifies the chemical bonds of the adsorbates.

More studies should be done on Au on ZnO, since gold has no stable oxide states. The CO and CO_2 adsorption by EELS and UPS could help us understand the unique properties of ultra-thin ZnO films. Besides the similarity in reactivity of CO oxidation, it is also possible to hypothesize that the adsorption energy on the oxidized Au on ZnO should be close to that on the oxidized Cu on ZnO, since the adsorption sites should be located at the ultra-thin ZnO films.

The above approaches make it possible to efficiently adapt these advances based on the model catalyst study into useful applications to industry. Additionally, the advent of nanoscience and nanotechnology also provides the ability to control the surface structure by investigating and optimizing a broad range of catalytic processes. We wish that our efforts in surface science could lead to the design of new heterogeneous catalysts in methanol industry and avoid the empirical tests in trial-and-error experiments.

References

[1] G. Ertl, H. KnÖzinger, F. Schüth, and J. Weitkamp (eds.), *Handbook of Heterogeneous Catalysis* (Wiley-VCH VerlagGmbH & Co. KGaA, Weinheim, 2008).

[2] G. A. Somorjai, J. Y. Park, *Catal. Lett.* 2007, 87, 115.

[3] K. Hayek, M. Fuchs, B. Klotzer, W. Reichl, G. Rupprechter, *Top. Catal.* 2000, 13, 55.

[4] G. A.Somorjai, Y. M. Li, 2010. *Introduction to Surface Chemistry and Catalysis*. New York: Wiley & Sons.771 pp.

[5] D. W. Goodman, *Chem. Rev.* 1995, 36, 523.

[6] F. Zaera, *J. Phys. Chem. B* 106 (2002) 4043.

[7] Gabor A. Somorjai, Jeong Y. Park, *Angew. Chem. Int. Ed.* 2008, 47, 9212-9228.

[8] A. S. K. Hashmi, G. J. Hutchings, *Angew. Chem., Int. Ed.* 2006, 45, 7896–7936.

[9] M. S. Chen, D. W. Goodman, *Science* 2004, 306, 252-255.

[10] N. Nilius, M. V. Ganduglia-Pirovano, Br_azdova, V. Kulawik M., Sauer J., H. J. Freund, *Phys. Rev. Lett.* 2008, 100, 096802-1-4.

[11] M. Sterrer, T. Risse, M. Heyde, H.-P. Rust, H.-J. Freund, *Phys. Rev. Lett.* 2007, 98, 206103-1-4.

[12] X. Shao, N. Nilius, H.-J. Freund, *Phys. Rev. B* 2012, 85, 115444-1-8.

[13] J.-H. Fischer-Wolfarth, J. A. Farmer, J. M. Flores-Camacho, A. Genest, I. V. Yudanov, N. Rosch, C. T. Campbell, S. Schauermann, H.-J. Freund, *Phys. Rev. B* 2010, 81, 241416-1–241416-4.

[14] S. Schauermann, N. Nilius, S. Shaikhutdinov, H.-J. Freund, *Acc. Chem. Res.* 2012, DOI: 10.1021/ar300225s.

[15] S. A. Nepijko, M. Klimenkov, M. Adelt, H. Kuhlenbeck, R. Schlogl, H.-J. Freund, *Langmuir* 1999, 15, 5309–5313.

[16] S. J. Tauster, *Acc. Chem. Res.* 1987, 20, 389–394.

[17] S. J. Tauster, S. C. Fung, *J. Catal.* 1978, 55, 29.

[18] Y.-N. Sun, L. Giordano, J. Goniakowski, M. Lewandowski, Z.-H. Qin, C. Noguera, S. Shaikhutdinov, G. Pacchioni, H.-J. Freund, *Angew. Chem., Int. Ed.* 2010, 49, 4418–4421.

[19] O. Dulub, W. Hebenstreit, U. Diebold, *Phys. Rev. Lett.* 2000, 84, 3646–3649.

[20] M. Bowker, P. Stone, P. Morrall, R. Smith, R. Bennett, N. Perkins, R. Kvon, C. Pang, E. Fourre, M. Hall, *J. Catal.* 2005, 234, 172–181.

[21] Z. H. Qin, M. Lewandowski, Y. N. Sun, S. Shaikhutdinov, H. J. Freund, *J. Phys.: Condens. Matter* 2009, 21, 134019-1–134019-6.

[22] M. Ritter, W. Ranke, W. Weiss, *Phys. Rev. B*, 1998, 57, 7240–7251.

[23] Y. N. Sun, Z. H. Qin, M. Lewandowski, E. Carrasco, M. Sterrer, S. Shaikhutdinov, H. J. Freund, *J. Catal.* 2009, 266, 359–368.

[24] H.-J. Freund, *Surf. Sci.* 2007, 60, 11438.

[25] H.-J. Freund, *Surf. Sci.* 2002, 500, 271.

[26] C. T. Campbell, *Phys. Rev. Lett.* 2006, 96, 066106.

[27] S. Surnev, M.G. Ramsey, F.P. Netzer, Progr. *Surf. Sci.* 2003, 73, 117.

[28] E. Lundgren, G. Kresse, C. Klein, M. Borg, J.N. Andersen, M. De Santis, Y. Gauthier, C. Konvicka, M. Schmid, P. Varga, *Phys. Rev. Lett.* 2002, 88, 246103.

[29]N. Nilius, *Surface Science Reports* 2009, 64, 595-659.

[30] L. Giordano, M. Baistrocchi, G. Pacchioni, *Phys. Rev. B* 2005, 72,115403.

[31] L. Giordano, U. Martinez, S. Sicolo, G. Pacchioni, *J. Chem. Phys.* 2007, 127, 144713.

[32] I. Rashba, M. D. Sturge (Eds.), Excitons, North-Holland Publ., Amsterdam, 1982.

[33] L. Giordano, G. Pacchioni, *Phys. Chem. Chem. Phys.* 2006, 8, 3335.

[34] G. Pacchioni, L. Giordano, M. Baistrocchi, *Phys. Rev. Lett.* 2005, 94, 226104.

[35] LK 2000 Spectrometer manual.

[36] J. R. Gomes, F. Illas, N. C. Hernandez, A. Marquez, J .F. Sanz, *Phys. Rev. B* 2002, 65, 125414.

[37] M. Walter, P. Frondelius, K. Honkala, H. Hakkinen, *Phys. Rev. Lett.* 2007, 99, 96102.

[38] D. Ricci, A. Bongiorno, G. Pacchioni, U. Landman, *Phys. Rev. Lett.* 2006, 97, 036106.

[39]Fei Wang, PhD dissertation, Louisiana State University, 2011.

[40]G. Natta, *Synthesis of Methanol in Catalysis*, vol. 3, Reinhold Publishing Corporation, New York, 1955.

[41] Kostelitz, O., Hensinger,G., *Chimie & industrie*, 1939, 40, 757.
[42] Melanie Kurtz, Jennifer Strunk, *et al.*, *Angew. Chem. Int. ed.* 2005, 44, 2790-2794.

[43] L. C. Grabow, M. Mavrikakis, *ACS catal.* 2011, 1, 365-384.

[44] H. Lüth, Solid Surfaces, Interfaces and Thin Films, (2001).

[45] Manuel P. Soriaga, Xiaole Chen, Ding Li, John L. Stickney, High Resolurion *Electron Energ- Loss Spectroscopy*, Wiley, 2008.

[46] H. Hertz, *Ann. Phys.* 1887, 17, 983.

[47] Andrea Damascelli, *Physica Scripta* 2004, **T109**, 61-74 .

[48] J. B. Hudson, *Surface Science: An introduction*, (Butterworth-Heinemann, Stoneham, 1992).

[49] H. Ibach, D. L. Mills, *Electron Energy Loss Spectroscopy and surface vibration*, (Academic, New York, 1982).

[50] H. H. Brongersma, M. Draxler, M. de Ridder, P. Bauer, *Surface Science Reports* 2007, 62, 63-109.

[51] S. N. Mikhailov, R. J. M. Elfrink, J.-P. Jacobs, L. C. A. van den Oetelaar, P. J. Scanlon, H. H. Brongersma, *Nucl. Instrum. Methods Phys. Res. Sect. B* 1994, 93, 149.

[52] H. H. Brongersma, *et al.*, *Nucl. Instrum. Methods Phys. Res. Sect. B* 1998, 142, 77.

[53] M. Schmid,http://www.iap.tuwien.ac.at/www/surface/stm_gallery/stm_schematic, (2005).

[54] I. T. Drapak, *Semiconductors* vol.2, pp.624-625, 1968.

[55] Michael H. Huang, Samuel Mao, *et al*., *Science* 292 (5523) 1897-1899.

[56] P. X. Gao, *et al.*, *Science* 2005, 309, 1700.

[57] Z. L. Wang, *Annu. Rev. Phys. Chem.* 2004**,** 55, 159.

[58] W. L. Hughes, Z. L. Wang, *J. Am. Chem. Soc.* 2004**,** 126, 6703.

[59] G. S. Devi, V. B. Subrahmanyam, S. C. Gadkari, S. K. Gupta, *Analytica Chimica Acta*, vol. 568, pp. 41–46, 2006.

[60] H. Gong, J. Q. Hu, J. H. Wang, C. H. Ong, F. R. Zhu, *Sens. Actuators B, Chem.*, vol. 115, pp. 247–251, 2006.

[61] X. H. Wang, Y. F. Ding, J. Zhang, Z. Q. Zhu, S. Z. You, S. Q. Chen, J. Z. Zhu, *Sens. Actuators B, Chem.*, vol. 115, pp. 421–427, 2006.

[62] T. F. Xue, J. F. Hu, H. W. Qin, Y. Zhou, K. An, L. Zhang, T. Han, Y. X. Li, *Rare Metal Mater. Eng.*, vol. 33, pp. 1006–1008, 2004.

[63] M. A. Henderson, *Surface Science*, 1999, 419, 174–187.

[64]Zhong Lin Wang, Jinhui Song, *Science* 2006, 312, 242.

[65] Bedja, I., *et al.*, *Langmuir* 1997, 13, 2398.

[66] Keis, K., *et al.*, *J. Photochem. Photobiol. A* 2002, 148, 57.

[67] Keis, K., *et al.*, *J. Electrochem. Soc.* 2001, 148, A149.

[68] C. B. Duke, A. R. Lubinsky, S. C. Chang, B. W. Lee, P. Mark, *Phys. Rev. B* 1997, 15, 4865.

[69] C. B. Duke, R. J. Meyer, A. Paton, P. Mark, *Phys. Rev. B* 1978, 18, 4225.

[70] K. Ozawa, K. Sawada, Y. Shirotori, K. Edamoto, M. Nakatake, *Phys. Rev. B* 2003, 68, 125417.

[71] W. E. Carlos, E. R. Glaser, D. C. Look, *Physica B* 2001, 976, 308–310.

[72] A. Janotti, C. G. Van de Walle, *Phys. Rev. B* 2007, 76, 165202.

[73] L. S. Vlasenko, G. D. Watkins, *Phys. Rev. B* 2005, 72, 035203.

[74] P. Erhart, K. Albe, *Appl. Phys. Lett.* 2006, 88, 201918.

[75] F. A. Selim, M. H. Weber, D. Solodovnikov, K. G. Lynn, *Phys. Rev. Lett.* 2007, 99, 085502.

[76] F. Oba, S. R. Nishitani, S. Isotani, H. Adachi, I. Tanaka, *J. Appl. Phys.* 2001, 90, 824.

[77] T. R. Paudel, W. R. L. Lambrecht, *Phys. Rev. B* 2008, 77, 205202.

[78] P. Erhart, A. Klein, K. Albe, *Phys. Rev. B* 2005, 72, 085213.

[79] S. Vlasenko, G. D. Watkins, *Phys. Rev. B* 2005, 71, 125210.

[80] S. M. Evans, N. C. Giles, L. E. Halliburton, L. A. Kappers, *J. Appl. Phys.* 2008, 103, 043710.

[81] K. Vanheusden, W. L. Warren, C. H. Seager, D. R. Tallant, J. A. Voigt, B. E. Gnade, *J. Appl. Phys.* 1996, 79, 7983.

[82] Y. W. Heo, D. P. Norton, S. J. Pearton, *J. Appl. Phys.* 2005, 98, 073502.

[83] J. Carrasco, N. Lopez, F. Illas, *Phys. Rev. Lett.* 2004, 93, 225502.

[84] J. He, R. K. Behera, M. W. Finnis, X. Li, E. C. Dickey, S. R. Phillpot, S. B. Sinnot, *Acta Mater.*, 2007, 55, 4325–4337.

[85] T. Moe Borseth, F. Tuomisto, J. S. Christensen, W. Skorupa, E. V. Monakhow, B. G. Svensson, A. Yu. Kuznetsov, *Phys. Rev. B* 2006, 74, 161202.

[86] L. J. Brillson, H. L. Mosbacker, D. L. Doutt, Y. Dong, Z. Q. Fang, D. C. Look, G. Cantwell, J. Zhang, J. J. Song, *Superlattices and Microstructures* 2009, 45, 206-213.

[87] Lukas Schmidt-Mende, Judith L. MacManus-Driscoll, *Materials Today* 10 2007, 5, 40-48.

[88] T. A. Merz, D. R. Doutt, T. Bolton, Y. Dong, L. J. Brillson, *Surf. Sci.* 2011, 605, 20-23.

[89] Y. Dong, F. Tuomisto, B. G. Svensson, A. Yu. Kuznetsov, L. J. Brillson, *Phys. Rev. B* 81(2010) 081201.

[90] Roman Kovacik, Bernd Meyer, Dominik Marx, *Angew.Chem. Int. Ed.* 2007, 46, 4894-4897.

[91] V. Bhosle, A. Tiwari, J. Narayan, *Appl. Phys. Lett.* 2006, 88, 032106.

[92] Oura K.; V. G. Lifshits, A. A. Saranin, A. V. Zotov, M. Katayama, *surface science: An Introduction. Berlin:* 2003, Springer ISBN 3-540-00545-5.

[93] Ilka Hegemann, *J. Comput. Chem.* 2008, 29: 2302–2310.

[94] Zhenyu Zhang, *et al.*, *Science* 1997, 276, 377.

[95] Fenglin Liao, Yaqun Huang, Junwei Ge, Weiran Zheng, Karaked Tedsree, Paul Collier, Xinlin Hong, Shik C. Tsang, *Angew. Chem.* 2011, 123, 2210-2213.

[96] Martin Kroll, Thomas Lober, Vadim Schott, Christof Woll, Ulrich Kohler, *Phys. Chem. Chem.Phys.* 2012, 14, 1654-1659.

[97] Tauster S. J., Fung S. C., Garten R. L., *J. Am. Chem. Soc.* 1978, 100,170.

[98] Z.-H. Qin, M. Lewandoski, Y.-N. Sun, S. Shaikhutdinov, H.-J. Freund, *J. Phys. Chem. C*, 2008, 112, 10209-10213.

[99] J. Y. Liu, *chemcatchem* 2011, 3, 934.

[100] Wu Q-H, Fortunelli A, Granozzi G., *Int. Rev. Phys. Chem.*, 2009, 28,571.

[101] Gui-Yang, Huang, Chong-Yu Wang, Jian-Tao Wang, *J. Appl. Phys.* 2009, 105, 073504.

[102] A. Wander, N. M. Harrison, *Surf. Sci.* 2000, 457, L342.

[103] H. Sakurai, M. Haruta, *Appl. Catal. A* 1995, 127, 93.

[104] H. Sakurai, S. Tsubota, M. Haruta, *Appl. Catal. A* 1993, 102, 125.

[105] M. Haruta, *CATTECH* 2002, 6, 102.

[106] G. C. Bond, C. Louis, D. T. Thompson, *Catalysis by Gold—Catalytic Science Series*, vol.6, Imperial College Press, 2006.

[107] H. Sakurai, T. Akita, S. Tsubota, M. Kiuchi, M. Haruta, *Appl. Catal. A: Gen.* 2005, 91, 179.

[108] Sang Hoon Joo, Jeong Young Park, *et al. Nature materials* 2009, 8, 126-131.

[109] A. Wolf, S. Schüth, *Appl. Catal. A: Gen.* 2002, 226, 1.

[110] M. Haruta, S. Tsubota, T. Kobayashi, H. Kageyama, M. J. Genet, and B. Delmon, *J. Catal*. 1993, 144, 175.

[111] S. D. Lin, M. Bollinger, M. A. Vannice, *Catal. Lett*. 1993, 17, 245.

[112] M. Haruta, *Catal. Today* 1997, *36*, 153.

[113] Y. Martynova, B.-H. Liu, *et al.*, *Journal of Catalysis* 2013, 301, 227-232.

[114] Bas L. M. Hendriksen, Marcelo D. Ackermann, Richard Van Rijn, *et al.*, *Natural Chemistry* 2010, 2, 730-734.

[115] R. Burch, R. J. Chappell, S. E. Golunski, *J. Chem. Soc. Farady Trans.* 1989, 85, 3569.

[116] Y. Kanai, T. Watanabe, T. Fujitani, T. Uchijima, J. Nakamura, *Cata. Today* 1996, 28, 223.

[117] J. C. Forst, *Nature* 1988, 334, 577.

[118] U. Diebold, M. Li, O. Dulub, E. L. D. Hebenstreit, W. Hebenstreit, *Surf. Rev. Lett.* 2000, 613, 5-6.

[119] J. Sasaki, N. L. Peterson, K. Hoshino, *J. Phys. Chem. Solids* 1985, 46, 1267.

[120] H. B. Huntington, G. A. Sullivan, *Phys. Rev. Lett.* 1965, 14, 177.

[121] U. Diebold, *Surface Science Reports* 2003, 48, 53-229.

[122] P. W. Tasker, *J. Phys. C* 1979, 12, 4977.

[123] Simon Bonanni, Kamel Ait-Mansour, Harald Brune, Wolfgang Harbich, *ACS. Catal.* 2011, 1, 385-389
[124] Brian O'Regan, Michael Gratzel, *Nature* 1999,353, 737-740.

[125] F. Boccuzzi, A. Chiorino, G. Martra, M. Gargano, N. Ravasio, B. Carrozzini, *J. Catal.* 1997, 165, 129-139.

[126] S. Fischer, A. W. Munz, K. D. Schierbaum, W. Gopel, *Surf. Sci.* 1995, 337, 17.

[127] U. Diebold, J. Lehman, T. Mahmoud, M. Kuhn, G. Leonardelli, W. Hebenstreit, M. Schmid, P. Varga, *Surf. Sci.* 1998, 411, 137.

[128] H. Onishi, Y. Iwasawa, *Surf. Sci.* 1994, 313, L 783.

[129] L. Q. Wang, D. R. Baer, M. H. Engelhard, *Surf. Sci.* 1994, 320, 295.

[130] Anthoula C. Papageorgiou, Nikolaos S. Beglitis, Chi L. Pang, Gilberto Teobaldi, Gregory Cabailh, Qiao Chen, Andrew J. Fisher, Werner A. Hofer, Geoff Thornton, *PNAS*, 2010, 107, 2391-2396.

[131] N. Bityurin, A. I. Kuznetsov, and A. Kanaev, *Applied Surface Science*, 2005, 248, 86–90.

[132] V. E. Henrich and R. L. Kurtz, *Phys. Rev. B* 1981, 12, 6280–6287.

[133] Y. Li, X. Li, J. Li, and J. Yin, *Materials Letters* 2005, 59, 2659–2663.

[134] H. Liu, H. T. Ma, X. Z. Li, M. wu, X. H. Bao, *Chemosphere*, 2003, 50, 39-46.

[135] Ming Kong, Yuanzhi Li, Xiong Chen, Tingting Tian, Pengfei Fang, Feng Zheng, Xiujian Zhao, *J. Am. Chem. Soc.* 2011, 133, 16414-16417.

[136] A. Gervasini, M. Manzoli, G. Martra, A. Ponti, N. Ravasio, L. Sordelli, F. Zaccheria, *J. Phys. Chem. B* 2006, 110, 7851−7861.

[137] Y. Liu, T. Hayakawa, K. Suzuki, S. Hamakawa, T. Tsunoda, T. Ishii, M. Kumahai, *Appl. Catal. A* 2002, 223, 137−145.

[138] F. Amano, S. Suzuki, T. Yamamoto, T. Tanaka, *Appl. Catal., B* 2006, 64, 282−289.

[139] A. M. Arias, R. Cataluña, J. C. Conesa, J. Soria, *J. Phys. Chem. B* 1998, 102, 809−817.

[140] Slamet, Nasution, H. W., Purnama, E., Kosela, S., Gunlazuardi, *J. Catal. Commun.* 2005, 6 (5), 313−319.

[141] S. Y. Qin, F. Xin, Y. D. Liu, X. H. Yin, W. Ma, *J. Colloid Interface Sci.* 2011, 356 (1), 257−261.

[142] L. Liu, C. Zhao, Y. Li, *J. Phys. Chem. C* 2012, 116, 7904−7912.

[143] Ying Li, Wei-Ning Wang, Zili Zhan, Myung-Heui Woo, Chang-Yu Wu, Pratim Biswas, *Applied Catalysis B: Environmental* 2010, 100, 386-392.

[144] Dong Liu, Yolanda Fernandez, Oluwafunmilola Ola, *et al., Catalysis Communications* 2012, 25, 78-82.

[145] D. A. Chen, M. C. Bartelt, R. Q. Hwang, K. F. McCarty, *Surf. Sci.* 2000, 450, 78.

[146] Qiang Fu, Wei-Xue Li, Yunxi Yao, *et al. Science* 2010, 328, 1141.

[147] M. D. Ackermann, T. M. Pedersen, B. L. M. Hendriksen, O.Robach, S. C. Bobaru, I. Popa, C. Quiros, H. Kim, B. Hammer, S. Ferrer, J.W. M. Frenken, *Phys. Rev. Lett.* 2005, 95, 255505.

[148] M. S. Chen, Y. Cal, Z. Yan, K. K. Gath, S. Axnanda, D. W.Goodman, *Surf. Sci.* 2007, 601, 5326.

[149] H. Gabasch, A. Knop-Gericke, R. Schlogl, M. Borasio, C.Weilach, G. Rupprechter, S. Penner, B. Jenewein, K. Hayek, B.Klotzer, Phys. Chem. Chem. Phys. 2007, 9, 533.

[150] H. A. van der Vegt, W. J. Huisman, P. B. Howes, T. S. Turner, E. Vlieg, *Surf. Sci.* 1996, 365, 205-211.

[151] S. J. Tauster, S. C. Fung, R. T. K. Baker, J. A. Horsley, *Science* 1981, 211,4487.

Appendix: ALD of ZnO on Cu-nanoclusters for methanol synthesis

Abstract

The properties of ALD-grown ZnO thin films on Cu clusters supported on ZnO($10\bar{1}0$) have been studied with scanning tunneling and scanning electron microscopy (STM, SEM) in combination with angle-resolved x-ray photoelectron spectroscopy. Deposition at room temperature of two monolayers of Cu on ZnO($10\bar{1}0$) results in metallic Cu^0 clusters ~8 nm wide by 1.4 nm high. Higher coverages of 15 ML result in a similar morphology, with slightly larger cluster sizes. Following air-exposure and ALD-growth of 2 cycles of ZnO, the Cu exhibits Cu^+ species characteristic of Cu_2O and the thin ZnO coating is hydroxylated. Electrochemical studies of ALD ZnO coatings on Cu suggest that they are more active for CO_2 reduction.

I. Introduction

Catalysts consisting of Cu supported on ZnO have been widely used in a variety of hydrogenation activities, especially methanol synthesis, for the past several decades[1-5]. Cu on ZnO($10\bar{1}0$) has previously been studied with STM[6] and valence band photoemission[7], and they indicate that Cu grows almost exclusively as 3D clusters even at very low coverage, and that the clusters are positively charged because of cluster-substrate interactions. Other work with Cu/ZnO catalysts suggests that Cu-Zn surface alloys may be a catalytically active species for methanol synthesis[2], with a Zn/Cu(111) model catalyst showing high activity for methanol synthesis from CO_2, and model Cu/ZnO catalysts showing Cu-Zn alloy formation after high-temperature reduction of the ZnO substrate. To date, there are few core level spectroscopy studies of Cu clusters on

ZnO($10\bar{1}0$) that would verify the proposed Cu-Zn alloying in the as-deposited clusters, or that would explain the reported charging effects. Recently Behrens *et al* have proposed a model for the active site for methanol synthesis on Cu/ZnO/Al_2O_3 catalysts that attributes the catalytic activity to steps at the Cu surface and the presence of Zn substituted into the Cu at the step sites, thus leading to partial coverage of the Cu with ZnO_x[8]. Kroll *et al* have also studied the morphology of metal-organic chemical vapor deposition (MOCVD) grown Cu on ZnO($10\bar{1}0$) with STM and X-ray photoelectron spectroscopy (XPS), finding Cu diffusion into the ZnO bulk after annealing high coverages of Cu (7 ML and higher), but they find no oxidation of the deposited Cu[9].

In the context of these Cu/ZnO systems, the mechanism for methanol synthesis remains elusive. For example, in gas-phase hydrogenation studies, methanol may be generated by the reaction of methoxy adsorbates with adsorbed hydrogen; however, the ZnO support is critical to realizing any appreciable yield[10]. It seems likely that in addition to dispersing the Cu, the ZnO also plays a role via the controlling the geometry of active sites, coordination, or interfacial charge.

A strong consensus of these past studies indicates that both morphology and composition play a key role in dictating the catalytic activity of Cu/Zn nanoclusters, in particular, the technologically important methanol synthesis mechanism. In the present study, we focus on identifying the chemical and morphological structure of ZnO monolayer(s) on Cu nanoclusters supported on a crystalline ZnO substrate. In particular we employ the use of ZnO atomic layer deposition (ALD) to judiciously deposit ZnO on well-characterized Cu/ZnO($10\bar{1}0$) systems. The primary motivation is to extract the physical properties of the ALD-produced ZnO thin-films and, more importantly, to

elucidate the ensuing properties of the ZnO/Cu/ZnO($10\bar{1}0$) heterostucture in light of its potential catalytic properties relevant to methanol synthesis.

The use of ALD in the present case is based on the desire to explore the properties of Cu nanoclusters capped with ultra-thin films of ZnO. Specifically, ultra-thin films grown using ALD are typically uniform, dense, homogenous, pinhole-free, and extremely conformal to the underlying substrate. Therefore, ALD is unique in the sense that it allows for the growth of conformal films even on substrates with complex surface geometries. ALD was first developed in the 1970s as a method to grow thin electroluminescent films on large and non-planar substrates.[11] ALD began to attract considerable attention in the following decades due to its ability to grow ultra-thin and highly-conformal layers with atomic-scale thickness and composition control.[12] The fundamental advantage of ALD is that the film growth is surface controlled, rather than source controlled as in chemical vapor deposition (CVD) or molecular beam epitaxy (MBE). This is achieved by using sequential exposures, separating the (usually binary) reaction between the precursor compounds into two half-reactions of two differing reactants. As a result, the process proceeds step-wise in self-limiting surface reactions, separated by purge steps. Each full reaction cycle leads to the formation of one monolayer. Accordingly, the film thickness is determined by the number of reaction cycles, and the growth rate mainly depends on the length of each exposure/purge cycle.

In the present study, we use both thermal evaporation methods in UHV and ALD techniques to produce model ZnO/Cu/ZnO($10\bar{1}0$) structures. We use STM, SEM, and angle-resolved X-ray photoelectron spectroscopy (ARXPS) to study the morphology and core level electronic structure of ~10-15 ML Cu clusters on the ZnO($10\bar{1}0$) surface with

and without two-cycles of an ALD-produced ZnO capping layer as model systems for practical Cu/ZnO catalysts.

II. Experimental

STM and XPS experiments were performed in an ultra-high vacuum (UHV) chamber with a base pressure of $1x10^{-10}$ Torr. This chamber is equipped with sputter gun, LEED (SPECS ErLEED 150), e-beam Cu evaporator, and an Omicron VT STM-XA. XPS experiments are performed with an Omicron XM1000 X-ray source in combination with a SPECS PHOIBOS 150 hemispherical analyzer. The chamber is equipped with a prep-chamber in which samples can be load-locked into/out of UHV.

ZnO($10\bar{1}0$) single crystals with one side polished were purchased from commercial vendors. Sample surfaces were cleaned by cycles of Ne ion sputtering and vacuum annealing to 1000 ℃. Sample cleanliness was checked with LEED and XPS; clear and sharp (1 ×1) LEED patterns, and no contamination from carbon or other species visible in XPS, were observed after sputtering and vacuum annealing. Before deposition, the e-beam evaporator was fully outgassed to ensure the Cu evaporated was clean and without contamination. Deposition rates were calibrated by evaporating Cu onto a clean Ru(0001) crystal (Cu is known to grow as single-layer islands at submonolayer coverages on Ru(0001)[13, 14]) and determining the percentage of the surface covered using STM.

STM measurements were performed at room temperature with electrochemically etched tungsten tips. Tunneling voltages and currents were set in the range of 0.5-3V and 0.3-1.5nA respectively, depending on the surface conditions. SEM measurements were acquired employing a Hitachi S-3600N (at 50 keV). XPS measurements were performed at room temperature using monochromatic Al Ka_I radiation (hn = 1486.6 eV). High-

resolution spectra of Zn 2*p*, Cu 2*p*, and O 1*s* levels were recorded using a pass energy of 20 eV. The Zn 2*p*, Cu 2*p*, O 1s spectra were fit using CasaXPS software using a Gaussian/Lorentzian product lineshape. The photoemission emission angle was varied by rotation of the sample normal with respect to the SPECS analyzer, facilitating ARXPS. In the present study, ARXPS data were acquired at 0 ° (normal), 20 °, 40 ° and 60 ° emission angle.

After preparation and characterization of the Cu-nanocluster/ZnO($10\bar{1}0$) substrates, the samples were load-locked out of the UHV system and transferred (in air) to the ALD system. Subsequent atomic layer deposition of ZnO coatings on the nanocluster-coated sample was carried out in a Savannah 100 ALD system (Cambridge NanoTech Inc.) at 120 ℃ using $Zn(CH_2CH_3)_2$ (diethylzinc, DEZ) and H_2O as precursors with exposure time of 0.15s, a wait time of 5s and purge time of 40s. The principle of ZnO ALD growth from H_2O and DEZ is subjected to the two self-terminating reactions as follows:[15, 16]

$$ZnOH^* + Zn(CH_2CH_3)_2 \rightarrow ZnO–ZnCH_2CH_3^* + CH_3CH_3$$

$$ZnCH_2CH_3^* + H_2O \rightarrow ZnOH^* + CH_3CH_3$$

Following the ALD growth procedure, the samples were again transported in air to the UHV chamber for further ARXPS analysis or to the SEM for microstructure characterization.

III. Results And Disscusion

A. Voltammetric Studies

Voltammetric analysis was performed using ZnO coated Cu films as working electrodes in a standard three-electrode cell using an aqueous 0.1M K_2CO_3 electrolyte saturated with CO_2. The ZnO film was deposited using several sequences of ALD growth

with a final thickness near 1nm. Reduction of CO_2 at Cu electrodes in similar electrolytes shows it is possible to produce products such as methane and methanol.[15] In this case, the presence of a thin ZnO layer may affect the activity or selectivity of the catalyst in the same manner as thermally-driven methanol synthesis reactions. Figure 1 shows the forward cathodic scans from 0 to -1.2 (versus Ag/AgCl, 25mV/s) for Cu and ALD-ZnO coated electrodes in the same carbonate electrolyte. Forward scans to -1.2V without CO_2 showed little reduction currents and were similar using either electrode. The cathodic currents with CO_2 present at the ALD-coated Cu film are similar to the currents for Cu electrodes up to ~1V showing two small peaks that may be associated with reduction of copper oxides. The exponential increase in current at potentials greater than -1.0V (versus Ag/AgCl) suggests the ZnO may be reduced at these potentials; however, the charge is significantly larger than expected from the reduction of a 1nm thick film alone. In this case, it is possible that the ZnO lowers reaction overpotentials for deoxygenation steps (via the formation of hydroxides); however, product analysis showed no significant changes in selectivity relative to Cu electrodes.

B. Cluster Films Before ALD

Figure 2(a) shows an STM image of ~ 2 ML Cu deposited on ZnO($10\bar{1}0$) at room temperature. Prior STM studies of the clean ZnO($10\bar{1}0$) surface[17] reveals large terraces (10 – 100 nm) of different heights, with two perpendicular steps along [$1\bar{2}10$] and [0001] directions. Line profiles indicate that the typical height of one step is 2.9Å, which is about the same as the vertical separation of two Zn-O planes (2.8Å). Upon Cu deposition, it is clearly seen that a 3D cluster growth mode is adopted (Volmer-Weber growth mode) for low Cu coverage at room temperature. As seen, the whole surface is completely

covered with Cu clusters. With the experimental parameters employed here, there is a lack of ripening of the Cu clusters. The individual Cu clusters have an average size of ~8nm in diameter and ~1.4nm in height. The bright clusters in the image are Cu clusters on elevated terraces in the ZnO($10\bar{1}0$) and steps to lower terraces can be seen as the darker depressions in 2(a), also filled with Cu clusters. At higher Cu coverages (10 - 20 ML), individual clusters have slightly larger diameters resulting in a higher corrugation (~3nm). High quality, atomic resolution STM images are lacking, but in general the surfaces reveal a similar 3D cluster morphology.

Figure 2(b) shows an SEM image of 15 ML of Cu/ ZnO($10\bar{1}0$) prior to ALD. This film has been annealed in UHV to the same temperature of 120 ℃ as the ALD deposition requires in order to provide the thermal conditions for any cluster ripening that may occur. Typical Cu cluster sizes from the SEM image are in the 15-20 nm range.

C. Cluster Films After ALD

Figure 2(c) shows an SEM image of the 15 ML-Cu/ZnO($10\bar{1}0$) substrates after deposition of 2 cycles of ZnO. The image shows larger 3D clusters (~ 30–40 nm in diameter) across large areas of the sample. It is possible that some precursor-mediated ripening occurs during the ALD deposition at 120 ℃, but this lower temperature precludes the formation of any type of Cu-Zn alloy. The clear definition of the clusters is reduced and the image suggests that there is some filling-in of material between the clusters seen in 2(b). STM imaging of oxide films grown on the clusters did not give reliable images due to tip effects with the disordered oxide.

After ALD deposition, the sample was re-introduced into the UHV system and furthermore was gently annealed to ~120 ℃ to desorb any volatile adsorbates (e.g. water).

Subsequent XPS revealed only small amounts of carbonaceous contamination. Following the same procedure as before, a series of ARXPS spectra were acquired at identical emission angles taken from the sample prior to ALD. As before, Cu and Zn $2p_{1/2,\,3/2}$ core-level peaks were fitted and the results are shown in Figure 4. As seen in the "After ALD" square/solid-lines, there are many differences and trends compared to the "Before ALD" data.

After 15 ML of Cu was deposited on the clean ZnO($10\bar{1}0$) at room temperature in UHV, XPS was used to further characterize the system. The overview XP spectrum (Figure 3) reveals Cu and Zn $2p_{1/2,\,3/2}$ core-levels between 950 – 1050 eV, as well as their LMM Auger-lines, and 3*s*/3*p* core-levels. A fit to both the Zn ($2p_{3/2}$ binding energy of 1021.7 eV) and oxygen (1*s* binding energy of 530.4 eV) peaks indicates only pure ZnO from the underlying substrate without any sample charging artifacts. Moreover, the Cu $2p_{3/2}$ peak is located at 932.8 eV indicates that the nanoclusters are only metallic Cu^0, and clearly rules out any presence of Cu^{2+} (CuO). An absence of C 1*s* species indicates total lack of carbonaceous contamination.

Figure 3B (inset) shows a series of ARXP spectra, which includes the Zn and Cu 2*p* cores-levels, as a function of increasing emission angle. As seen from the spectra, the Cu/Zn peak ratio increases as the emission angle increases. Based on escape depths and mean free paths (~1-2 nm) arguments, the ARXPS technique provides higher surface/bulk sensitivity at higher emission angles. As shown in the inset, a fit of the areas of the core-levels are made and the results are shown in Figure 4. As seen in the "Before ALD" circle/dotted-lines, both Zn (Figure 4A) and Cu (Figure 4B) $2p_{3/2}$ peaks show little variation as a function of emission angle. However, the ratio of Cu/Zn peak areas (Figure

4C) shows a large increase (a factor of ×3.7) at 60° relative to normal emission (0°). The results of this XPS analysis is in total support of the STM data above reflecting 3D Cu^0 nanoclusters on an unperturbed flat ZnO($10\bar{1}0$) substrate.

First, the Cu (Figure 4B) $2p_{3/2}$ binding energy (BE) is lower by approximately 0.3 eV[18]. This BE shift is consistent with a partial oxidation of the $Cu^0 \rightarrow Cu^+$ (i.e. formation of Cu_20) and is expected because the sample was transported in ambient air. Moreover, the presence of any Cu^{2+} species (CuO) can be ruled out since this characterized by an increase in the BE[18].

Second, at low emission angles (Figure 4A), the binding energy of the Zn $2p_{3/2}$ core-level peak is nearly the same (within ~ 0.1 eV) as before. This is again expected because in this arrangement ARXPS primarily probes the bulk underlying ZnO. However, at high emission angles, ARXPS becomes more sensitive to the chemical properties of the ALD ZnO capping layer. In this case, the binding energy increases sharply to 1022.0 eV. This suggests that other species, such as chemisorbed hydroxides, may be present at the surface of the ALD-ZnO film. Although not conclusive, this notion is supported by prior XPS observations of a Zn $2p_{3/2}$ level at 1022.7 eV in $Zn(OH)_2$.[19]

Third, the Cu/Zn peak ratio (Figure 4C) for clusters coated with ZnO shows the opposite angular dependence of the uncoated clusters at largest emission angles. Rather than increasing sharply by a factor of ~ 4 in the "Before ALD" data, ARXPS reveals that for the "After ALD" there is a sharp drop in the Cu/Zn peak ratio at 60° emission angle. As discussed below, it is believed that the at the highest emission angles, Cu nanoclusters and their ALD ZnO capping layers begin to occlude one another, producing a higher surface sensitivity to the ZnO capping layer.

D. Discussion

Based on scanning tunneling (STM) and scanning electron (SEM) microscopy, a model of the morphology of the differing structures studies can be made. In combination with the ARXPS, a more detailed description of the influence of the ALD ZnO coating on the oxidation states and surface chemistry of the nanoclusters can be developed.

Figure 5A shows a schematic of the as-grown (UHV) 3D nanoclusters of Cu that homogeneously cover the clean ZnO($10\bar{1}0$) substrate. As a function of coverage and temperature these clusters have been seen to vary slightly in size and ripen on annealing.[17] STM reveals that at a coverage of ~ 15 ML, the metallic Cu^0 islands are approximately 10 nm in diameter. With ARXPS data taken at higher emission angles, one would expect that the surface sensitivity to the Cu clusters would be enhanced. This is precisely what is observed as the Cu/Zn peak-area ratio increases at higher emission angles.

Figure 5B shows a structural model of the Cu nanoclusters following two cycles of ALD ZnO thin-film growth. The unique property of the ALD-grown film is the conformal coating of the Cu nanoclusters, producing a uniform ZnO film on the tops and sides of the nanoclusters. A model for the behavior of the Cu/Zn 2*p* peak area ratio can be developed considering this conformal coating. For electron emission angles close to normal emission, one initially has the behavior observed for the uncoated clusters, that is, the sensitivity to Cu will increase as one probes through an increasing thickness of Cu. The thin ZnO coating in provides a slight attenuation of the Cu that is similar for emission angles near normal. For much higher emission angles, however, the ZnO-coated Cu clusters begin to occlude one another and this “shadowing” effect makes the influence

of the thin ZnO film is more pronounced. One approaches a condition where the path of the electron trajectory is increasingly dominated by the ZnO coating and consequently the Cu/Zn ratio drops. This observation provides strong additional evidence that a ZnO film is in fact coating the Cu clusters.

The core-level shifts observed for these samples provide additional information on the oxidation state of both Cu and Zn and on surface chemistry relevant to methanol formation. First, when the Cu nanoclusters are exposed to air, Cu^+ forms as evident by a shift of the Cu 2*p* to lower binding energy. Our data in Figure 3 also shows this for post-ALD processed samples, and it is possible that there is oxidation occurring during the ALD process, in addition to that produced by air exposure in transport. Upon ALD deposition of ~ 2 ML of ZnO on the Cu/ZnO($10\bar{1}0$) system, XPS reveals that the ZnO ultra-thin capping layer is chemically different from the underlying ZnO bulk. The post-ALD surfaces do not exhibit large amounts of carbon, and both the ALD process involving H_2O exposure as well as the air-exposure provide the potential for producing adsorbed surface hydroxyls, and result in the observed shift of the Zn 2*p* level to higher binding energy in the ALD thin-film.

Moreover, voltammetric analysis using suggests the surface ZnO may increase the CO_2 reduction activity. At cathodic potentials greater than -1V (versus Ag/AgCl), the reduction currents observed at ALD-coated Cu films were significantly higher than bare copper electrodes. While it is possible that the ALD-ZnO is reduced, the increased current could also be associated with increased density of Cu^+ species or ZnO-assisted deoxgenation steps.

IV. Summary And Conclusion

This study investigated the properties of ALD thin-films of ZnO on Cu nanoclusters on ZnO($10\bar{1}0$) as a potential model for active sites in methanol synthesis involving Cu/ZnO. Both cluster morpoholgy and oxidation states were studied and it was found that the initially metallic Cu clusters were partially oxidized to Cu^+ following film growth. The ~2ML ZnO films grown on these clusters provided evidence for surface hydroxides. Likewise, ALD ZnO coatings on Cu electrodes showed increased CO_2 reduction currents relative to Cu electrodes. The increased activity may be due to relative increase in Cu^+ sites or improved deoxygenation from the formation on hydroxides at the ZnO surface.

References

[1] Y. Choi, K. Futagami, T. Fujitani, and J. Nakamura, Applied Catalysis A: General **208**, 163 (2001).

[2] T. Fujitani and J. Nakamura, Applied Catalysis A: General **191**, 111 (2000).

[3] H. Sakurai and M. Haruta, Applied Catalysis A: General **127**, 93 (1995).

[4] H. Sakurai and M. Haruta, Catalysis Today **29**, 361 (1996).

[5] J. Strunk, K. Kaehler, X. Xia, M. Comotti, F. Schueth, T. Reinecke, and M. Muhler, Applied Catalysis A: General **359**, 121 (2009).

[6] O. Dulub, L. A. Boatner, and U. Diebold, Surf. Sci. **504**, 271 (2002).

[7] K. Ozawa, T. Sato, Y. Oba, and K. Edamoto, J Phys Chem C **111**, 4256 (2007).

[8] M. Behrens, et al., Science **336**, 893 (2012).

[9] M. Kroll, T. Lober, V. Schott, C. Woll, and U. Kohler, Phys. Chem. Chem. Phys. **14**, 1654 (2012).

[10] B. G. Nedrebo, U. B. Ericsson, O. Nygard, H. Refsum, P. M. Ueland, A. Aakvaag, S. Aanderud, and E. A. Lien, Metabolism **47**, 89 (1998).

[11] T. Suntola, Thin Solid Films **216**, 84 (1992).

[12] S. M. George, A. W. Ott, and J. W. Klaus, J. Phys. Chem. **1000**, 13121 (1996).

[13] R. Q. Hwang, J. Schroder, C. Gunther, and R. J. Behm, Phys. Rev. Lett. **67**, 3279 (1991).

[14] J. E. Houston, C. H. F. Peden, D. S. Blair, and D. W. Goodman, Surf. Sci. **167**, 427 (1986).

[15] A. W. Ott and R. P. H. Chang, Materials Chemistry and Physics **58**, 132 (1999).

[16] J. W. Elam, M. D. Groner, and S. M. George, Review of Scientific Instruments **73**, 2981 (2002).

[17] F. Wang, Louisiana State University, 2011.

[18] J. P. Tobin, W. Hirschwald, and J. Cunningham, Appl. Surf. Sci. **16**, 441 (1983).

[19] L. S. Dake, D. R. Baer, and J. M. Zachara, Surf. Interface Anal. **14**, 71 (1989).

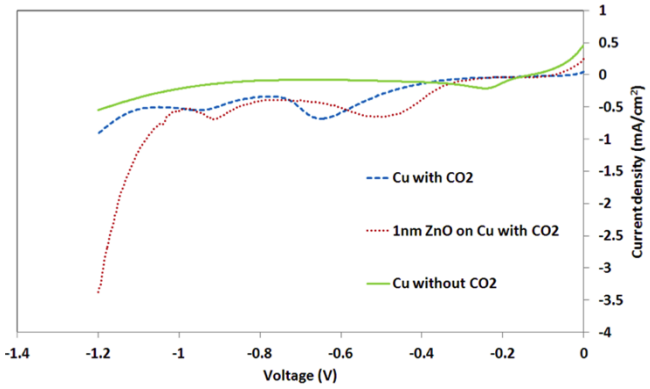

Figure 1 Voltammetry of Cu films without and with a 1nm ZnO ALD coating in electrolyte either saturated or without CO_2.

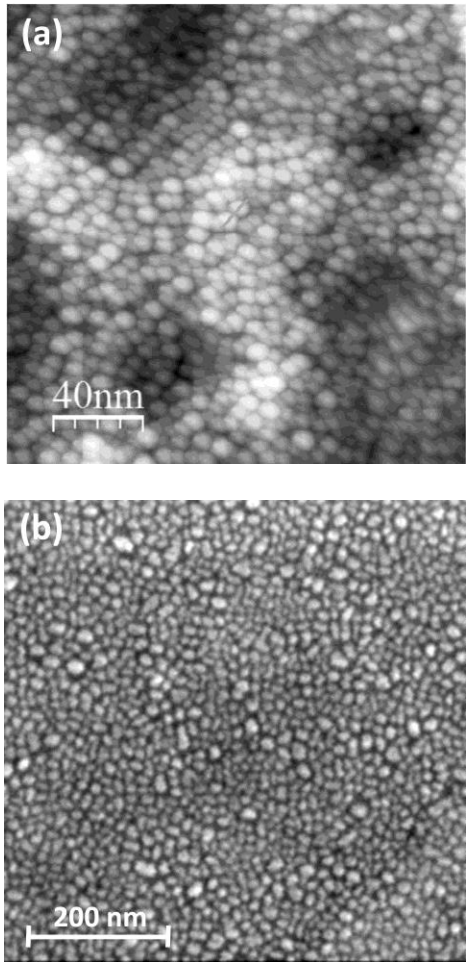

Figure 2 (a) STM image of 2 ML Cu/ZnO(10$\bar{1}$0) surface at RT (b) SEM image of 15 ML Cu/ZnO(10$\bar{1}$0) before and (c) after ALD deposition of 2 cycles of ZnO.

(Figure 2 continued)

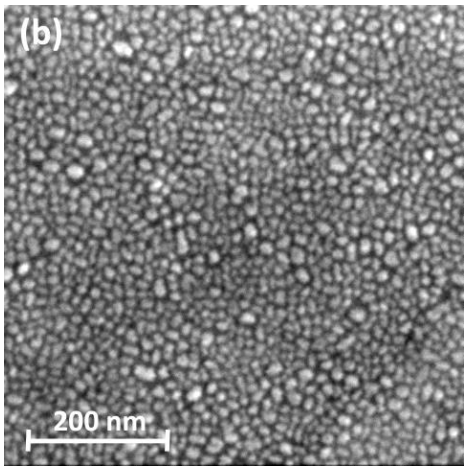

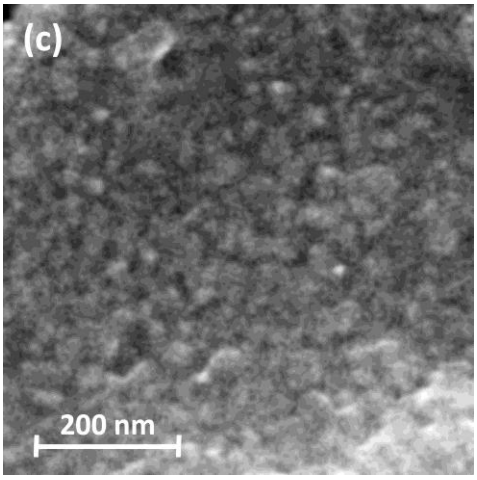

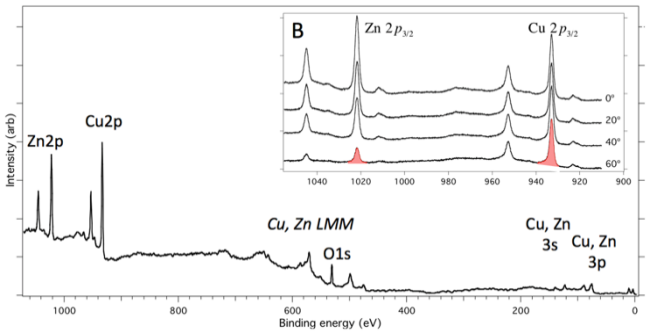

Figure 3 Overview XPS of 15 ML Cu deposited on clean ZnO(10$\underline{1}$0) at RT; B) (inset) Zn and Cu 3p $_{1/2}$ and 3p $_{3/2}$ as a function of XPS emission angle [areas of Cu and Zn 3p 3/2 are indicated for 60° emission angle].

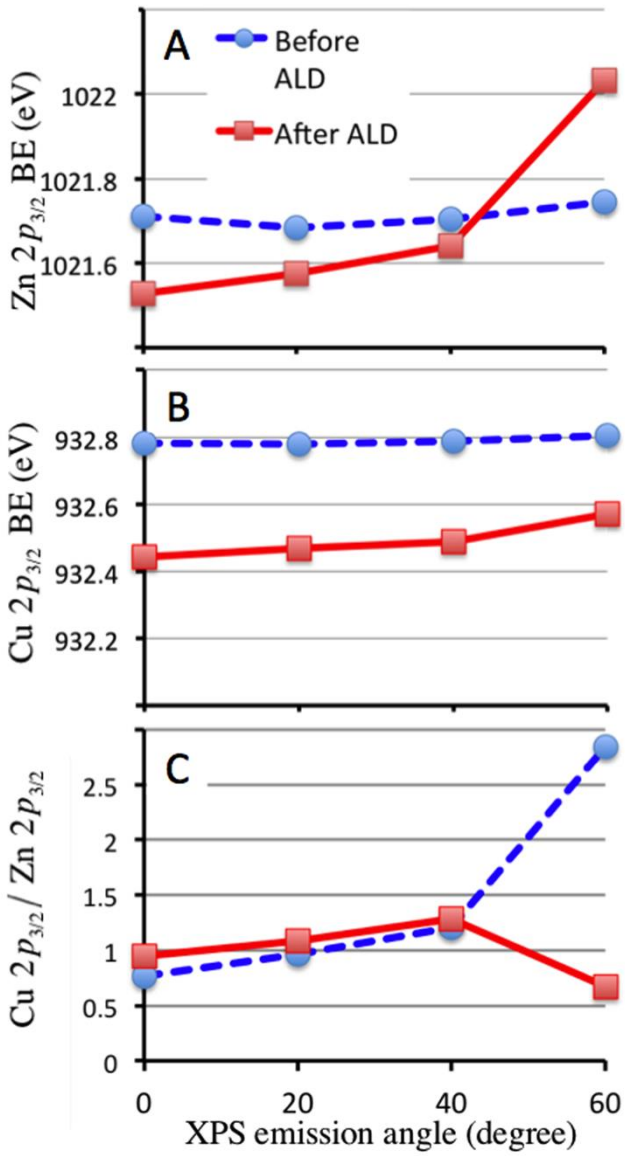

Figure 4 XPS fitting results for surfaces before and after ALD deposition of ~ 2 ML of ZnO as a function of XPS emission angle; A) Zn 3p $_{3/2}$ binding energy; B) Cu 3p $_{3/2}$ binding energy; C) Cu 2p/Zn 2p ratio

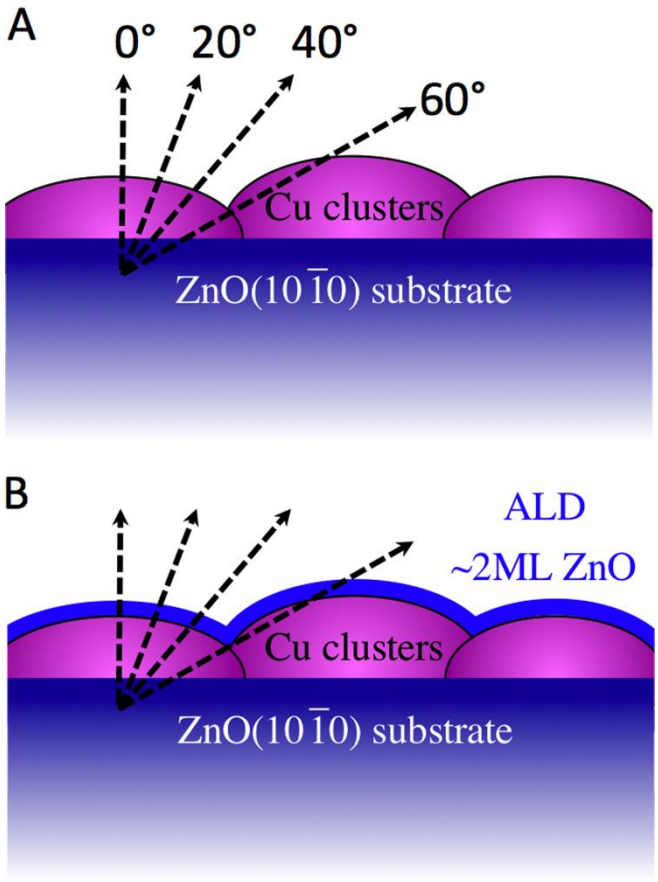

Figure 5 Model of surface morphology A) before and B) after ~ 2 ML ALD deposition of ZnO on 15 ML Cu/ZnO(10$\underline{1}$0) surface. (emission angles corresponds to Figure 2B and Figure 3)

Vita

Ziyu Zhang was born in Jiangsu province of P. R. China, on January 5, 1983. After completing his degree at Siyang middle (1994~1997) and high school (1997~2000), on August 2000, he entered University of Science and Technology of China (USTC) in Hefei, Anhui province and received the degree of Bachelor of Applied Physics on June, 2004. In August, 2006, He entered the graduate school in the department of Physics and Astronomy at the Louisiana State University (LSU). During his stay at LSU, he joined Center for Atomic-Level Catalyst Design, Energy Frontier Research Center, which is supported by Department of Energy (DOE) Office of Basic Energy Research Sciences. And he is going to receive his PhD degree of physics in May 2014.